

Solid oxide fuel cell reliability and performance modeling and fabrication by spray pyrolysis

by

Lin Liu

A dissertation submitted to the graduate faculty
in partial fulfillment of the requirements for the degree of

DOCTOR OF PHILOSOPHY

Major: Mechanical Engineering

Program of Study Committee:
Abhijit Chandra, Co-major Professor
Gap-Yong Kim, Co-major Professor
Ashraf Bastawros
Andrew C. Hillier
Pranav Shrotriya

Iowa State University

Ames, Iowa

2011

Copyright © Lin Liu, 2011. All rights reserved.

DEDICATION

This dissertation is dedicated to my parents,

Mr. Faxin Liu and Mrs. Penggai Di,

For their love and invaluable supports,

and

my loving wife,

Ruimin Wang,

for her love, encouragement and understanding through my Ph.D. study.

TABLE OF CONTENTS

LIST OF FIGURES	vi
LIST OF TABLES	ix
ACKNOWLEDGEMENTS	x
ABSTRACT	xi
CHAPTER 1. INTRODUCTION	1
1.1 Motivation	1
1.2 Research Framework and Objectives	5
1.2.1 Modeling of Thermal Stresses and Lifetime Prediction of Planar Solid Oxide Fuel Cell under Thermal Cycling Conditions	5
1.2.2 Fabrication of Solid Oxide Fuel Cell Anode Electrode by Spray Pyrolysis	6
1.2.3 Microstructural and Electrochemical Impedance Study of Ni-CGO Anodes for Solid Oxide Fuel Cells Fabricated By Ultrasonic Spray Pyrolysis	7
1.2.4 Modeling of Solid Oxide Fuel Cells Performance with Homogenous and Graded Anode in Particle Size and Porosity	8
1.3 Dissertation Organization	9
CHAPTER 2. MODELING OF THERMAL STRESSES AND LIFETIME PREDICTION OF PLANAR SOLID OXIDE FUEL CELL UNDER THERMAL CYCLING CONDITIONS	10
2.1 Nomenclature	10
2.2 Introduction	12
2.3 SOFC Reliability and Lifetime Prediction Thermo-mechanical Modeling	16
2.3.1 Modeling of Interfacial Shear Stress and Peeling Stress	18
2.3.2 Modeling of Crack Nucleation and Lifetime Prediction	21
2.4 Material Properties for the Cell and Model Validation	25
2.5 Results and Discussion	29
2.5.1 Sensitivity Analysis of Thermal Stresses	29
2.5.2 Crack Nucleation and Cell Lifetime Prediction under Thermal Cycling Conditions	33
2.6 Conclusions	36
CHAPTER 3. FABRICATION OF SOLID OXIDE FUEL CELL ANODE ELECTRODE BY SPRAY PYROLYSIS	37
3.1 Introduction	37
3.2 Experimental Procedures and Materials	41
3.2.1 Experimental Setup	41
3.2.2 Materials and Precursor Solution Preparation	42
3.2.3 Anode Film Deposition and Measurement	43
3.3 Ultrasonic Atomization Modeling	45

3.3.1 Modeling of Deposited Particle Size	45
3.3.2 Model Validation	46
3.4 Results and Discussion	48
3.4.1 Analysis of the Deposited Anode Film Microstructure	48
3.4.2 Effect of the Deposition Time	51
3.4.3 Effect of Precursor Solution Concentration	53
3.4.4 Effect of Deposition Temperature	55
3.4.5 Effect of Precursor Solution Feed Rate	59
3.5 Conclusions	60
CHAPTER 4. MICROSTRUCTURAL AND ELECTROCHEMICAL IMPEDANCE STUDY OF NI-CGO ANODES FOR SOLID OXIDE FUEL CELLS	61
4.1 Introduction	61
4.2 Experimental Procedures	63
4.2.1 Ultrasonic Spray Pyrolysis Deposition Experiment	63
4.2.2 AC Electrochemical Impedance Spectroscopy (EIS) Experiment	65
4.3 Results and Discussion	67
4.3.1 Ultrasonic Spray Pyrolysis Deposition Mechanism and Results of Anode Deposition Microstructure	67
4.3.2 AC Electrochemical Impedance Spectroscopy Results of Different Anode Deposition Microstructures	72
4.4 Conclusions	76
CHAPTER 5. MODELING OF SOLID OXIDE FUEL CELLS PERFORMANCE WITH HOMOGENOUS AND GRADED ANODE IN PARTICLE SIZE AND POROSITY	78
5.1 Nomenclature	78
5.2 Introduction	80
5.3 Model Development	83
5.4 Model validation	93
5.5 Results and discussion	98
5.5.1. Analysis of homogenous anodes	98
5.5.2. Effect of particle size grading	103
5.5.3. Effect of porosity grading	107
5.6 Conclusion	108
CHAPTER 6. SUMMARY AND SCIENTIFIC CONTRIBUTIONS	110
6.1 Summary	110
6.1.1 Modeling of Thermal Stresses and Lifetime Prediction of Planar Solid Oxide Fuel Cell under Thermal Cycling Conditions	111
6.1.2 Fabrication of Solid Oxide Fuel Cell Anode Electrode by Spray Pyrolysis	112
6.1.3 Microstructural and Electrochemical Impedance Study of Ni-CGO Anodes for Solid Oxide Fuel Cells Fabricated by Ultrasonic Spray Pyrolysis	113
6.1.4 Modeling of Solid Oxide Fuel Cells Performance with Homogenous and Graded Anode in Particle Size and Porosity	114
6.2 Scientific Contributions	115
6.3 Recommendations for the future work	117

LIST OF FIGURES

Figure 1. World Electric Power Generation and Total Energy Consumption Overlook (a) Growth in Electricity Generation and Total Energy Consumption (index, 1990=1) and (b) World Electricity Generation by Different Types of Fuel (trillion kilowatthours)	2
Figure 2. Comparison of Efficiency of Different Techniques of Electricity Power Generation Relative to the Plant Size (EG&G Technical Services Inc., 2004b)	3
Figure 3. SOFC Emission Environmental Benefits (FuelCell Energy, March 21, 2007)	3
Figure 4. Schematic of the Concept of Modeling Approach	18
Figure 5. Schematic of Different SOFC Configuration (a) Electrolyte-supported (b) Anode-supported	20
Figure 6. Schematic Diagram of Half-SOFC structure with an Isothermal and Porous Homogenous Interfacial Layer	21
Figure 7. Thermal Stress Comparison with Anode-electrolyte and cathode-electrolyte in Electrolyte-supported SOFC: (a) Shear Stress (b) Peeling Stress	30
Figure 8. Thermal Stress Comparison with Different Porosity in Electrolyte-supported SOFC: (a) Shear Stress (b) Peeling Stress	31
Figure 9. SEM Image of a Partially Delaminated Anode Layer on YSZ Electrolyte (Koch et al., 2006)	31
Figure 10. Thermal Stress Comparison with Different Thickness in Electrolyte-supported SOFC: (a) Shear Stress (b) Peeling Stress	32
Figure 11. Thermal Stress Comparison with Different Porosity in Anode-supported SOFC: (a) Shear Stress (b) Peeling Stress	33
Figure 12. Thermal Stress Comparison with Different Thickness in Anode-supported SOFC: (a) Shear Stress (b) Peeling Stress	33
Figure 13. Damage Evolution in Electrolyte-supported SOFC ($\omega_{\max} = 0.4$ and the Anode Layer Porosity $p = 47\%$)	34
Figure 14. Anode Porosity Effect on Number of Cycles to Failure in Different SOFC Configurations	35
Figure 15. Anode Thickness Effect on Critical Thermal Cycle	35
Figure 16. Spray Pyrolysis Experiment Setup	41
Figure 17. Comparison of Deposited Particle Size Calculated from Eqn. (4) and Measured from Experiments ($L = 1.23 \text{ ml min}^{-1}$, $Q = 1.5 \text{ l min}^{-1}$, $T = 300 \text{ }^\circ\text{C}$)	47
Figure 18. Images of Deposited Particles at Various Precursor Solution Concentrations ($L = 1.23 \text{ ml min}^{-1}$, $Q = 1.5 \text{ l min}^{-1}$, $T = 300 \text{ }^\circ\text{C}$). d_{pe} is the Diameter of Experiment Particle. (a) $C = 0.4 \text{ mol l}^{-1}$, $d_{pe} = 16 \text{ } \mu\text{m}$ (b) $C = 0.1 \text{ mol l}^{-1}$, $d_{pe} = 6 \text{ } \mu\text{m}$ and (c) $C =$ 0.025 mol l^{-1} , $d_{pe} = 2 \text{ } \mu\text{m}$	48
Figure 19. EDS Analysis of Corresponding Elements Distribution	50
Figure 20. XRD Analysis of the Deposited Film	51

Figure 21. Deposited Substrate Morphology at Different Deposition Times ($L = 1.23 \text{ ml min}^{-1}$, $Q = 1.5 \text{ l min}^{-1}$, $C = 0.1 \text{ mol l}^{-1}$, $T = 300 \text{ }^{\circ}\text{C}$) (a) After 15 minutes (b) After 30 minutes (c) After 45 minutes (d) After 120 minutes	52
Figure 22. Increase of Anode Film Thickness with Deposition Time ($L = 1.23 \text{ ml min}^{-1}$, $Q = 1.5 \text{ l min}^{-1}$, $C = 0.1 \text{ mol l}^{-1}$, $T = 300 \text{ }^{\circ}\text{C}$)	53
Figure 23. Images of Deposited Anode Film at Different Precursor Solution Concentrations ($L = 1.23 \text{ ml min}^{-1}$, $Q = 1.5 \text{ l min}^{-1}$, $T = 300 \text{ }^{\circ}\text{C}$) (a) $C = 0.4 \text{ mol l}^{-1}$ (b) $C = 0.1 \text{ mol l}^{-1}$ (c) $C = 0.025 \text{ mol l}^{-1}$	54
Figure 24. Effect of Temperature and Precursor Solution Concentration on Deposited Anode Film Porosity ($L = 1.23 \text{ ml min}^{-1}$, $Q = 1.5 \text{ l min}^{-1}$)	55
Figure 25. Images of deposited anode film at various deposition temperatures ($L = 1.23 \text{ ml min}^{-1}$, $Q = 1.5 \text{ l min}^{-1}$, $C = 0.025 \text{ mol l}^{-1}$) (a) $T = 250 \text{ }^{\circ}\text{C}$ Bottom layer (b) $T = 250 \text{ }^{\circ}\text{C}$ Top layer (c) $T = 300 \text{ }^{\circ}\text{C}$ Bottom layer (d) $T = 300 \text{ }^{\circ}\text{C}$ Top layer (e) $T = 350 \text{ }^{\circ}\text{C}$ Bottom layer (f) $T = 350 \text{ }^{\circ}\text{C}$ Top layer	57
Figure 26. Effect of temperature and precursor solution concentration on deposited particle size ($L = 1.23 \text{ ml min}^{-1}$, $Q = 1.5 \text{ l min}^{-1}$)	58
Figure 27. Severely cracked deposited anode film ($L = 1.23 \text{ ml min}^{-1}$, $Q = 1.5 \text{ l min}^{-1}$, $C = 0.1 \text{ mol l}^{-1}$, $T = 450 \text{ }^{\circ}\text{C}$)	58
Figure 28. Images of deposited anode film at different precursor solution feed rate ($Q = 1.5 \text{ l min}^{-1}$, $C = 0.1 \text{ mol l}^{-1}$, $T = 250 \text{ }^{\circ}\text{C}$) (a) $L = 1.23 \text{ ml min}^{-1}$ (b) $L = 1.78 \text{ ml min}^{-1}$	59
Figure 29. Spray Pyrolysis Experiment Setup	64
Figure 30. AC Impedance Test Sample Configuration	66
Figure 31. AC Impedance Test Setup	66
Figure 32. Schematic of Deposition Mechanism of Modified Spray Pyrolysis	68
Figure 33. Microstructure of Deposited Anode Film ($L = 1.23 \text{ ml min}^{-1}$, $Q = 1.5 \text{ l min}^{-1}$, $C = 0.1 \text{ mol l}^{-1}$, $T = 300 \text{ }^{\circ}\text{C}$): (a) Top View and (b) Cross Section.	69
Figure 34. SEM Images of Anode Microstructures: (a) Sample #1 ($d_p = 17 \text{ }\mu\text{m}$, $p = 36\%$), (b) Sample #2 ($d_p = 2.5 \text{ }\mu\text{m}$, $p = 22\%$) and (c) Sample #3 ($d_p = 1.5 \text{ }\mu\text{m}$, $p = 34\%$)	70
Figure 35. Plot of Film Porosity versus Temperature and Precursor Solution Concentration ($L = 1.23 \text{ ml min}^{-1}$, $Q = 1.5 \text{ l min}^{-1}$).	71
Figure 36. Plot of Particle Size versus Deposition Temperature	71
Figure 37. Nyquist Plots Depicting EIS Results for Various Samples at Three Test Temperatures: (a) Sample #1 ($d_p = 17 \text{ }\mu\text{m}$, $p = 36\%$), (b) Sample #2 ($d_p = 2.5 \text{ }\mu\text{m}$, $p = 22\%$) and (c) Sample #3 ($d_p = 1.5 \text{ }\mu\text{m}$, $p = 34\%$)	74
Figure 38. Equivalent Circuit of Electrochemical Test Cell	74
Figure 39. Arrhenius Plot of Electrode Resistances for Three Test Samples	76
Figure 40. A schematic of TPB and microstructure grading: (a) reaction at TPB, (b) particle size grading, and (c) porosity grading	83
Figure 41. Comparison between model simulation and experimental data of Jiang et al: (a) voltage losses at 1073 K and 1173K and (b) individual voltage losses at 1073 K.	97

Figure 42. SEM images of anode microstructures: (a) Sample #1 ($d_p = 17 \mu\text{m}$, $\varepsilon = 36\%$), (b) Sample #2 ($d_p = 2.5 \mu\text{m}$, $\varepsilon = 22\%$) and (c) Sample #3 ($d_p = 1.5 \mu\text{m}$, $\varepsilon = 34\%$).	98
Figure 43. Voltage loss distribution: (a) Sample #1, (b) Sample #2 and (c) Sample #3	101
Figure 44. TPBs reaction area versus electrode particle size	101
Figure 45. Nyquist plots depicting EIS results for various samples at three test temperatures: Sample #1 ($d_p = 17 \mu\text{m}$, $\varepsilon = 36\%$), Sample #2 ($d_p = 2.5 \mu\text{m}$, $\varepsilon = 22\%$) and Sample #3 ($d_p = 1.5 \mu\text{m}$, $\varepsilon = 34\%$).	102
Figure 46. Diffusion coefficients for three test samples: Sample #1 ($d_p = 17 \mu\text{m}$, $\varepsilon = 36\%$), Sample #2 ($d_p = 2.5 \mu\text{m}$, $\varepsilon = 22\%$) and Sample #3 ($d_p = 1.5 \mu\text{m}$, $\varepsilon = 34\%$).	102
Figure 47. Voltage loss versus particle diameter at different current densities.	104
Figure 48. Particle size grading profiles used in this study	105
Figure 49. SOFCs thermo-mechanical reliability and electrochemical performance model integration	118

LIST OF TABLES

Table 1. Material properties and geometries used for model validation	27
Table 2. Material properties and geometries used for the calculation of thermal stresses and lifetime prediction	27
Table 3. Young's modulus of electrode at different porosities	29
Table 4. Comparison of SOFC fabrication techniques (Flesner, 2009)	40
Table 5. Experimental Matrix Used in the Study	44
Table 6. Values used to calculate deposition particle diameter (d_p) by ultrasonic atomization	47
Table 7. EDS data showing element composition in the deposited anode film	49
Table 8. Experimental matrix used in the study	64
Table 9. Test sample preparation condition and sample microstructure information	66
Table 10. Boundary conditions for the electrode.	92
Table 11. Values of model parameters used in validation.	94
Table 12. Test sample preparation condition and sample microstructure information	95
Table 13. Test sample preparation condition and sample microstructure information	95
Table 14. Values of model parameters used in the study	104
Table 15. Summary of particle size grading	106
Table 16. Percent voltage loss reduction from a homogeneous anode microstructure	108

ACKNOWLEDGEMENTS

I would like to take this opportunity to express my deepest appreciation to my advisors, Prof. Gap-Yong Kim and Prof. Abhijit Chandra, for their great support, guidance and patience throughout my Ph.D. study and research. I would also like to extend my appreciation to Prof. Bastawros and Prof. Shrotriya for their invaluable lecture teaching. I deeply appreciate Prof. Hillier for providing guidance and equipment in cell's electrochemical performance test.

I am grateful to the colleagues in our lab for their assistance and all the pleasure of working together. Also, I specially thank my colleague Yufeng Wu for helping me with material characteristic analysis and experiment. Finally, I would give my gratitude to my dear wife Ruimin Wang for her unconditional support, love, encouragement, and patience through my Ph.D. study.

ABSTRACT

SOFCs have the potential to meet the critical energy needs of our modern civilization and minimize the adverse environmental impacts from excessive energy consumption. They are highly efficient, clean and can run on a variety of fuel gases. However, wide adoption of SOFCs is currently hindered by cell durability, manufacturing cost, and lack of fundamental understanding on electrochemical performance of the cell. In order to evaluate the durability of SOFCs, a mathematical thermo-mechanical model was developed to provide the distribution of thermal stresses during thermal cycling, and predict the lifetime of a cell. In addition, an ultrasonic spray pyrolysis prototype fabrication setup, which has the ability to tailor the microstructure of the deposited film, was established as an economically practical fabrication method to deposit the electrode of SOFC. Then, the electrochemical performances of deposited cells with tailored microstructures were investigated in order to better understand the impact of fabrication process parameters on cell electrochemical performance using AC electrochemical impedance spectroscopy. Furthermore, a complete electrode polarization model of SOFCs has been developed and utilized to analyze the performance of homogenous and functionally graded anode with different particle size and porosity profiles. The thermo-mechanical model study showed thermal stresses were more concentrated near the free edge. As the porosity and the thickness of anode increased, the lifetime of the cell decreased. The precursor solution concentration and deposition temperature were found to be the most critical parameters that

influenced the microstructure. By manipulating deposited microstructures, the Area Specific Resistance (ASR) of the deposited anode improved and the activation energy decreased. The developed thermo-mechanical model is one of the first attempts to understand cyclic failure behavior of multilayer SOFC through theoretical approach. Low polarization and activation energy makes the developed prototype fabrication setup a promising candidate for the fabrication of high performance SOFC electrode with tailored microstructure. The study of developing electrode polarization model experimentally and numerically demonstrated the potential of controlling the electrode microstructure of a SOFC to improve the cell's electrochemical performance. The work contributes to the understanding of cell performance in relation to graded microstructures.

CHAPTER 1. INTRODUCTION

1.1 Motivation

Solid oxide fuel cells (SOFC) are an environmentally friendly technology that could play a critical role in ensuring the development of a more sustainable and safe global energy infrastructure. The world energy consumption is dramatically increasing to meet the needs of civilization and the mass industrialization of human society, enhanced life quality, and the increased world population, (see Figure 1 (a)). Because of the high manufacturing cost of alternative energy power generation system, the majority of electricity is still generated from the combustion of fossil fuels as shown in Figure 1 (b). Due to the limited reserve of fossil fuels and diminishing fossil fuel resources, excessive energy consumption has triggered a rise in the price of fossil fuel, production cost, high inflation and even economic crisis. In addition, the excessive consumption of energy has been widely recognized to have significant adverse impacts on human, animal and other life forms. SOFCs have the potential to meet the urgent energy needs of our modern civilization and minimize the environmentally adverse effects of excessive energy consumption. Unlike the conventional energy conversion through combustion process, SOFCs convert the chemical energy of the fuel directly to electrical energy, which is not subject to the Carnot thermodynamic inefficiency. As shown in Figure 2, the SOFCs possess 50 – 60% efficiency compared with the 33% efficiency of a fossil fuel plant. SOFCs allow conversion of a wide range of gasified hydrocarbon fuels such as, ammonia, natural gas, gasified coal, etc. Unlike conventional combustion-based power generation technologies, SOFCs can significantly decrease the detrimental environmental

impacts. The pollution reductions can be seen from Figure 3, where SOFCs emit virtually zero SO_x and NO_x emissions, and the emitted CO_2 is significantly reduced by more than 50% (FuelCell Energy, March 21, 2007). SOFC systems are completely quiet, clean, and compact, which makes them suitable for almost any location avoiding potential NIMBY issues.

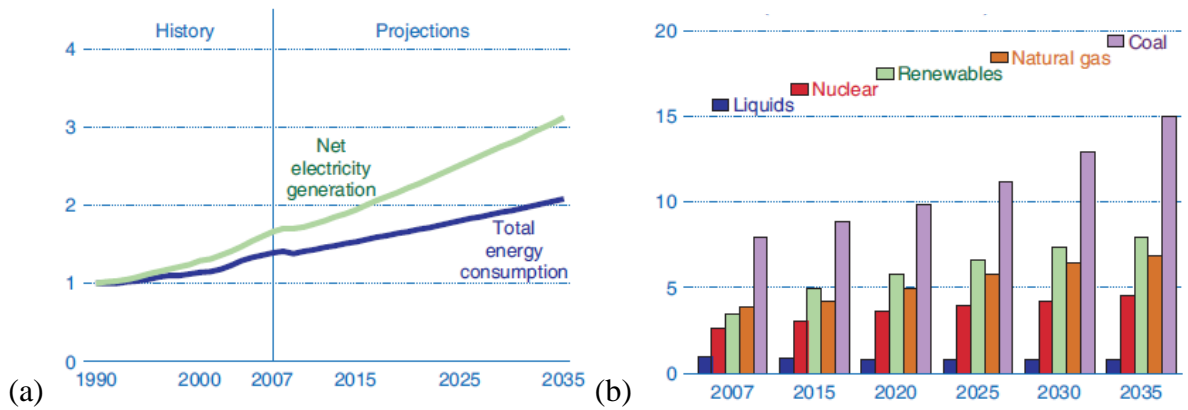


Figure 1. World Electric Power Generation and Total Energy Consumption Overview

(a) Growth in Electricity Generation and Total Energy Consumption (index, 1990=1)
and (b) World Electricity Generation by Different Types of Fuel (trillion kilowatthours)

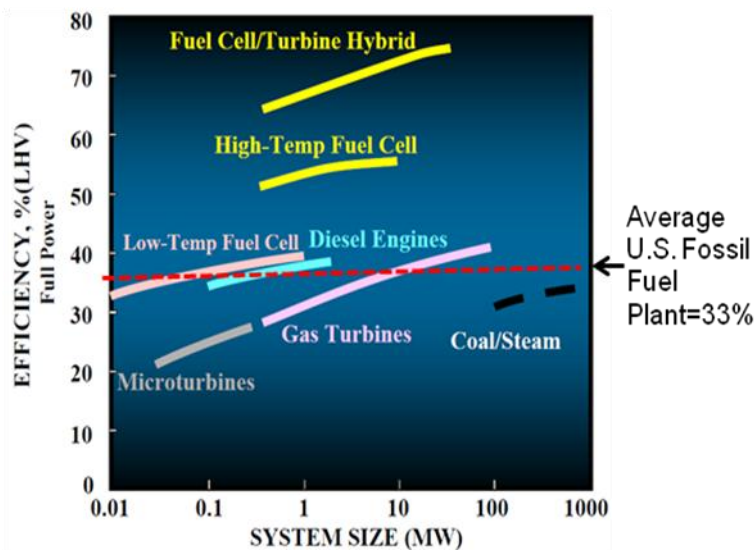


Figure 2. Comparison of Efficiency of Different Techniques of Electricity Power Generation Relative to the Plant Size (EG&G Technical Services Inc., 2004b)

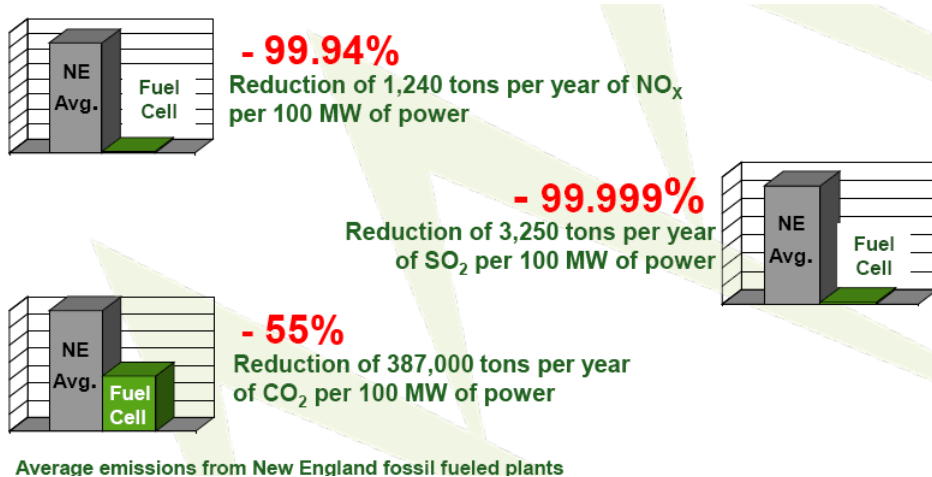


Figure 3. SOFC Emission Environmental Benefits (FuelCell Energy, March 21, 2007)

Even though SOFCs possess those aforementioned advantages, durability and cost are currently hindering potential applications in stationary, transport and portable power generation. Durability is inadequate for some SOFC applications. This is compounded by

uncertain mechanical reliability over the cell lifetime since SOFCs operate at high temperatures (above 600°C) and endure significant thermal stresses induced by thermal mismatch in cell components under thermal cycling conditions. Therefore, catastrophic failure often occurs suddenly due to material fracture or layer delamination during operation. In addition, it is difficult to predict cell lifetime under operating conditions. Also, manufacturing costs are still relatively high which requires new processing methods to maximize their performance-cost ratio. Another major challenge is the lack of fundamental understanding on the kinetics of electrode electrochemical processes. The polarization and degradation of SOFC performance has been reported repeatedly, which is often attributed to the complex combined effects of thermo-mechanical, electrical and chemical driving forces in the cell.

The motivation of this study is to evaluate the lifetime of cell using predicted thermal stresses in a cell and provide a deeper understanding of SOFC electrochemical performance in different tailored electrode microstructures. The mathematical model can also be easily applicable to different configurations of SOFC. An economically practical prototype fabrication setup is established to deposited SOFC components with tailored microstructure. The electrochemical performance of deposited cell with tailored microstructures is also investigated in order to better understanding the impact of fabrication process parameters on the improvement on the cell electrochemical performance. A fundamental theory-based numerical model has been proposed and developed to evaluate the effects of electrode microstructure variation on a SOFC electrochemical performance. The model helps to

understand the implications of varying the electrode microstructure from the polarization standpoint.

1.2 Research Framework and Objectives

The objectives of the study are to understand the influence of the cell microstructure and thermal stresses developed during the operation on the SOFC's electrochemical performance and cell lifetime. A thermo-mechanical model has been developed to predict the cell lifetime based on thermal cycling fatigue. Then, a spray deposition technique has been developed to analyze the anode cell microstructure and understand its impact on electrochemical performance of the cell. Furthermore, a complete electrode polarization model of SOFCs has been developed and utilized to analyze the performance of homogenous and functionally graded anode with different particle size and porosity profiles. Based on the outcomes of this study, a potential pathway to integrate thermo-mechanical model and electrochemical model has been recommended in Chapter 6.

1.2.1 Modeling of Thermal Stresses and Lifetime Prediction of Planar Solid Oxide Fuel Cell under Thermal Cycling Conditions

A typical operating temperature of a Solid Oxide Fuel Cell (SOFC) is above 600 °C, which leads to severe thermal stresses caused by the difference in material mechanical properties during thermal cycling. Interfacial shear stress and peeling stress are the two types of thermal stress that can cause the mechanical failure of the SOFC. Two commonly

used SOFC configurations (electrolyte-supported and anode-supported) were considered for this study. The paper developed a mathematical model to estimate the thermal stresses and to predict the lifetime of the cell (Ni/8YSZ-YSZ-LSM). Due to the mismatch of the material mechanical properties of the cell layers, a crack nucleation induced by thermal stresses can be predicted by the crack damage growth rate and the initial damage distribution in the interfacial layer for each thermal cycle. It was found that the interfacial shear stress and peeling stress were more concentrated near the electrode free edge areas. The number of cycles needed for failure decreased with the increase in the porosity of electrode. The number of cycle for failure decreased with increase in electrolyte thickness for both anode- and electrolyte-supported SOFC. The model provides insight into the distribution of interfacial shear stress and peeling stress and can also predict damage evolution in a localized damage area in different SOFC configurations.

1.2.2 Fabrication of Solid Oxide Fuel Cell Anode Electrode by Spray Pyrolysis

Large triple phase boundaries (TPBs) and high gas diffusion capability are critical in enhancing the performance of a Solid Oxide Fuel Cell (SOFC). In this study, ultrasonic spray pyrolysis has been investigated to assess its capability in controlling the anode microstructure. Deposition of porous anode film of nickel and $\text{Ce}_{0.9}\text{Gd}_{0.1}\text{O}_{1.95}$ on a dense 8 mol.% yttria stabilized zirconia (YSZ) substrate was carried out. First, an ultrasonic atomization model was utilized to predict the deposited particle size. The model accurately estimated the deposited particle size based on the feed solution condition. Second, effects of various process parameters, which included the precursor solution feed rate, precursor

solution concentration and deposition temperature, on the TPB formation and porosity were investigated. The deposition temperature and precursor solution concentration were the most critical parameters that influenced the morphology, porosity and particle size of the anode electrode. Ultrasonic spray pyrolysis achieved homogeneous distribution of constitutive elements within the deposited particles and demonstrated capability to control the particle size and porosity in the range of 2–17 μm and 22–54%, respectively.

1.2.3 Microstructural and Electrochemical Impedance Study of Ni-CGO Anodes for Solid Oxide Fuel Cells Fabricated By Ultrasonic Spray Pyrolysis

Optimization of the electrode microstructure in a Solid Oxide Fuel Cell (SOFC) is an important approach to performance enhancement. In this study, the relationship between the microstructure and electrochemical performance of an anode electrode fabricated by ultrasonic spray pyrolysis was investigated. Nickel- $\text{Ce}_{0.9}\text{Gd}_{0.1}\text{O}_{1.95}$ (Ni-CGO) anodes were deposited on a dense yttria stabilized zirconia (YSZ) substrate by ultrasonic spray pyrolysis, and the resulting microstructure was analyzed. Scanning electron microscope (SEM) examinations revealed the impact of deposition temperature and precursor solution concentration on anode morphology, particle size and porosity. The electrochemical performance of the anode was measured by Electrochemical Impedance Spectroscopy (EIS) using a Ni/CGO-YSZ-Ni/CGO symmetrical cell. The deposited anode had a particle size and porosity in ranging between 1.5–17 μm and 21%–52%, respectively. The estimated volume-specific triple phase boundary (TPB) length increased by one order of magnitude from 0.33 $\mu\text{m} \mu\text{m}^{-3}$ to 3.57 $\mu\text{m} \mu\text{m}^{-3}$ as a result of decrease of the particle size and increase of the

porosity. The corresponding area specific electrode resistance decreased from 5.45 ohm cm² to 0.61 ohm cm² and the activation energy decreased from 1.06 eV to 0.86 eV as the TPB length increased.

1.2.4 Modeling of Solid Oxide Fuel Cells Performance with Homogenous and Graded Anode in Particle Size and Porosity

The aim of this work was to understand the effects of electrode microstructure grading on a SOFC performance. In this study, a fundamental theory-based numerical model has been proposed and developed to evaluate the effects of electrode microstructure variation on a SOFC performance. The model can effectively provide insight into the evaluation of electrochemical performance with designed SOFC electrodes. All three major loss distributions can be obtained and separated from the overall voltage loss. Three deposited SOFC anode samples have been analyzed by the model. The results demonstrated the potential of graded microstructure can improve the electrochemical performance of a SOFC. The concept of nonlinearly graded microstructures in a SOFC electrode was explored for the first time in this work. This study investigated the particle size and porosity grading range effects on grading profile, including linear and nonlinear profiles, and voltage losses. It has been shown that a larger particle size grading range (0.3–8 μm) is more effective at reducing voltage losses than smaller ranges. Linear grading showed reduced voltage losses over homogeneous anodes. Nonlinear grading demonstrated particular benefit over linear and homogenous microstructures. Particle size grading was more effective at reducing losses in a SOFC anode than porosity grading because the reaction area increased squarely with

decreasing particle size, but parabolically with decreasing porosity. Also, the fact that particle size grading can range over two orders of magnitude is advantageous when porosity grading cannot. This study experimentally and numerically demonstrated the potential of controlling the electrode microstructure of a SOFC to improve the cell's electrochemical performance. The work contributes to the understanding of cell performance in relation to graded microstructures.

1.3 Dissertation Organization

The remainder of the dissertation is divided into five chapters. In chapter 2, a mathematical model is developed to estimate the thermal stresses and to predict the lifetime of the SOFC cell. The sensitive analysis of thermal stresses and lifetime in electrolyte-supported SOFC and anode-supported SOFC are also presented. In chapter 3, investigation on the application of ultrasonic spray pyrolysis in fabrication of SOFC electrode is performed. The effects of process parameters' effects on deposited electrode microstructure have been investigated. Chapter 4 assesses the deposited SOFC anode electrodes using AC electrochemical impedance spectroscopy. In chapter 5, a fundamental theory-based numerical model has been proposed and developed to evaluate the effects of electrode microstructure variation on a SOFC performance. A summary and contribution of this research are presented in Chapter 6. In the last chapter, suggestions on future works are also provided and discussed.

**CHAPTER 2. MODELING OF THERMAL STRESSES AND LIFETIME
PREDICTION OF PLANAR SOLID OXIDE FUEL CELL UNDER THERMAL
CYCLING CONDITIONS**

2.1 Nomenclature

Symbols

a material constant.

b the average spacing between microscale damage.

D the average size of microscale damage.

E_1, E_2 young's moduli for materials of bonded layers.

E_a Young's modulus for materials of bonded layers.

E'_i the plane strain modulus.

G_a shear modulus of interfacial layer.

h_1 , thickness of top layer.

h_2 thickness of bottom layer.

h_a thickness of interfacial layer.

K stress intensity factor.

K_I opening stress intensity factor.

K_{II} in plane shear stress intensity factor.

l_1, l_2 half length of top and bottom layers.

n material constant.

N the number of thermal cycle.

$N_{nucleation}$ the maximum number of thermal cycling the material sustain before a macroscopic crack appears.

p porosity of electrode.

u additional cyclic sliding.

v additional cyclic stretching.

ν_1, ν_2 , poisson's ratio of top and bottom layer.

ν_a , poisson's ratio of interfacial layer.

Greek

α_1, α_2 coefficient of thermal expansion for materials of bonded layers.

β material constant.

Δ value variation.

ΔK_I mode I cyclic stress intensity factor at a microcrack tip.

ΔK_{II} mode II cyclic stress intensity factor at a microcrack tip

ζ calculation parameter.

δ_{open} crack opening displacement.

δ_{shear} crack sliding displacement.

$\Delta\sigma$ amplitude of local cyclic normal stresses.

$\Delta\tau$ amplitude of local cyclic shear stresses.

λ the ratio of damage cluster size to average microcrack spacing.

ξ calculation parameter.

σ peeling stress.

$\sigma_{thermal}$ interfacial stress at the free edge ($x=l_1$).

$\sigma_{peeling}$ interfacial peeling stress.

$\tau_{interfacial}$ interfacial shear stress.

χ calculation parameter.

ω nondimensional damage parameter.

$\omega_{average}$ the average damage level in the localized damage region of interfacial layer.

ω_{max} the maximum damage level in the localized damage region of interfacial layer.

Superscript

“ ’ ” normalized parameter.

2.2 Introduction

Degradation of a Solid Oxide Fuel Cell (SOFC) is often referred to as the decrease of a cell's electrical performance or mechanical failure (Yokokawa, Tu, Iwanschitz and Mai, 2008; Hsiao, 1997; Komatsu, Watanabe, Arakawa and Arai, 2009; Laurencin, Delette, Morel, Lefebvre-Joud and Dupeux, 2009). The consequences of thermal stress and redox cycle where the nickel anode is repeatedly oxidized and reduced lead to performance degradation and shortening of the SOFC lifetime (Bujalski, 2007). It has been reported that the decrease of the overall cell electrical performance is mainly due to the degradation of the anode microstructure (Fukui, Ohara, Naito and Nogi, 2002; Hagen, Barfod, Hendriksen, Liu and Ramousse, 2006; Koch, Hendriksen, Mogensen, Liu, Dekker, Rietveld, de Haart and Tietz, 2006; Lee, Heo, Lee, Kim, Kim, Lee, Song and Moon, 2003). For the Ni anode SOFC, there

are three anode degradation mechanisms (Yokokawa et al., 2008): 1) material transport mechanism; 2) thermo-mechanical mechanism; and 3) deactivation and passivation mechanism. There have been reports and observations of catastrophic mechanical failure of SOFCs during thermal cycling (Laurencin et al., 2009; Herbstritt, Krugel, Weber and Ivers-Tiffée, 2001; Selcuk, Merere and Atkinson, 2001; Sarantaridis, Rudkin and Atkinson, 2008; Faes, Nakajo, Hessler-Wyser, Dubois, Brisse, Modena and Van herle, 2009). As the operating temperature of a SOFC is typically above 600 °C, thermo-mechanical mechanism is likely the cause of such abrupt failure. Severe thermal stress induced by different material mechanical properties during the thermal cycling can make the interface layers to delaminate.

The two main failure modes of a SOFC, delamination and transgranular fracture, have been observed by several researchers. Peter Z. Cai *et al* (Cai, Green and Messing, 1997) investigated the constrained densification of Al₂O₃/ZrO₂ laminates fabricated by tape casting and sintering. Several kinds of damage or crack occurred during the process including channeling in the tensile layer, edge effect cracks, delamination or interface cracking, and cracks parallel to the interface in the compressive layer. An investigation in room and high temperature failure mechanisms in SOFC electrolytes was carried out by Lowries and Rawlings (Lowrie and Rawlings, 2000). They found that for 8mol% yttria-stabilized zirconia (YSZ), the room temperature flexure failure test was dependant on surface flaws with fracture initiating at porous defects. At higher temperatures, however, crack initiation and propagation mechanisms changed and fracture also occurred at featureless areas. Overall, the increase in temperature caused a 23-30% reduction in flexural strength. Experiments on

ceramic layers (Ni/YSZ-YSZ-LaMnO₃) under thermal shock loading revealed that the dominant failure modes to be transgranular fracture at locations of high thermal gradients and inter-granular at high temperature regions. Spalling failure of SOFC components was due to cracking normal to the planes, but interfacial cracking was also present (Busso, Tkach and Travis, 2001). The fracture toughness and stable crack growth behavior of the treated YSZ was investigated and was compared with that of pure YSZ by Kumar and Sørensen (Kumar and Sorensen, 2002). The crack mode for all the surface treated ceramics was found to be principally transgranular. Studies on production techniques found lower strengths for electrolyte-anode layers when sintered at higher temperatures due to higher interfacial fracture toughness deflecting cracking through the layers (Sorensen and Primdahl, 1998).

Cycling of SOFCs can cause thermo-mechanical degradation in material integrity and in performance, which increases rapidly with redox cycles and especially with thermal cycles. D. Sarantaridis et al (Sarantaridis et al., 2008) investigated oxidation failure modes of nickel based anode-supported SOFCs aiming at understanding how much oxidation such a cell can tolerate before catastrophic mechanical failure happens. Antonin Fase *et al* (Faes et al., 2009) carried on redox study of anode-supported SOFCs. They applied two techniques to quantify the anode expansion after a redox cycle of nickel at different temperatures. Both of D. Sarantaridis and A. Fase experiments showed the cracking of electrolyte after the cycling of SOFCs. As to the thermal cycling performance of SOFC, W. Bujalski *et al* (Bujalski, 2007) studied the transient performance of three types of SOFCs under different thermal cycling conditions in order to understand the degradation mechanisms. S. Taniguchi *et al*.

(Taniguchi, Kadowaki, Yasuo, Akiyama, Miyake and Nishio, 2000) have investigated electrolyte-supported planar SOFC. They found the electrolyte cracked in the area contacting glass sealing materials after one thermal cycle. The thermal cycling performance can be improved by modifying sealing materials and configuration. Hart *et al.* (Hart, 2004) investigated the thermal cycling of SOFC fabricated by screen printing. It was found that thermal cycling performance degraded greatly during the fifth cycle while the open circuit voltage (OCV) was not reduced significantly during the whole 10 cycles. Tang *et al.* (E. Tang, 2005) have investigated the thermal cycling performance of a anode-supported cell between 200 °C and 750 °C and reached 50 thermal cycles with average OCV loss of 1 mV·cycle⁻¹. Shiller *et al.* (G. Schiller, 2005) reported the results of thermal cycling performance of a metal supported SOFC. The electrode polarization resistance increased and OCV decreased, which was cycled between 180 °C and 800 °C for 10 thermal cycles. They concluded that the resistance increase indicated some minor electrode delamination and the drop of OCV could be due to the leakage as a result of crack formation in the electrolyte or at seals. Ellen Ivers-Tiffée *et al.* (Herbstritt et al., 2001) found that SOFC degradation caused by thermal cycling was mainly due to the electrode delamination. The delamination may happen after only several thermal cycles under specific operation conditions. Since the real delamination area was difficult to measure during thermal cycling, finite element (FE) and numerical analysis approaches have been used to estimate the area of delamination in SOFC. However, FE analysis requires a pre-existing crack tip or initial interfacial flaw in SOFC

structure (Sun, Liu, Stephens and Khaleel, 2008; Pitakthapanaphong and Busso, 2005; Herbristrit et al., 2001; Faes et al., 2009) and is usually confined to a specific configuration.

Currently, much attention has been focused on the analysis of SOFC performance under thermal cycling conditions. Much of the existing work, however, relied on finite element-based approach rather than modeling from first principles of delamination in layered structures. There have been very few thermo-mechanical modeling techniques that can be used to assess the reliability and durability of different configurations of SOFC. A fundamental theory-based numerical model is better suited for incorporation within a design and lifetime cycle prediction framework. In this paper, a multi-scale micromechanics model (Chandra, Huang, Jiang, Hu and Fu, 2000) capable of calculating thermal stresses and predicting crack nucleation has been developed. The model integrates thermal stress calculation into crack nucleation model to predict the SOFC lifetime. The model is capable of providing stress distribution and crack nucleation under thermal cycling conditions. This thermo-mechanical model is generalized and utilized for the lifetime prediction of SOFCs with different configurations.

2.3 SOFC Reliability and Lifetime Prediction Thermo-mechanical Modeling

A SOFC consists of an anode, electrolyte, and cathode. Amongst SOFCs, most widely used electrolyte is the YSZ ceramic, which exhibits high ionic conductivity, good thermal and chemical stability, and great mechanical strength at high temperatures (Yang, Li, Zhang, Bi, Peng, Chen and Liu, 2009; Brahim, Ringued, Gourba, Cassir, Billard and Briois, 2006; Han, Tang, Yin and Peng, 2007). Commonly, the anode is made of nickel yttria-stabilized

zirconia composites (Ni/8YSZ) and is usually 20-40% porous, which displays excellent catalytic properties for fuel oxidation and good current collection capability (Yu, Park, Lee and Woo, 2007; Haanappel, Mertens and Malzbender, 2007). Because Sr-doped lanthanum manganate ($\text{La}_{0.75}\text{Sr}_{0.2}\text{MnO}_3$) has high electronic conductivity and is also effective catalyst for the dissociation of O_2 , it has also been frequently used as cathode (Li, 2006; Leone, Santarelli, Asinari, Cal and Borchiellini, 2008). This study considers two variations of SOFC configuration: electrolyte-supported and anode-supported. Electrolyte-supported SOFC operates around 1000 °C. The thickness of an electrode is about 50 μm and that of electrolyte is thicker than 100 μm . In the anode-supported configuration, the electrolyte is usually very thin (less than 20 μm), and cathode is thicker than the electrolyte but much thinner than the anode (50 μm). The thickness of anode varies between 0.3 and 1.5 mm. Since the operating temperature is mainly determined by the nature of the electrolyte, such as the thickness of the electrolyte and its ionic conductivity (Ormerod, 2003), it can be lowered if the electrolyte becomes thin or has better ionic conductivity. Compared with electrolyte-supported SOFC with a much thicker electrolyte, an anode-supported SOFC operates at lower operating temperatures, typically 700-800 °C. Due to the thinner electrolyte thickness anode-supported SOFCs exhibit high electrochemical performance even at reduced temperatures with substantially lower ohmic resistance of the electrolyte (Zhonghe, Baolian, Zhenwei, Yonglai, Hejin, Yunchuan and Mojie, 2004; Laurencin et al., 2009; Yakabe, Baba, Sakurai and Yoshitaka, 2004).

The thermo-mechanical model consists of two parts: thermal stress calculation and crack nucleation, which is shown in Figure 4. The two thermal stresses, interfacial shear stress and peeling stress, are calculated from the mismatch of material mechanical properties of the cell layers. By applying the thermal stresses and using the Paris law (Anderson, 2005), the crack damage rate in a localized damaged area in the interfacial layer can be obtained. Then, the crack nucleation can be predicted from the crack damage rate and the initial damage distribution in the interfacial layer under the thermal cycling condition.

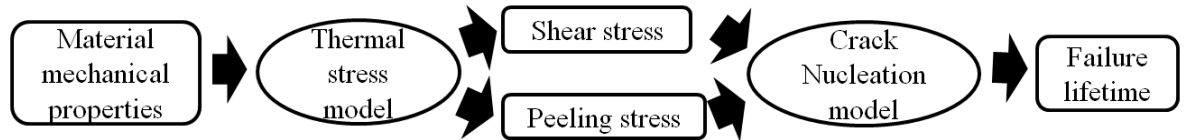


Figure 4. Schematic of the Concept of Modeling Approach

2.3.1 Modeling of Interfacial Shear Stress and Peeling Stress

Many studies (Zhang, Ohara, Maric, Okawa, Fukui, Yoshida, Inagaki and Miura, 2000; Maffei and de Silveira, 2003; Liu and Jiao, 2005; Tsoga, Gupta, Naoumidis and Nikolopoulos, 2000) show that an interfacial zone or layer exists between the electrolyte and electrode because of chemical reactions and diffusion under thermal and redox cycling. This interfacial zone or layer contains the electrochemically active sites and is vulnerable to microstructure changes during cell operation. Therefore, a hypothetical interfacial layer was assumed between the electrodes and the electrolyte, as shown in Figure 5, where $h_a \ll h_1$ and h_2 . The cell is subject to thermal cycling from room temperature to operating temperature, ΔT . Thermal cycling exists in the SOFCs operation, e.g., due to maintenance, fuel supply

interruption, or shut-down and restart of plant or device. Also, thermal cycling has been used as a method to investigate SOFC performance degradation and reliability of SOFC structure. A plane strain deformation was assumed in the analysis. Prior research (Busso et al., 2001; Cai et al., 1997; Kumar and Sorensen, 2002; Lowrie and Rawlings, 2000; Sorensen and Primdahl, 1998) suggested that the delamination and transgranular fracture are the two types of SOFC failure. Interfacial shear stress (τ) causes different adjacent layers to detach from each other in parallel direction, and peeling stress leads to different adjacent layers to detach in vertical direction (see Figure 6). These two types of thermal stresses in a multilayered structure lead to such failures seen in SOFCs. Based on the traction-free boundary condition at the free edge, the interfacial shear stress (τ) and the peeling stress (σ) near a free edge can be expressed as (Chandra et al., 2000; Wang, Huang, Chandra and Hu, 2000):

$$\tau_{interface} = \sigma_{thermal} \exp(-\xi x) \quad (1)$$

where,

$$\sigma_{thermal} = \frac{G_a}{h_a \xi} [(1 + \nu_1)\alpha_1 - (1 + \nu_2)\alpha_2] \Delta T \quad (2)$$

G_a is the shear modulus of the interfacial layer, and is expressed in the following form:

$$G_a = E_a / [2(1 + \nu_a)] E \quad (3)$$

Parameter ξ is given by,

$$\xi = 2 \sqrt{\frac{G_a}{h_a} \left(\frac{1}{E_1 h_1} + \frac{1}{E_2 h_2} \right)} \quad (4)$$

E_i' is the plane strain modulus, given by

$$E_i' = \frac{E_i}{1-\nu_i^2}, i = 1, 2 \quad (5)$$

The peeling stress developed by Jiang *et al.* (Jiang, Huang and Chandra, 1997) is obtained as,

$$\sigma_{peeling} = \zeta \sigma_{thermal} \sigma_0(x) \quad (6)$$

where,

$$\begin{aligned} \sigma_0(x) = & \exp(-\xi x) + \exp(-\chi x) \left(\frac{\xi^2}{2\chi^2} \sin(\chi x) \right. \\ & \left. - \left(\frac{\xi^2}{2\chi^2} + \frac{2\chi}{\xi} \right) \cos(\chi x) \right) \end{aligned} \quad (7)$$

Parameter χ and ζ are given by,

$$\chi = \left[3 \frac{E_a'}{h_a} \left(\frac{1}{E_1 h_1^3} + \frac{1}{E_2 h_2^3} \right) \right]^{1/4} \quad (8)$$

$$\zeta = \frac{3 \left(\frac{1}{E_1 h_1^2} - \frac{1}{E_2 h_2^2} \right) \frac{h_a}{G_a} \xi}{4(1-\nu_a) \left(\frac{1}{E_1 h_1} + \frac{1}{E_2 h_2} \right)^2 + 6 \left(\frac{1}{E_1 h_1^3} + \frac{1}{E_2 h_2^3} \right) \frac{h_a}{G_a}} \quad (9)$$

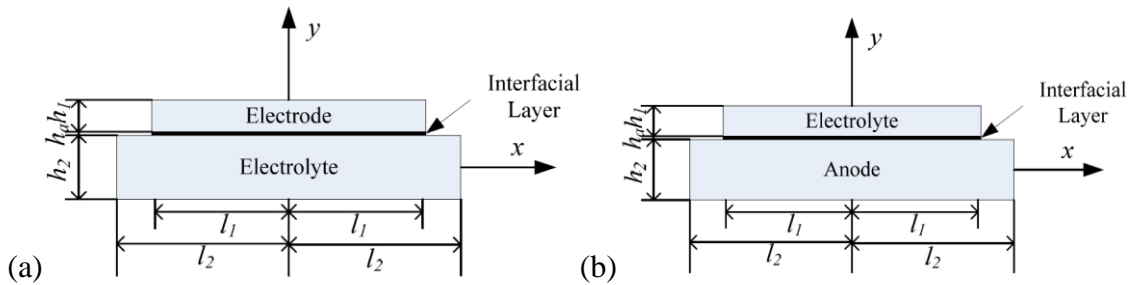


Figure 5. Schematic of Different SOFC Configuration (a) Electrolyte-supported (b) Anode-supported

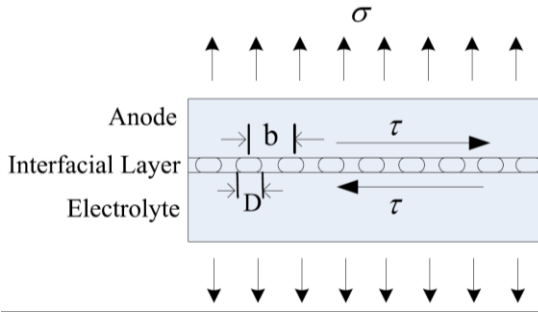


Figure 6. Schematic Diagram of Half-SOFC structure with an Isothermal and Porous Homogenous Interfacial Layer

2.3.2 Modeling of Crack Nucleation and Lifetime Prediction

When a multi-layer structure is subjected to thermal cycling, the fracture begins with nucleation of micro-defects, which are followed by propagation of micro-cracks. Eventually, it will lead to the fracture of the multi-layer structure.

The model developed by Huang *et al.* (Huang, Gong, Suo and Jiang, 1997) is generalized and applied to the SOFC structure shown in Figure 6. During the cyclic loading, a simple form of the kinetic equation can be taken from Paris' law (Anderson, 2005),

$$\frac{dD}{dN} = C \left(\frac{\Delta K}{E_a} \right)^n \quad (10)$$

D is the micro-crack size, C and n are material constants; N is the number of cycles. To simplify the calculation and analysis, ω is introduced as a non-dimensional damage parameter:

$$\omega = \frac{D}{b} \quad (11)$$

b is the micro-crack spacing (see Figure 3). If $\omega=0$, no damage is present. When $\omega=1$, the micro-crack has coalesced into a larger traction free crack and is considered as nucleation of a macroscopic crack. Therefore, for each loading cycle, the stress intensity factor changes,

$$\Delta K = \Delta\sigma \sqrt{2b \tan \frac{\pi D}{2b}} = \Delta\sigma \sqrt{2b \tan \frac{\pi}{2} \omega} \quad (12)$$

ΔK_I and ΔK_{II} are the different mode stress intensity factors. (ΔK_I means opening stress intensity factor variation (mode I) and ΔK_{II} means in plane shear stress intensity factor variation (mode II).) For the periodic thermal cycle, the cycle stress intensity factors are given by (H Tada, 1985).

$$\Delta K_I = \Delta\sigma \sqrt{2b \tan \frac{\pi}{2} \omega} \quad (13)$$

$$\Delta K_{II} = \Delta\tau \sqrt{2b \tan \frac{\pi}{2} \omega} \quad (14)$$

$\Delta\sigma$ and $\Delta\tau$ are the amplitudes of local cyclic normal and shear stresses, respectively. The fatigue growth rate described by Paris' law is expressed below, where β and n are material constants.

$$\frac{dD}{dN} = \beta (\sqrt{\Delta K_I^2 + \Delta K_{II}^2})^n \quad (15)$$

Because of the opening and sliding of micro-crack shown in Figure 6, there will be additional stretch v and additional sliding u across the localized damage band, which can be obtained by averaging the crack opening and crack sliding displacements in damaged layer,

$$v = \frac{1}{b} \int_{-D/2}^{D/2} \delta_{open} dx \quad (16)$$

$$u = \frac{1}{b} \int_{-D/2}^{D/2} \delta_{shear} dx \quad (17)$$

The crack opening and crack sliding displacement can be analyzed by using a configuration of periodical cracks described by Tada *et al.* (H Tada, 1985)

$$\delta_{open} = \frac{4\sigma b}{\pi E'} \cosh^{-1} \frac{\cos \frac{\pi x}{b}}{\cos \frac{\pi x}{2b}} \quad \text{for } |x| \leq D/2 \quad (18)$$

$$\delta_{shear} = \frac{4\tau b}{\pi E'} \cosh^{-1} \frac{\cos \frac{\pi x}{b}}{\cos \frac{\pi x}{2b}} \quad \text{for } |x| \leq D/2 \quad (19)$$

Additional cyclic stretching Δv and additional cyclic sliding Δu will generate because of the opening and sliding of the micro-cracks in the interfacial layer. The additional cyclic stretching Δv and additional cyclic sliding Δu can be obtained by substituting Equation (18) and (19) into Equations (16) and (17), respectively.

$$\Delta v = \left(\frac{4}{\pi}\right) \left(\frac{1-\nu^2}{E_a}\right) b \Delta \sigma \ln \left(\frac{1}{\cos\left(\frac{\pi D}{2b}\right)}\right) \quad (20)$$

$$\Delta u = \left(\frac{4}{\pi}\right) \left(\frac{1-\nu^2}{E_a}\right) b \Delta \tau \ln \left(\frac{1}{\cos\left(\frac{\pi D}{2b}\right)}\right) \quad (21)$$

Chandra *et al.* (Chandra et al., 2000) developed a model in which the localized band containing micro-cracks are modeled as an array of dislocation. Therefore, local normal stress $\Delta \sigma$ and local shear stress $\Delta \tau$ can be expressed as

$$\Delta\sigma(x) = \Delta\sigma_{peeling} - \frac{E_a}{4\pi(1-\nu_a^2)} \int_{-\infty}^{\infty} \frac{\partial\Delta v(\xi)}{\partial\xi} * \frac{d\xi}{x-\xi} \quad (22)$$

$$\Delta\tau(x) = \Delta\tau_{interface} - \frac{E_a}{4\pi(1-\nu_a^2)} \int_{-\infty}^{\infty} \frac{\partial\Delta u(\xi)}{\partial\xi} * \frac{d\xi}{x-\xi} \quad (23)$$

Normalizing the variables in those equations above, the following non-dimensional parameters are obtained (Chandra et al., 2000):

$$\begin{aligned} \sigma' &= \frac{\Delta\sigma}{\sigma_{thermal}}, \tau' = \frac{\Delta\tau}{\sigma_{thermal}} \\ v' &= \frac{\Delta v}{\frac{b\sigma_{thermal}(1-\nu_a^2)}{E_a}}, u' = \frac{\Delta u}{\frac{b\sigma_{thermal}(1-\nu_a^2)}{E_a}}, x' = \frac{x}{b} \end{aligned} \quad (24)$$

Then, Equations (20), (21), (22) and (23) can be rewritten as:

$$v' = \frac{4}{\pi} \sigma' \ln \frac{1}{\cos(\frac{\pi}{2} \omega)} \quad (25)$$

$$u' = \frac{4}{\pi} \tau' \ln \frac{1}{\cos(\frac{\pi}{2} \omega)} \quad (26)$$

$$\sigma' = \zeta\sigma_0(x) - \frac{1}{4\pi} \int_{-\infty}^{\infty} \frac{\partial v'}{\partial \xi'} * \frac{d\xi'}{x' - \xi'} \quad (27)$$

$$\tau' = \exp(-\lambda x) - \frac{1}{4\pi} \int_{-\infty}^{\infty} \frac{\partial u'}{\partial \xi'} * \frac{d\xi'}{x' - \xi'} \quad (28)$$

Therefore, the damage growth rate obtained from Equation (15) can be expressed as:

$$\frac{d\omega}{dN'} = (\tan \frac{\pi}{2} \omega)^{n/2} (\sigma' + \tau')^{n/2} \quad (29)$$

The damage distribution $\omega(x)$ is updated with an increment of cycle $\Delta N'$ for the next cycle number $N'+\Delta N'$.

The critical thermal cycle is denoted by $N_{nucleation}$, which is the maximum number of thermal cycles the material can sustain before a macroscopic crack appears in the interfacial layer. $N_{nucleation}$ depends on the material property, $\sigma_{thermal}$ and the initial damage distribution. Following Ohno and Hutchinson (Ohno and Hutchinson, 1984) and Chandra (Chandra et al., 2000), the initial distribution of damage is used to represent a cluster of damage in the interfacial layer around the electrode edge.

$$\omega(x) = \omega_{average} + (\omega_{max} - \omega_{average}) \exp\left[-\frac{1}{2} \left(\frac{x}{\lambda b}\right)^2\right] \quad (30)$$

$\omega_{average}$ and ω_{max} are the average and maximum damage level in the band. The damage distribution depends much more greatly on ω_{max} than on λ (Chandra et al., 2000). Since the anode layer is porous structure, the analysis of SOFC structure life prediction is based on the initial damage parameters $\omega_{average} = 0.1$, $\omega_{max} = 0.6$ (porosity $p=47\%$), $\omega_{max} = 0.5$ (porosity $p=32\%$), $\omega_{max} = 0.4$ (porosity $p=17\%$).

2.4 Material Properties for the Cell and Model Validation

The modeling results have been compared with two different experimental cases. Parameters used in the simulation for the two cases are summarized in Table 1. The material properties of different SOFC cell layer used in the validation were chosen from previous literatures (Aruna, Muthuraman and Patil, 1998; Tietz, 1999; Atkinson and Selcuk, 2000; Miladin and Edgar, 2004a; 2004b; Nakajo, Stiller, Härkegård and Bolland, 2006; Mori,

Yamamoto, Itoh, Inaba and Tagawa, 1998; Sameshima, Ichikawa, Kawaminami and Hirata, 1999; Pihlatie, Kaiser and Mogensen, 2008). In Case 1 (Waldbillig, Wood and Ivey, 2005), it was assumed that the critical thermal cycle for failure was reached when the redox cycle caused significant cell voltage degradation. The modeling calculated critical thermal cycle $N_{nucleation} = 9$, which was almost the same with the value reported in D. Waldbillig *et al* experiment (Waldbillig et al., 2005) (8 cycles). In Case 2 (Laurencin et al., 2009), the critical thermal cycle for failure was estimated by the dramatically increased specific ohmic resistance. The modeling calculated critical thermal cycle $N_{nucleation} = 8$, which was in agreement with the cycle number (9 cycles) in J. Laurencin *et al* experiment (Laurencin et al., 2009).

The material properties of different components of a typical electrolyte-support or anode-supported SOFC (NiO-8YSZ/YSZ/LSM) are chosen from relevant literatures (Giraud and Canel, 2008; Mori et al., 1998; Pihlatie et al., 2008; Sameshima et al., 1999; Atkinson and Selcuk, 2000) and are summarized in Table 2. Solid state reaction and inter-diffusion phenomena result in the formation of an interaction zone between the electrodes and the electrolyte under SOFC thermal and redox cycling (Tsoga et al., 2000), which forms an interfacial layer reported in (Zhang et al., 2000; Liu and Jiao, 2005). The material properties of the interfacial layer are assumed to be between those of the electrode and the electrolyte respectively as shown in Table 2. Based on the interfacial zone or layer thickness in those experiments (Tsoga et al., 2000; Zhang et al., 2000; Liu and Jiao, 2005), the interfacial layer in the modeling calculation is assumed to be 1 μm .

Table 1. Material properties and geometries used for model validation

Layer	Young's Modulus (GPa)	Poisson Ratio	Thickness (μm)	CTE ($\times 10^{-6} \text{ } ^\circ\text{C}^{-1}$)	ΔT ($^\circ\text{C}$)	Number of cycle at failure	
						Experiment	Calculated
Case 1 (Waldbillig et al., 2005)						8	9
Anode (Ni/8YSZ)	60 (Pihlatie et al., 2008)	0.3 (Atkinson and Selcuk, 2000; Giraud and Canel, 2008)	1000	12.5 (Mori et al., 1998; Sameshima et al., 1999)	750		
Electrolyte (YSZ)	200 (Pihlatie et al., 2008)	0.31 (Atkinson and Selcuk, 2000; Giraud and Canel, 2008)	10	10.8 (Mori et al., 1998; Sameshima et al., 1999)			
Case 2 (Laurencin et al., 2009)						9	8
Anode (Ni/8YSZ)	56.8 (Miladin and Edgar, 2004a; 2004b)	0.258 (Miladin and Edgar, 2004a; 2004b)	1500	12.5 (Tietz, 1999)	780		
Electrolyte (YSZ)	190 (Atkinson and Selcuk, 2000)	0.308 (Atkinson and Selcuk, 2000)	10	10.8 (Aruna et al., 1998; Nakajo et al., 2006)			

*As to case 1, the material property is assumed based on product from Versa Power System Ltd. with 40% porosity anode and 5% porosity electrolyte

Table 2. Material properties and geometries used for the calculation of thermal stresses and lifetime prediction

Layer	Young's Modulus (GPa)	Poisson Ratio	Thickness (μm)	CTE ($\times 10^{-6} \text{ } ^\circ\text{C}^{-1}$)
Electrolyte-supported SOFC				
Anode (Ni/8YSZ)	220 (Giraud and Canel, 2008; Pihlatie et al., 2008)	0.3 (Atkinson and Selcuk, 2000; Giraud and Canel, 2008)	10,25,40,	12.5 (Mori et al., 1998; Sameshima et al., 1999)

Table 2. (continued)

Layer	Young's Modulus (GPa)	Poisson Ratio	Thickness (μm)	CTE ($\times 10^{-6} \text{ } ^\circ\text{C}^{-1}$)
Electrolyte (YSZ)	205 (Giraud and Canel, 2008; Pihlatie et al., 2008)	0.31 (Atkinson and Selcuk, 2000; Giraud and Canel, 2008)	250	10.3 (Mori et al., 1998; Sameshima et al., 1999)
Cathode (LSM)	114 (Giraud and Canel, 2008; Pihlatie et al., 2008)	0.28 (Atkinson and Selcuk, 2000; Giraud and Canel, 2008)	25	12.4 (Mori et al., 1998; Sameshima et al., 1999)
Interfacial layer*	213/160	0.3	1	11.4
Anode-supported SOFC				
Anode (Ni/8YSZ)	220 (Giraud and Canel, 2008; Pihlatie et al., 2008)	0.3 (Atkinson and Selcuk, 2000; Giraud and Canel, 2008)	1000	12.5 (Mori et al., 1998; Sameshima et al., 1999)
Electrolyte (YSZ)	205 (Giraud and Canel, 2008; Pihlatie et al., 2008)	0.31 (Atkinson and Selcuk, 2000; Giraud and Canel, 2008)	10,20,30,	10.3 (Mori et al., 1998; Sameshima et al., 1999)
Cathode (LSM)	114 (Giraud and Canel, 2008; Pihlatie et al., 2008)	0.28 (Atkinson and Selcuk, 2000; Giraud and Canel, 2008)	25	12.4 (Mori et al., 1998; Sameshima et al., 1999)
Interfacial layer*	213/160	0.3	1	11.4

*The material properties of interfacial layer are assumed between those of anode of electrolyte

Since the electrode is a porous structure, its Young's modulus E changes with different porosity. The apparent modulus, E_I can be calculated as a function of porosity for the same pore structure with semi-empirical correlations. Since the average porosity of anode layer is about 20-40%, three porosities (17%, 32% and 47%) are chosen to analyze the effect of electrode porosity on peeling stress (σ) and interfacial stress (τ). Based on the

correlation described in relevant literature (Wang, 1984), the corresponding E_I with different porosities is summarized and shown in Table 3.

Table 3. Young's modulus of electrode at different porosities

Porosity	Anode (GPa)		Cathode (GPa)		Interfacial layer (GPa)	
	E_0	E_I	E_0	E_I	E_0	E_I
17%	220	99	114	51	213/160	96/72
32%	220	79	114	40	213/160	76/57
47%	220	30	114	15	213/160	29/22

2.5 Results and Discussion

2.5.1 Sensitivity Analysis of Thermal Stresses

The thermal stresses of anode-electrolyte and cathode-electrolyte interfaces are compared in Figure 7. The thermal stresses between the anode and electrolyte interface are larger than those between the cathode and electrolyte, and therefore, anode and electrolyte interface is more likely to crack or delaminate under the combined peeling and interfacial shear stresses. This result is in good agreement with other research results reporting delamination susceptibility of the anode-electrolyte interface (Zhang, Zhu, Huang, Xie and Xin, 2008; Laurencin, Delette, Lefebvre-Joud and Dupeux, 2008; Hsiao, 1997). Moreover, the degradation of the anode microstructure mainly determines the overall cell electrical performance (Fukui et al., 2002; Hagen et al., 2006; Koch et al., 2006; Lee et al., 2003), and therefore, anode-electrolyte was chosen as the focus of this study.

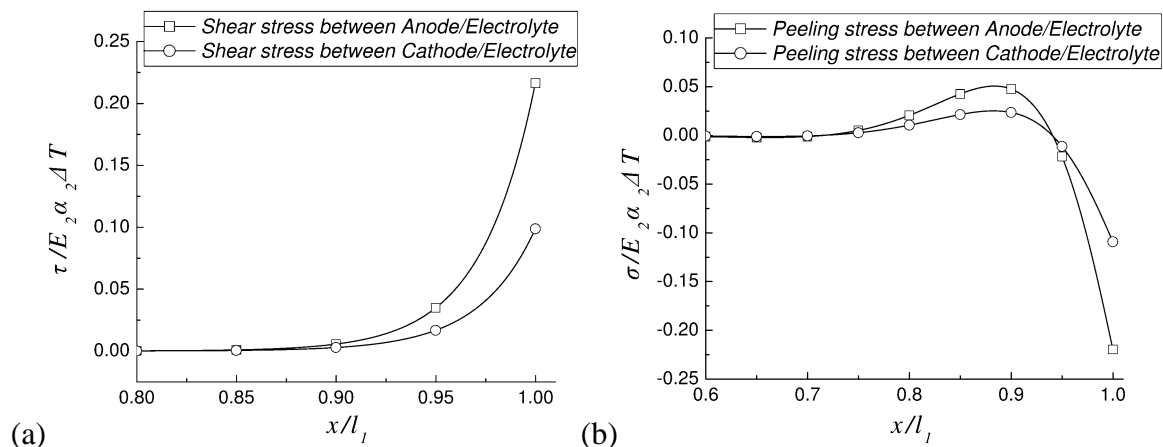


Figure 7. Thermal Stress Comparison with Anode-electrolyte and cathode-electrolyte in Electrolyte-supported SOFC: (a) Shear Stress (b) Peeling Stress

Figure 5 shows anode porosity effects on interfacial shear and peeling stresses in electrolyte supported SOFC. With the increase of anode porosity, the interfacial shear stress and peeling stress decrease. When the anode porosity increases from 17% to 47%, the interfacial shear stress almost doubles. The location of peeling stress peak indicates a vulnerable region, which would likely crack or delaminate first. The interfacial shear stress is nearly zero around the center of the specimen and increases sharply towards the edge because of the combined effect of material and geometrical singularities. The peeling stress undergoes severe change from a maximum tensile value to compressive stress near the edge. This trend is similar to layered assemblies under the thermal cycling condition (Wang and Zeng, 2008). The combination of these two stresses reaches maximum around the edge of electrode, which is in good agreement with other simulations and measurements made in a similar SOFC configuration. Based on the Weibull approach for failure prediction in a

similar SOFC configuration, J. Laurencin *et al* (Laurencin et al., 2008; Laurencin et al., 2009) predicted that the region around the interfacial area at the edge of electrolyte-electrode will first show signs of damage under thermal cycling. This prediction is confirmed by experimental results by A. Selcuk *et al* (Selcuk et al., 2001), which shows a partial delamination of the anode layer edge on the YSZ electrolyte (see Figure 9).

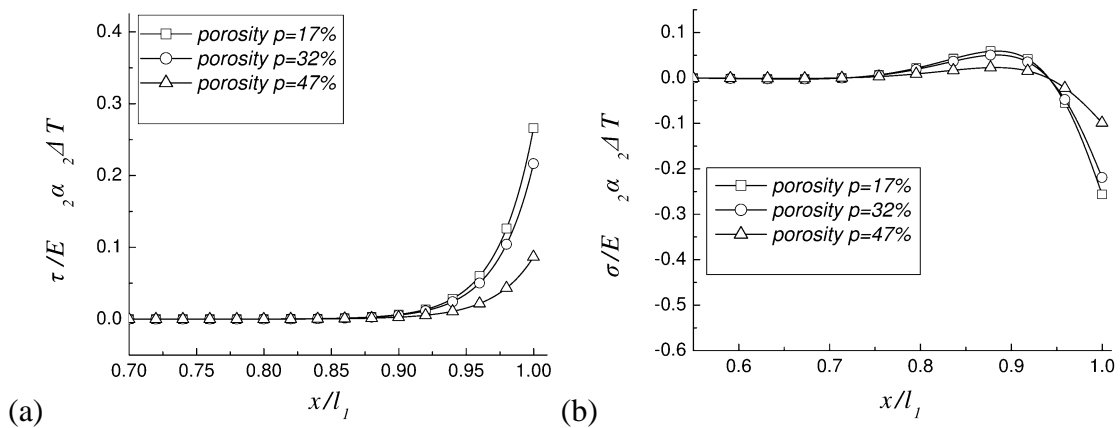


Figure 8. Thermal Stress Comparison with Different Porosity in Electrolyte-supported SOFC: (a) Shear Stress (b) Peeling Stress

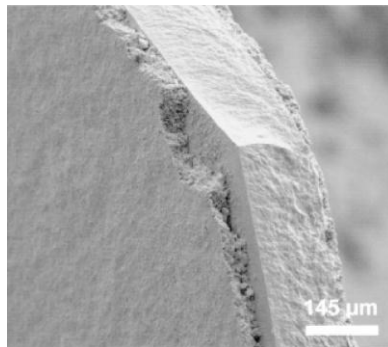


Figure 9. SEM Image of a Partially Delaminated Anode Layer on YSZ Electrolyte (Koch et al., 2006)

The effect of anode thickness on interfacial shear and peeling stresses is shown in Figure 10. With the increase of anode thickness, the thermal stresses increase. For example,

if the anode thickness increases from 10 to 40 μm , the interfacial shear stress is almost doubled. Experiment and simulation results performed by H. Yakabe *et al* (Yakabe et al., 2004) show that the thermal stresses measured by X-ray diffraction in the cell increases with the increase in anode thickness.

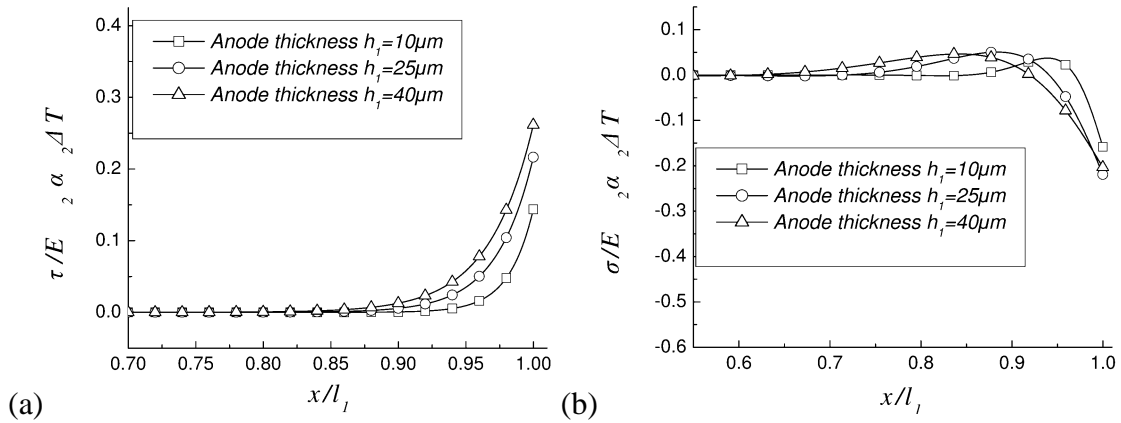


Figure 10. Thermal Stress Comparison with Different Thickness in Electrolyte-supported SOFC: (a) Shear Stress (b) Peeling Stress

Anode porosity effect on interfacial shear stress and peeling stress in anode-supported SOFC is shown in Figure 11. The interfacial shear stress and peeling stress have similar trends with those in electrolyte-support SOFC shown in Figure 8. The peak value of tensile stress and the amplitude of peeling stress are larger than those in an electrode-supported SOFC (Figure 12).

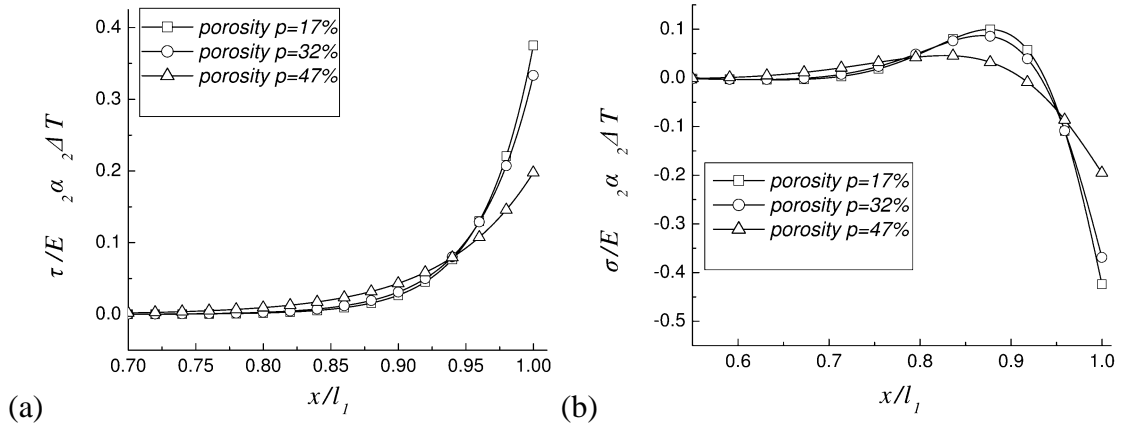


Figure 11. Thermal Stress Comparison with Different Porosity in Anode-supported SOFC: (a) Shear Stress (b) Peeling Stress

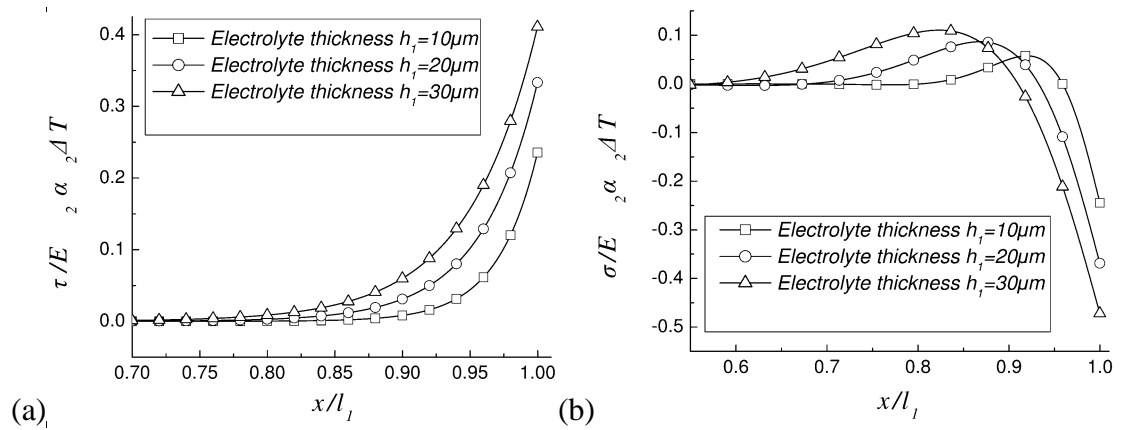


Figure 12. Thermal Stress Comparison with Different Thickness in Anode-supported SOFC: (a) Shear Stress (b) Peeling Stress

2.5.2 Crack Nucleation and Cell Lifetime Prediction under Thermal Cycling Conditions

Based on the distribution of thermal stresses, the crack nucleation model described in section 2.3 can predict the damage evolution in the local damage area of the interfacial layer.

A typical damage evolution curve is shown in Figure 13. The propagation of damage accelerates as the cells undergo thermal cycling. The anode-supported SOFC also showed a similar trend.

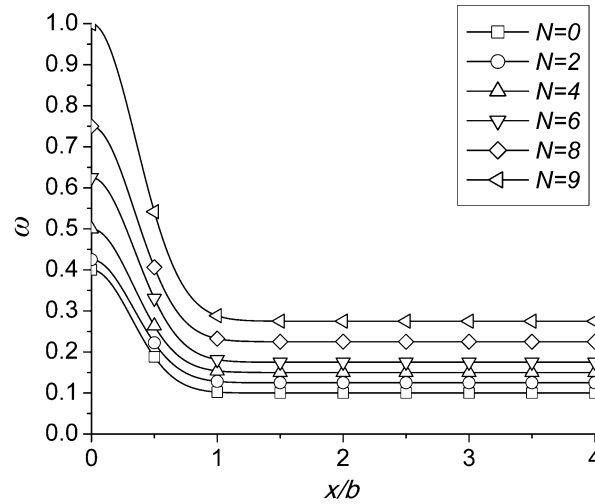


Figure 13. Damage Evolution in Electrolyte-supported SOFC ($\omega_{\max} = 0.4$ and the Anode Layer Porosity $p = 47\%$)

It can be seen from Figure 14, the critical thermal cycles for both electrolyte-supported SOFC and anode-supported SOFC decrease with the increase of porosity. Although the increasing porosity of anode reduces the thermal stresses under thermal cycling, it increases the initial damage distribution, which also greatly influences the damage evolution. For example, ω_{\max} increases from 0.4 to 0.6 with the porosity increasing from 17% to 47%, which has great influence on the critical thermal cycles for failure (see Equation (30)). That is the reason for the decrease in the thermal cycle numbers to failure with the increase in anode porosity.

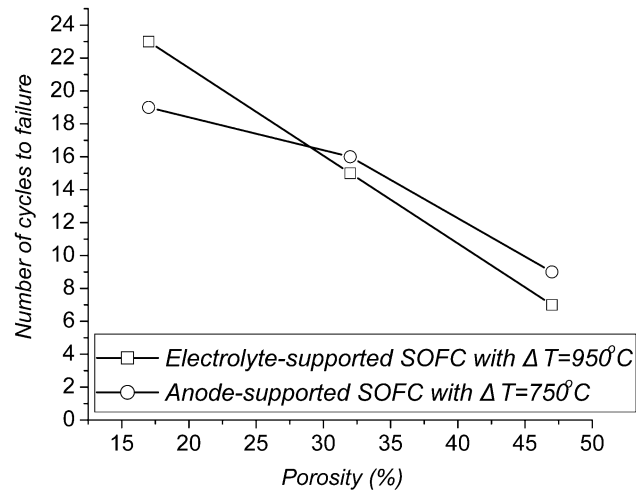


Figure 14. Anode Porosity Effect on Number of Cycles to Failure in Different SOFC Configurations

The effects of anode thickness variation and electrolyte thickness variation on critical thermal cycle are shown in Figure 15. It can be clearly concluded that the number of thermal cycles to failure decreases with the increase of anode thickness or electrolyte thickness.

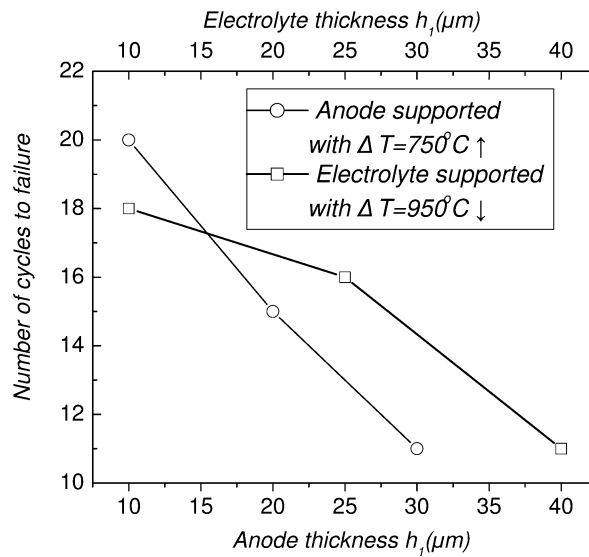


Figure 15. Anode Thickness Effect on Critical Thermal Cycle

2.6 Conclusions

The modeling approach considered thermal stresses, i.e. interfacial shear stress and peeling stress, arising from the material mismatch between the electrode and electrolyte, and integrated them into the crack propagation model to predict the number of cycles to cell failure. Numerical results were validated against available experimental results, which showed a good agreement. Following conclusion has been drawn from this study.

- The model can effectively provide insight into the evolution and distribution of the thermal stresses during thermal cycling and predict the lifetime of the cell in different configurations.
- The interfacial shear stress and peeling stress were more concentrated near the free edge of SOFCs, which theoretically explains the damage near the cell edges frequently observed in experiments under thermal cycling conditions.
- For the case of nickel-based SOFCs, the anode-electrolyte interface was found to be more prone to delamination under thermal cycling conditions, which explains the high possibility of anode delamination in the electrolyte-supported SOFC in the reported experiments.

The effects of structural and geometric parameters on the cell lifetime under thermal cycling conditions were investigated. As the porosity and the thickness of anode increased, the lifetime of the cell decreased for the electrolyte-supported cell. A similar trend was found for the anode-supported structure when electrolyte porosity and thickness were varied.

CHAPTER 3. FABRICATION OF SOLID OXIDE FUEL CELL ANODE ELECTRODE BY SPRAY PYROLYSIS

3.1 Introduction

Solid oxide fuel cells (SOFCs) are an electrochemical energy conversion device that can directly convert chemical fuel to electrical power with high efficiency and low emission of pollutants. Solid oxide fuel cells (SOFCs) are an electrochemical energy conversion device that can directly convert chemical fuel to electrical power with high efficiency and low emission of pollutants. One of the research efforts has been focusing on improving the performance of the SOFC electrodes (Jiang, Wang and Zhen, 2005; Yoon, Nam, Han, Lim, Hong and Hyun, 2004; Ali, Wen, Nandakumar, Luo and Chuang, 2008; Uchida, Arisaka and Watanabe, 2000). The reactions in the electrodes occur at triple phase boundary (TPB) sites, where the reactant gas comes into contact with an electronic conductor and an ionic conductor (O'Hayre, Barnett and Prinz, 2005a). Therefore, a SOFC electrode with greater TPBs provides more reaction sites, leading to an increase in electrical power output and better electrochemical performance. In the meanwhile, a highly porous electrode is required to efficiently supply fuel gas to the TPB sites. Therefore, designing and controlling the porous structure of an electrode is critical in improving the cell performance (Tanner, Fung and Virkar, 1997; Deseure, Bultel, Dessemond and Siebert, 2005a; Greene, Chiu and Medeiros, 2006). There have been efforts to improve the performance by introducing interface layers and making functionally graded electrodes. Nanocrystalline electrolyte-

electrode interfacial layer has shown to increase the power output by more than 20% (Stoermer, Rupp and Gauckler, 2006). The functionally graded electrodes also showed better electrochemical performance than conventional SOFCs (Will, Mitterdorfer, Kleinlogel, Perednis and Gauckler, 2000; Jono, Suda and Hattori, 2007a).

Various techniques have been investigated by scientists for the fabrication of electrodes, such as tape casting (Song, Park, Lee and Kim, 2008), screen printing (Rotureau, Viricelle, Pijolat, Caillol and Pijolat, 2005), spin coating (Xu, Xia, Huang and Peng, 2005a), tape calendaring (Minh, 2004), thermal plasma spraying (Hui, Wang, Kesler, Rose, Jankovic, Yick, Maric and Ghosh, 2007), electrostatic spray deposition (Nguyen and Djurado, 2001), and spray pyrolysis (Chang, Hsu and Hwang, 2008). These techniques have been summarized and compared in Table 4 (Flesner, 2009). Spray pyrolysis is one of the most cost effective and versatile deposition techniques. It only requires a simple apparatus to deposit thin films of various materials under atmospheric condition. Compared with other techniques, spray pyrolysis has the capability to control particle shape, particle size, composition, and phase homogeneity of the deposited film. It has a great potential for producing functionally graded electrodes, which require deposition of multiple layers with gradually changing particle size, composition and/or porosity. Moreover, spray pyrolysis is compatible with large scale industry manufacturing for deposition of thin and porous films due to a wide selection of precursors and low equipment cost for mass production.

Several types of spray pyrolysis have been investigated to fabricate electrode layers in SOFCs. Electrostatic spray pyrolysis was used to make NiO-Samaria-doped ceria (SDC),

YSZ and lanthanum strontium manganite (LSM) (Xie, Neagu, Hsu, Zhang and Deces-Petit, 2007; Wilhelm, Pratsinis, Perednis and Gauckler, 2005; Nguyen and Djurado, 2001; Princivalle, Perednis, Neagu and Djurado, 2004). Porous electrode films of $\text{La}_{0.6}\text{Sr}_{0.4}\text{Co}_{0.2}\text{Fe}_{0.8}\text{O}_{3-\delta}$ (Beckel, Dubach, Studart and Gauckler, 2006) and Ni/CGO (Muecke, Messing and Gauckler, 2009) have been fabricated by gas pressurized spray pyrolysis. An ultrasonic spray pyrolysis, which uses ultrasonic vibration to atomize the precursor solution, has been investigated to fabricate SOFC electrodes, as well. Hamedani et al. (Hamedani, Dahmen, Li, Peydaye-Saheli, Garmestani and Khaleel, 2008) fabricated a gradient porous LSM cathode, and Moe et al. (Moe, K, Tagawa, T, Goto and S, 1998) prepared $\text{La}_{1.8}\text{Al}_{0.2}\text{O}_3$ anode using ultrasonic spray pyrolysis. Chen et al. (Chen and Hwang, 2008; Chang et al., 2008) deposited Ni-CGO anode by electrostatic-assisted ultrasonic spray pyrolysis to reduce the loss of aerosol stream to open air. However, none of the studies on ultrasonic spray pyrolysis investigated porosity of the deposited electrode, which can influence the electrode performance (Zhao and Virkar, 2005). Studies in applying spray pyrolysis for SOFC manufacturing are still very limited and further experiments accompanied by modeling are needed.

Table 4. Comparison of SOFC fabrication techniques (Flesner, 2009)

Fabrication Technique	Grading capability	Cost (time/complexity)	Porosity	Deposited Film Thickness
Tape casting	Poor	High	0-60	>7 μm
Screen printing	Poor	High	0-60	>8 μm
Spin coating	Yes	High	0-60	>1 μm
Tape calendaring	Poor	Low	N/A	N/A
Thermal plasma spray	Yes	Low	5-20	>Particle size
Electrostatic spray deposition	Yes	High	0-60	>Particle size
Spray pyrolysis	Yes	Medium	0-55	>Particle size

In this study, the ultrasonic spray pyrolysis was investigated for deposition of SOFC anode electrode to assess its capability to control the microstructure. A detailed experimental work was performed to deposit nickel and $\text{Ce}_{0.9}\text{Gd}_{0.1}\text{O}_{1.95}$ on an yttria stabilized zirconia (YSZ) substrate. First, an ultrasonic atomization model was utilized to predict the deposited particle size (Section 3.4). Second, the effects of various process parameters, which included deposition time (Section 3.5.2), precursor solution concentration (Section 3.5.3), deposition temperature (Section 3.5.4) and precursor solution feed rate (Section 3.5.5), on the microstructure and the porosity of deposited film were investigated. Among the parameters, precursor solution concentration and deposition temperature had the most significant effect on the microstructure.

3.2 Experimental Procedures and Materials

3.2.1 Experimental Setup

The spray pyrolysis experimental setup is shown in Figure 16. It consists of a carrier gas delivery system, a syringe pump, an ultrasonic nebulizer and a hot plate. The process can be divided into three main steps: atomization of precursor solution, transportation of the aerosol by the carrier gas, and deposition-decomposition of the precursor solution on the heated substrate. The system was designed to avoid deposition of large droplets formed by occasional variation of the ultrasonic nebulizer. It can effectively reduce the variation of atomized droplets, which will improve the uniformity of the deposited microstructures in the film. The precursor solution was atomized by ultrasonic nebulizer (Sonics[®] VC) operating at 60 kHz. The atomized aerosol was carried through a glass tube by the nitrogen (N₂) carrier gas at a flow rate (Q) of 1.5 l min^{-1} . The substrate was placed at the center of the hot plate. The distance between the tip of glass tube and substrate was fixed at 6 cm.

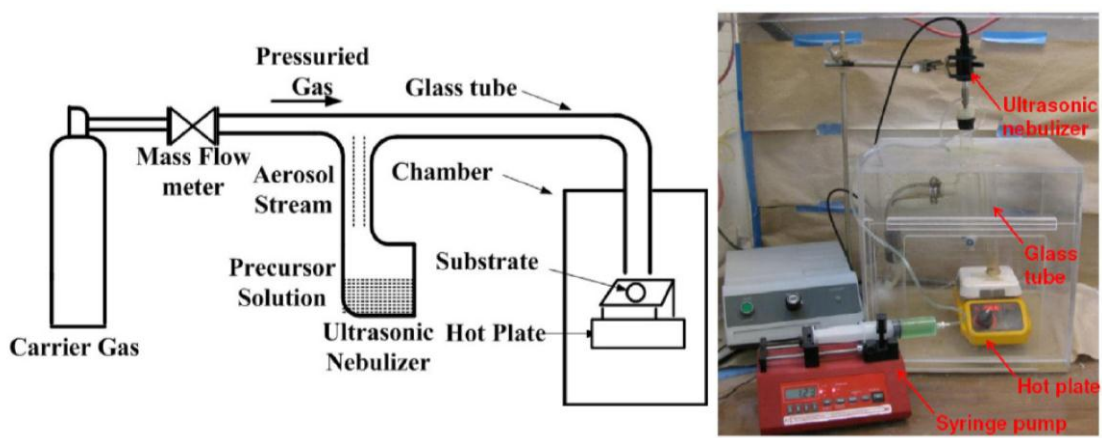


Figure 16. Spray Pyrolysis Experiment Setup

3.2.2 Materials and Precursor Solution Preparation

In this study, 8 mol.% YSZ has been selected as the electrolyte material due to its wide use and affordability (Prabhakaran, Beigh, Lakra, Gokhale and Sharma, 2007; Zhao, Li, Ju and Pal, 2008; Simwonis, Thülen, Dias, Naoumidis and Stöver, 1999). YSZ buttons (FCM[®]) were 20 mm in diameter and 270 μm in thickness. For the anode material, Ni/CGO was selected. Ni/CGO ($\text{Ce}_{0.9}\text{Gd}_{0.1}\text{O}_{1.95}$) is considered one of the state-of-the-art anode materials due to its high ionic conductivity, high electronic conductivity and high thermal-chemical stability, particularly with YSZ electrolyte (Chen, Zhe, Ai, Chen, Hu, Huang and Su, 2007; Van herle, Ihringer, Vasquez Cavieres, Constantin and Bucheli, 2001; Chourashiya, Pawar and Jadhav, 2008; Shi, Liu, Xu, Wang, Yuan, Majewski and Aldinger, 2005; Steele, 2000; Kharton, Figueiredo, Navarro, Naumovich, Kovalevsky, Yaremchenko, Viskup, Carneiro, Marques and Frade, 2001; Higashinakagawa, Sameshima and Hirata, 2004; Suda, Itagaki, Node, Takahashi, Kawano, Yoshida and Inagaki, 2006; Xie et al., 2007).

The precursor solution was prepared using a similar method proposed in (Chen and Hwang, 2008). Nickel (II) nitrate hexahydrate (98%, $\text{N}_2\text{NiO}_6 \cdot 6\text{H}_2\text{O}$; Alfa Aesar), cerium (III) nitrate hexahydrate (99.5%, $\text{Ce}(\text{NO}_3)_3 \cdot 6\text{H}_2\text{O}$; Alfa Aesar) and gadolinium (III) nitrate hydrate (99.9%, $\text{Gd}(\text{NO}_3)_3 \cdot x\text{H}_2\text{O}$, $x \approx 6$; Alfa Aesar) were dissolved in the solution of diethylene glycol mono-n-butyl ether (99%, $\text{HOCH}_2\text{CH}_2\text{OCH}_2\text{CH}_2\text{O}(\text{CH}_2)_3\text{CH}_3$; Alfa Aesar) and ethyl alcohol (99.5%, $\text{C}_2\text{H}_5\text{OH}$; Decon) at a volume ratio of 1:1. The molar ratio of Ni to CGO was chosen as 6:4 based on the research conducted by Chen et al. (Chen and Hwang, 2008), which resulted in the best performance in their study. Precursor solutions were

prepared so that the total concentration of metal ions can be varied between 0.025 mol l^{-1} and 0.4 mol l^{-1} .

3.2.3 Anode Film Deposition and Measurement

Three processing variables were investigated: precursor solution concentration (C), deposition temperature (T) and precursor solution feed rate (L). The full experiment matrix is summarized in Table 5. All the deposited samples were annealed at 800°C for 2 hours to promote crystallization of the deposited films at the heating and cooling rate of $5^{\circ}\text{C min}^{-1}$. The morphology and composition of the deposited anode film were examined by scanning electron microscope (JEOL JSM-606LV) and energy dispersive X-ray spectrometer (INCA mics/x-stream/SEM TVA3). Siemens D-500 X-ray diffraction system was used to obtain the X-ray diffraction (XRD) pattern of the deposited samples. SEM images were analyzed by commercial software, ImageJ, to calculate the porosity values.

Table 5. Experimental Matrix Used in the Study

#	Precursor solution concentration ($mol\ l^{-1}$)	Deposition temperature ($^{\circ}C$)	Precursor solution feed rate ($ml\ min^{-1}$)
1	0.4	250	1.23
2	0.4	300	1.23
3	0.4	350	1.23
4	0.1	250	1.23
5	0.1	300	1.23
6	0.1	350	1.23
7	0.025	250	1.23
8	0.025	300	1.23
9	0.025	350	1.23
10	0.4	250	1.78
11	0.4	300	1.78
12	0.4	350	1.78
13	0.1	250	1.78
14	0.1	300	1.78
15	0.1	350	1.78
16	0.025	250	1.78
17	0.025	300	1.78
18	0.025	350	1.78

3.3 Ultrasonic Atomization Modeling

3.3.1 Modeling of Deposited Particle Size

Understanding the relation among the ultrasonic atomization parameters can aid design and control of the deposited microstructure. However, only few studies have made efforts to model the deposited particle size in a SOFC. In this study, we employed the work by Jokanovic et al. (Jokanović, 1996; Jokanović, Spasić and Uskoković, 2004). The governing equation for ultrasonically atomized aerosol droplet in the ellipsoidal form is (Jokanovic, Janackovic and Uskokovic, 1999):

$$\rho \frac{\partial^2 \phi}{\partial t^2} \Big|_{r=R} - \frac{\sigma}{R^2} \left\{ 2 \frac{\partial \phi}{\partial r} + \frac{\partial}{\partial r} \left[\frac{1}{\sin \theta} \frac{\partial(\sin \theta \frac{\partial \phi}{\partial \theta})}{\partial \theta} + \frac{1}{\sin^2 \theta} \frac{\partial^2 \phi}{\partial \varepsilon^2} \right] \right\} = 0 \quad (1)$$

where ϕ is the rate potential of excitation precursor; r is radius of the aerosol droplet; and ε and θ are angles corresponding to the equation transformed into polar coordinates. The solution of Eqn. (1) can be obtained in the following form (Jokanovic et al., 1999):

$$\rho \omega^2 + \frac{l\sigma}{R^3} [2 - l(l+1)] = 0 \quad (2)$$

where ω is the spherical frequency of ultrasonic wave oscillation. The average diameter of an aerosol droplet (d_d) is obtained by solving Eqn. (2) (Jokanovic et al., 1999),

$$d_d = 2 \frac{\sqrt[3]{2}}{\pi} \left(\frac{\pi \sigma}{\rho f^2} \right)^{1/3} \quad (3)$$

where σ is the surface tension of the precursor solution, ρ is the precursor solution density, and f is the frequency of the ultrasonic nebulizer.

The diameter of discharged aerosol droplet from the nebulizer decreases during the solidification and pyrolysis steps. The eventual deposited particle diameter (d_p) can be expressed by the following formula (Jokanovic et al., 1999),

$$d_p = d_d \left(\frac{c_{pr} M_p}{\rho_p M_{pr}} \right)^{1/3} \quad (4)$$

where c_{pr} is the precursor solution concentration, M_p is the powder molecular mass, ρ_p is the powder density, and M_{pr} is the molecular mass of the precursor solution.

3.3.2 Model Validation

The surface tension of the precursor solution was calculated based on the volume fraction of the ethyl alcohol and butyl ether without considering the influence of other element concentrations (Chen, Tseng, Tsay and Lin, 2008). The surface tensions of ethyl alcohol and butyl ether are 22.32 and 17.06 dynes/cm, respectively. Therefore, the surface tension of the precursor solution was assumed to be 20.0 dynes/cm considering 1:1 volume mixing. The Eqns. (3) and (4) were used to calculate the average diameter of an aerosol droplet and deposited particle diameters. Parameters used in the calculation are summarized in Table 6. The calculated deposited particle size and experimentally measured values have a good agreement as shown in Figure 17. Figure 18 shows images of deposited particles at different precursor solution concentrations. Changing the concentration of precursor solution does not influence the aerosol droplet size, but the concentration of the precursor solution

determines the eventual particle size deposited. Capability to predict the deposited particle size will help to control and design the anode microstructure.

Table 6. Values used to calculate deposition particle diameter (d_p) by ultrasonic atomization

Precursor solution density (g ml^{-1})	0.88
Precursor solution surface tension (dynes cm^{-1})	20
Ultrasonic frequency (kHz)	60
Powder density ρ_p (mol l^{-1})	775
Powder molecular mass M_p (g mol^{-1})	348.85
Precursor solution molecular mass M_{pr} (g mol^{-1})	71
Calculated average droplet diameter d_d (μm)	100

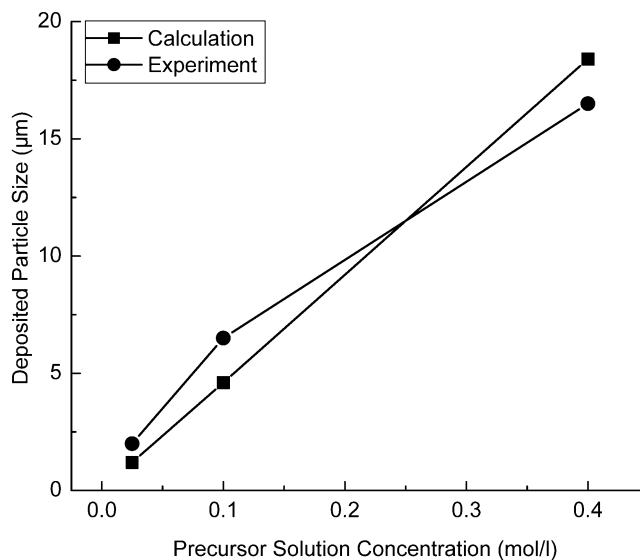


Figure 17. Comparison of Deposited Particle Size Calculated from Eqn. (4) and Measured from Experiments ($L = 1.23 \text{ ml min}^{-1}$, $Q = 1.5 \text{ l min}^{-1}$, $T = 300^\circ\text{C}$)

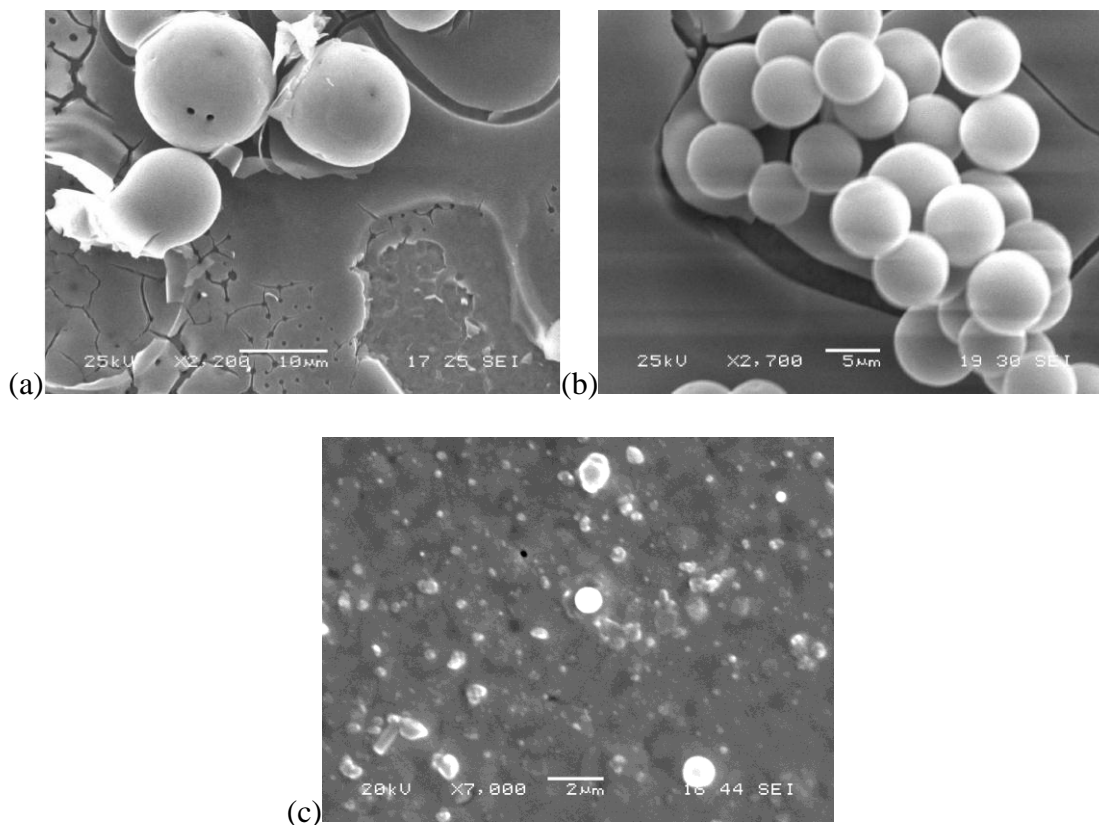


Figure 18. Images of Deposited Particles at Various Precursor Solution Concentrations

($L = 1.23 \text{ ml min}^{-1}$, $Q = 1.5 \text{ l min}^{-1}$, $T = 300^\circ\text{C}$). d_{pe} is the Diameter of Experiment Particle. (a) $C = 0.4 \text{ mol l}^{-1}$, $d_{pe} = 16 \text{ }\mu\text{m}$ (b) $C = 0.1 \text{ mol l}^{-1}$, $d_{pe} = 6 \text{ }\mu\text{m}$ and (c) $C = 0.025 \text{ mol l}^{-1}$, $d_{pe} = 2 \text{ }\mu\text{m}$

3.4 Results and Discussion

3.4.1 Analysis of the Deposited Anode Film Microstructure

In this section, the composition and microstructure evolution of the deposited anode film are analyzed. The compositional analysis of a typical anode film by EDS is summarized

in Table 7. The measured composition ratio of Ni/Ce/Gd was 15:8:1 as presented in Table 7. This is close to the theoretically calculated value of 15:9:1 based on the molar of ratio of Ni and CGO, which was 6:4. The weight ratio of NiO and CGO is about 50:50 without considering carbon, which comes from the decomposition of the precursor solution. In addition, the deposited anode film was analyzed by EDS mapping technique and to reveal the element distribution of Ni, Ce and Gd. As evident in Figure 19, the elements are homogenously distributed in the deposited film and within each particle. XRD analysis shows those deposition composites relevant diffraction patterns in Figure 20. The proposed method is capable of fabricating anode composite film with well-dispersed constitutive elements.

Table 7. EDS data showing element composition in the deposited anode film

Element	App Conc.	Intensity Corrn.	Weight%	Weight% Sigma	Atomic%
C	2.63	0.5533	4.75	0.41	14.38
O	31.82	1.2685	25.07	0.38	57.02
Ni	27.59	0.9434	29.22	0.37	18.11
Ce	33.39	0.9354	35.66	0.40	9.26
Gd	4.73	0.8923	5.30	0.33	1.23
Total			100.00		

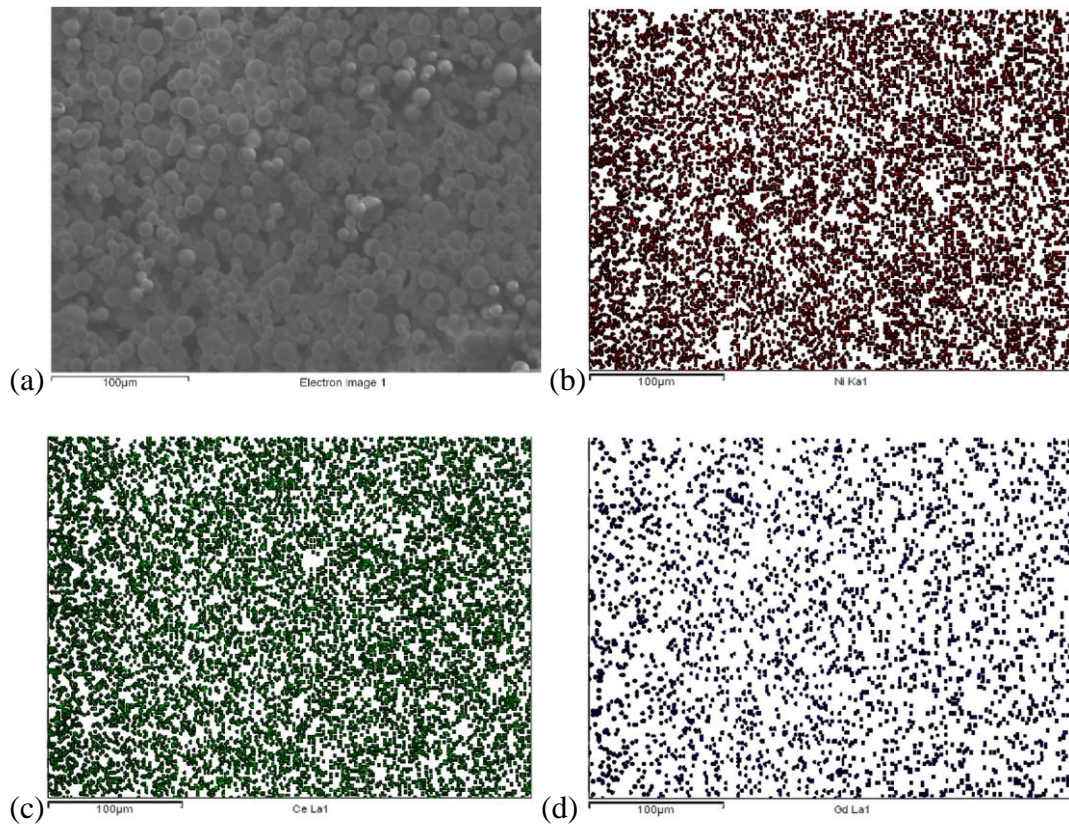


Figure 19. EDS Analysis of Corresponding Elements Distribution

(a) SEM image of the Analyzed Area (b) Ni (c) Ce (d) Gd

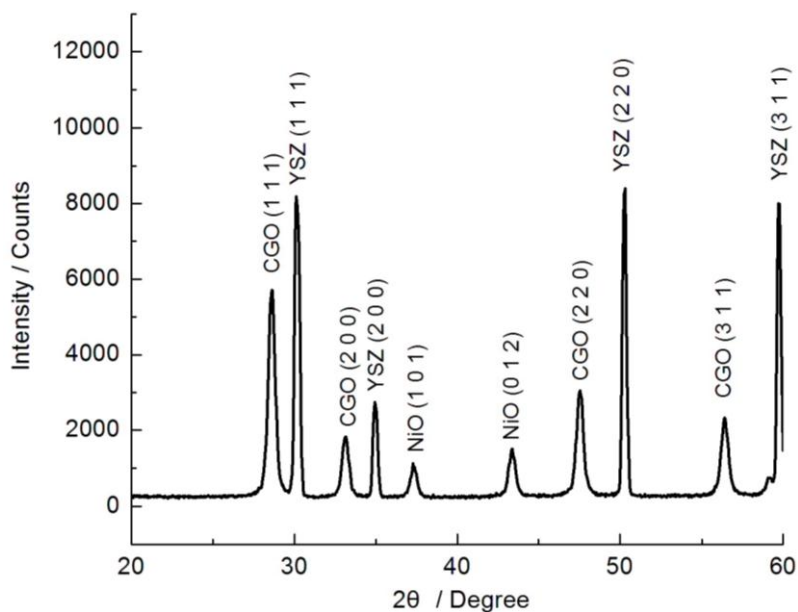


Figure 20. XRD Analysis of the Deposited Film

3.4.2 Effect of the Deposition Time

As the deposition time progresses, the deposited film morphologies evolve, shown in Figure 21. After 15 minutes, highly crystallized, dense deposition film was observed (see Figure 21 (a)). The porosity of the deposition film also increased, which agreed with prior work performed by T. Nguyen et al (Nguyen and Djurado, 2001). The initial dense deposition layer can be classified as type II morphology categorized by Schoonman et al (N.H.J. Stelzer, 1997). Rapid spreading of the precursor solution droplet may be the reason for the formation of a dense layer (Nguyen and Djurado, 2001). Once the deposition time passed 30 minutes, the deposited particles agglomerated and a columnar structure formed as shown in Figure 21 (c). Due to evolving microstructures during the deposition process, the deposition rate increased from $0.10 \mu\text{m min}^{-1}$ to $0.24 \mu\text{m min}^{-1}$ after 60 minutes of deposition

time (See Figure 22). When the deposition time reached 60 minutes, a porous top layer was formed on the dense bottom layer in accordance with the type III morphology (N.H.J. Stelzer, 1997).

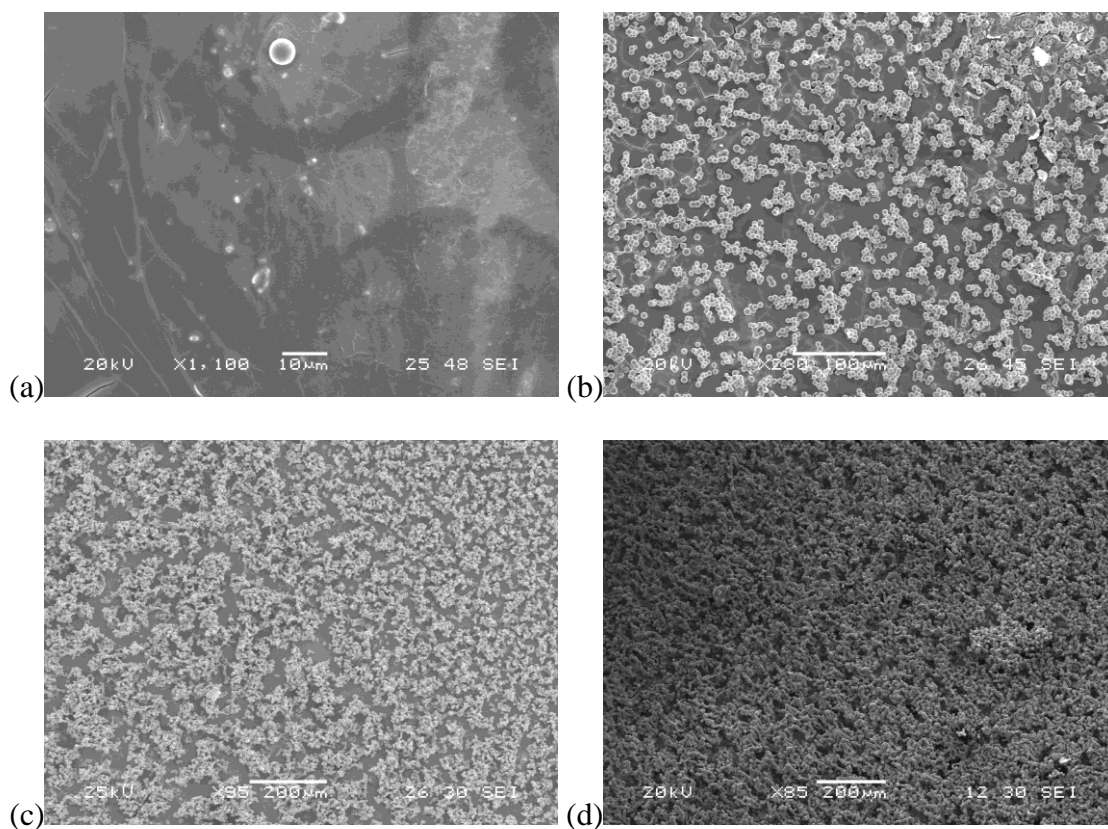


Figure 21. Deposited Substrate Morphology at Different Deposition Times ($L = 1.23 \text{ ml min}^{-1}$, $Q = 1.5 \text{ l min}^{-1}$, $C = 0.1 \text{ mol l}^{-1}$, $T = 300 \text{ }^\circ\text{C}$) (a) After 15 minutes (b) After 30 minutes (c) After 45 minutes (d) After 120 minutes

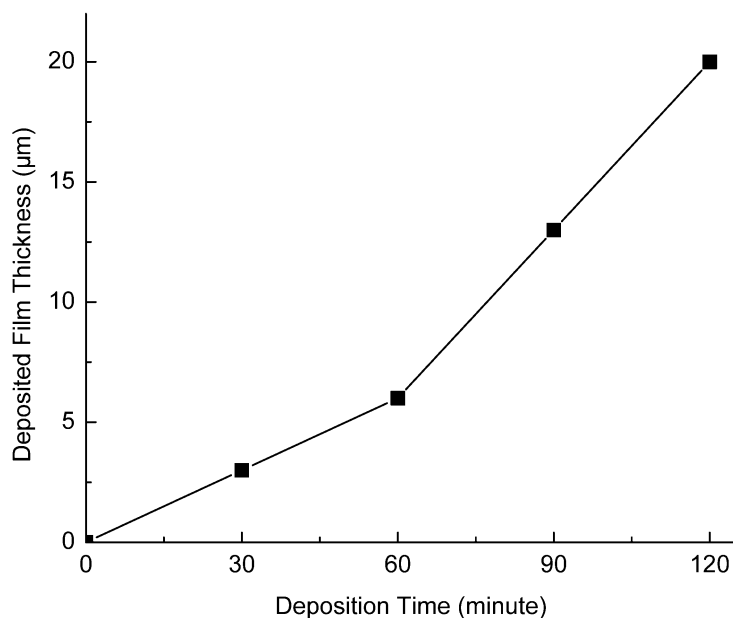


Figure 22. Increase of Anode Film Thickness with Deposition Time ($L = 1.23 \text{ ml min}^{-1}$, $Q = 1.5 \text{ l min}^{-1}$, $C = 0.1 \text{ mol l}^{-1}$, $T = 300 \text{ }^\circ\text{C}$)

3.4.3 Effect of Precursor Solution Concentration

Effects of precursor solution concentration on deposited particle size and porosity were analyzed. As shown in Figure 23, higher precursor solution concentration resulted in deposition of larger particles. The particle size increased from $2 \mu\text{m}$ to $20 \mu\text{m}$ when the precursor solution concentration increased from 0.025 mol l^{-1} to 0.4 mol l^{-1} . By lowering the precursor solution concentration, particle with sub-micrometer size can be deposited. As the solution concentration increased, higher porosity was obtained due to the formation of large particles with a high degree of agglomeration (see Figure 24). The porosity increased from 21% to 38% by changing the precursor solution concentration from 0.025 mol l^{-1} to 0.4 mol l^{-1} when the deposition temperature was $250 \text{ }^\circ\text{C}$. While the precursor concentration should not

exceed the solubility limit of the chemical compounds, it should not be too low to achieve a reasonable deposition rate. At low concentration, the particles will be blown away from the substrate by the carrier gas, and therefore, the deposition rate will be very low. The precipitated particle needs to be above a minimum size in order to overcome the thermophoresis force.

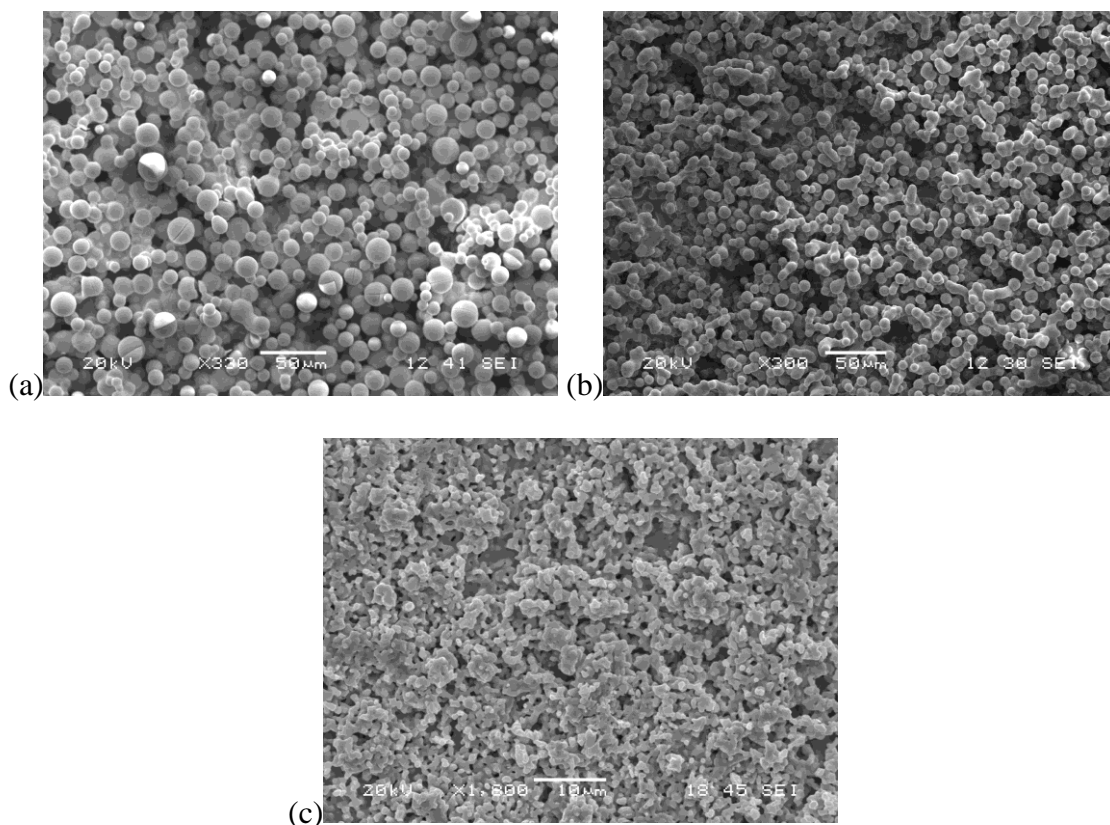


Figure 23. Images of Deposited Anode Film at Different Precursor Solution Concentrations ($L = 1.23 \text{ ml min}^{-1}$, $Q = 1.5 \text{ l min}^{-1}$, $T = 300^\circ \text{C}$) (a) $C = 0.4 \text{ mol l}^{-1}$ (b) $C = 0.1 \text{ mol l}^{-1}$ (c) $C = 0.025 \text{ mol l}^{-1}$

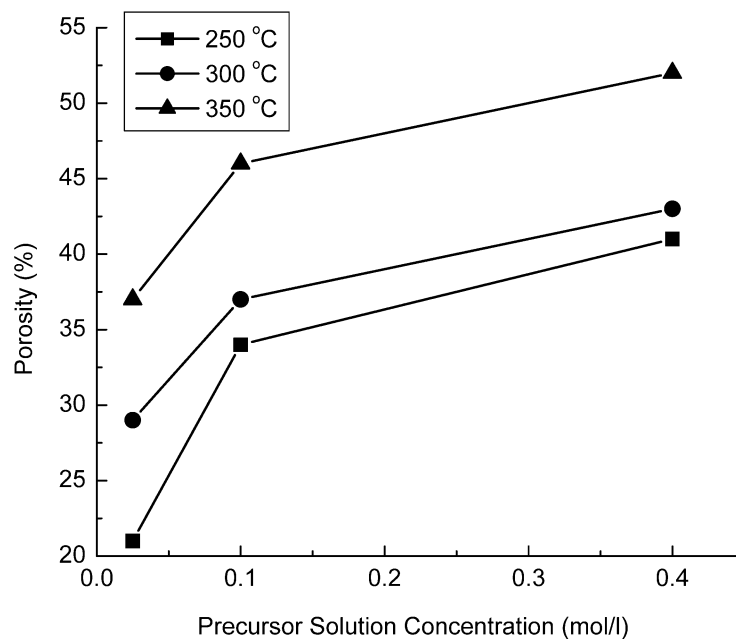


Figure 24. Effect of Temperature and Precursor Solution Concentration on Deposited Anode Film Porosity ($L = 1.23 \text{ ml min}^{-1}$, $Q = 1.5 \text{ l min}^{-1}$)

3.4.4 Effect of Deposition Temperature

The deposition temperature also significantly influenced the morphology and porosity of the microstructure. A relatively dense layer is formed in the beginning of deposition near the YSZ interface and is referred to as bottom layer. A porous film formed and accumulated on top of the bottom layer. As shown in Figure 25, the bottom layer (YSZ interface) and the top layer (the free surface) showed distinctly different structures at three temperatures. Fewer cracks were found at higher temperature in the bottom layer. The deposition temperature at least should be above the boiling temperature of the precursor solution, which will guarantee an effective evaporation of the solution during deposition of the atomized droplet. Low deposition temperatures below 250 °C is not appropriate for

anode film deposition because the droplets cannot be easily vaporized due to the high boiling temperature of diethylene glycol mono-n-butyl ether. Even at 250 °C, the excessive amount of precursor solution remains on the substrate for too long and results in surface cracks as shown in Figure 25 (a). Similar results were reported by Wilhelm et al (Wilhelm et al., 2005).

The higher deposition temperature resulted in higher porosity in the deposited film as shown in Figure 24. The large amount of vapor generated from the fast evaporating solvent during high deposition temperature is assumed to be responsible for the high porosity of the deposited film (Bohac and Gauckler, 1999). On the other hand, the diameter of atomized droplet decreased as it decomposed into smaller particles at higher deposition temperatures (see Figure 26). Some particle sizes are below micrometer (See Figure 25 (f)). However, temperatures above 450 °C should be avoided because the deposited film can break and result in numerous cracks and serious delamination due to the high thermal stress, as shown in Figure 27. Similar phenomena were reported by L. Gauckler et al (Bohac and Gauckler, 1999). Extremely high deposition temperature causes complete evaporation of the atomized droplet, and the precipitated particles are blown away before they can reach the substrate. Consequently, the deposition rate decreases significantly.

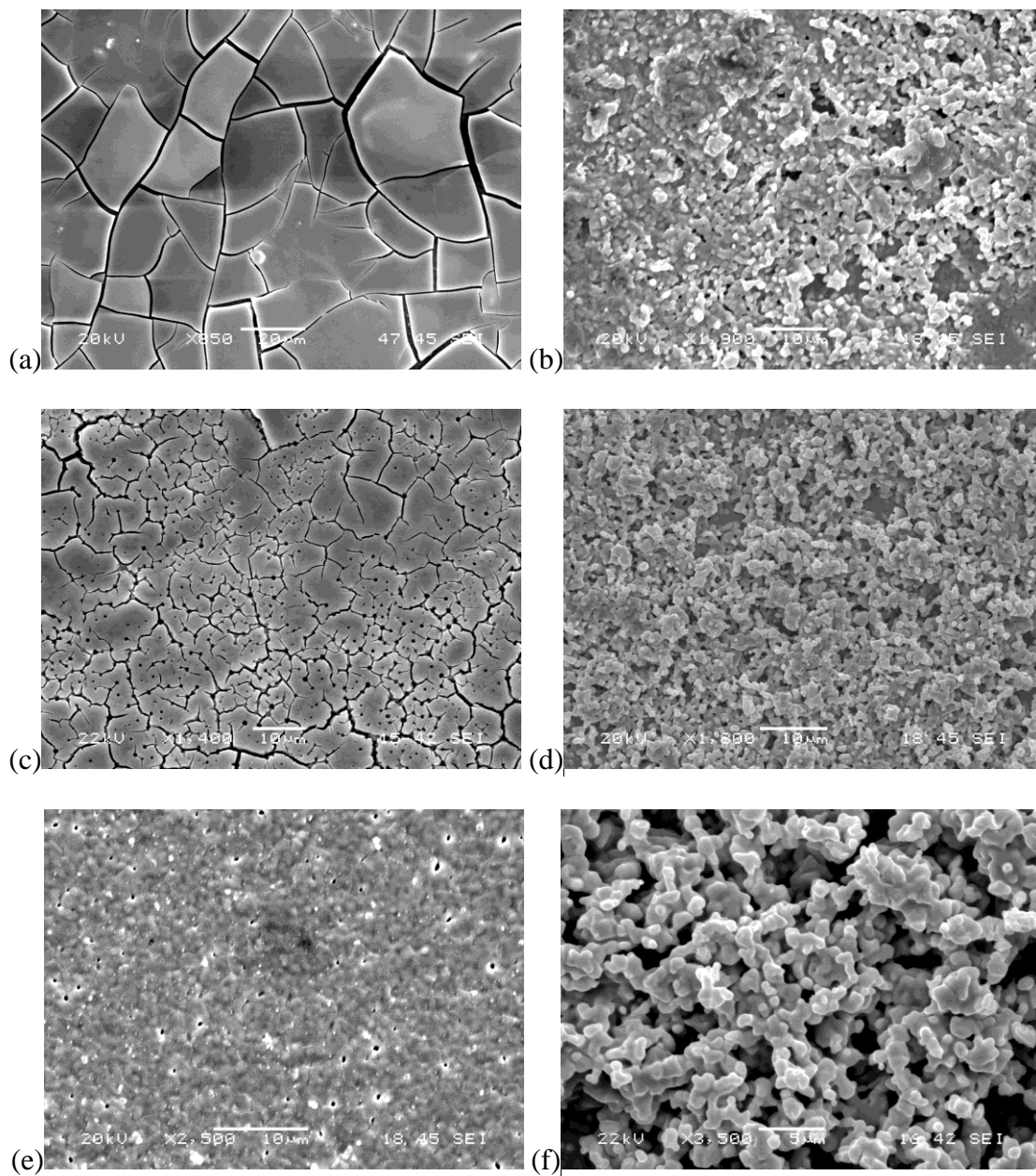


Figure 25. Images of deposited anode film at various deposition temperatures ($L = 1.23$ ml min⁻¹, $Q = 1.5$ l min⁻¹, $C = 0.025$ mol l⁻¹) (a) $T = 250$ °C Bottom layer (b) $T = 250$ °C Top layer (c) $T = 300$ °C Bottom layer (d) $T = 300$ °C Top layer (e) $T = 350$ °C Bottom layer (f) $T = 350$ °C Top layer

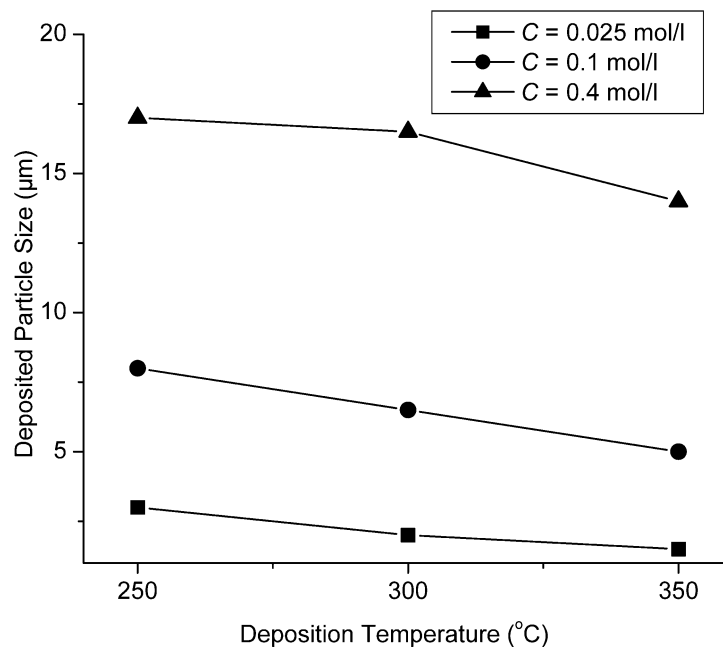


Figure 26. Effect of temperature and precursor solution concentration on deposited particle size ($L = 1.23 \text{ ml min}^{-1}$, $Q = 1.5 \text{ l min}^{-1}$)

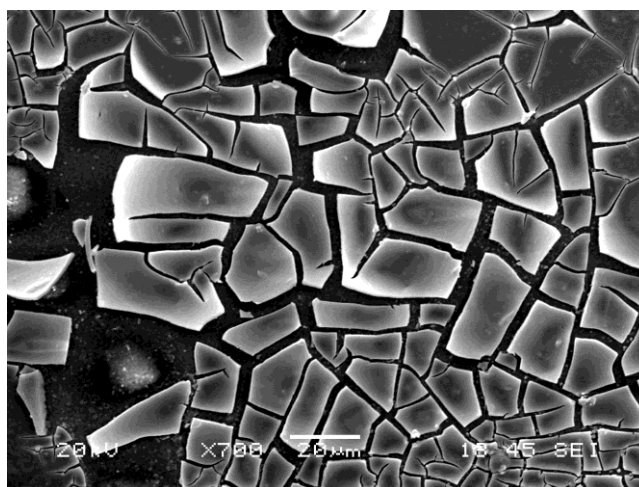


Figure 27. Severely cracked deposited anode film ($L = 1.23 \text{ ml min}^{-1}$, $Q = 1.5 \text{ l min}^{-1}$, $C = 0.1 \text{ mol l}^{-1}$, $T = 450 \text{ }^\circ\text{C}$)

3.4.5 Effect of Precursor Solution Feed Rate

Precursor solution feed rate did not influence the deposited anode film microstructure and morphology as significantly as the precursor solution concentration or the deposition temperature. The precursor solution feed rate determines the amount of atomized precursor solution reaching the substrate. At higher solution feed rate, larger amount of droplets reach the substrate. Increase of precursor solution on the substrate requires longer decomposition and drying time. This leads to denser layer and more severe cracks. The deposited bottom layer morphologies are shown in Figure 28. When the precursor solution feed rate increased from 1.23 ml min^{-1} to 1.7 ml min^{-1} , the porosity of the film and the diameter of the deposited particle remained relatively constant at 37% and $7.5 \mu\text{m}$, respectively. The precursor solution feed rate only had minimal influence on the deposited anode film microstructure and morphology.

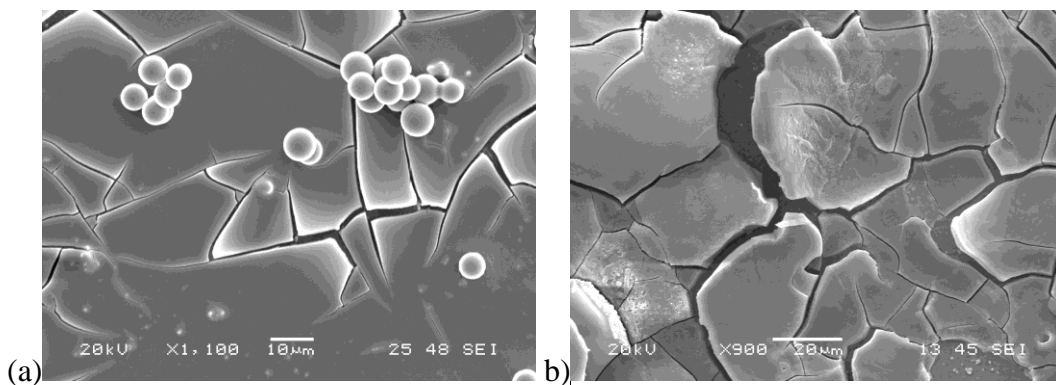


Figure 28. Images of deposited anode film at different precursor solution feed rate ($Q = 1.5 \text{ l min}^{-1}$, $C = 0.1 \text{ mol l}^{-1}$, $T = 250 \text{ }^\circ\text{C}$) (a) $L = 1.23 \text{ ml min}^{-1}$ (b) $L = 1.78 \text{ ml min}^{-1}$

3.5 Conclusions

The study demonstrated the potential of ultrasonic spray pyrolysis for tailoring the microstructure of Ni-CGO anode electrode of a SOFC. The effects of processing parameters, including deposition time, precursor solution concentration, deposition temperature and precursor solution feed rate, on the deposited anode film morphology and porosity were analyzed. Following conclusions may be drawn from this study:

(i) The ultrasonic spray pyrolysis demonstrated its capability to uniformly disperse the constitutive elements. The EDS and XRD analysis showed that all the elements, nickel, cerium, and gadolinium with corresponding diffraction patterns, were homogeneously distributed on the substrate. Thus, it verified the capability of the developed prototype fabrication setup in dispersing the constitutive elements.

(ii) The ultrasonic atomization model based on Jokanovic et al. (Jokanović, 1996; Jokanović et al., 2004) was capable of accurately predicting the size of deposited anode particle. The model can be a useful tool to design and deposit optimal microstructure.

(iii) The precursor solution concentration and deposition temperature were the most critical parameters that influenced the morphology and porosity of the deposited microstructure. The deposition temperature influenced the integrity of the deposited layer and deposition rate.

(iv) The study finds that by controlling these parameters, deposition particle size below 2 μm and porosity in the range of 22%–54% can be controlled by ultrasonic spray pyrolysis for Ni-CGO anode.

CHAPTER 4. MICROSTRUCTURAL AND ELECTROCHEMICAL IMPEDANCE STUDY OF NI-CGO ANODES FOR SOLID OXIDE FUEL CELLS

4.1 Introduction

Solid oxide fuel cells (SOFCs) are electrochemical energy conversion devices that directly convert a chemical fuel source into electrical power. Much attention has been focused on improving the performance of the SOFC electrodes (Jiang et al., 2005; Yoon et al., 2004; Ali et al., 2008; Uchida et al., 2000). One potential improvement is to increase the number of reaction sites on the electrodes. The electrochemical reactions are known to occur at triple phase boundary (TPB) sites, where the reactant gas phase comes into contact with the electronic conductor and ionic conductor (O'Hayre et al., 2005a). Increasing the extent of TPBs in the electrode thereby can be used to increase the reaction sites and produce better electrochemical performance. Also, a highly porous electrode is required to efficiently supply fuel gas to the TPB sites. Therefore, designing and controlling the microporosity of the electrode is critical in improving cell performance (Tanner et al., 1997; Deseure et al., 2005a; Greene et al., 2006).

Various techniques have been used to fabricate SOFC electrodes, including tape casting (Song et al., 2008), screen printing (Rotureau et al., 2005), spin coating (Xu et al., 2005a), tape calendaring (Minh, 2004), thermal plasma spraying (Hui et al., 2007), electrostatic spray deposition (Nguyen and Djurado, 2001) and spray pyrolysis (Chang et al.,

2008). These methods have been summarized and compared in our previous paper (Liu, Kim and Chandra, 2010a). Compared with other techniques, spray pyrolysis has the most potential capability to control the deposition microstructure because of the flexibility in processing parameters and their impact on film structure. Several types of spray pyrolysis methods have been investigated to fabricate electrodes in SOFCs, such as electrostatic spray pyrolysis (Xie et al., 2007; Wilhelm et al., 2005; Nguyen and Djurado, 2001; Princivalle et al., 2004), gas pressurized spray pyrolysis (Beckel et al., 2006; Muecke et al., 2009; Muecke, Akiba, Infortuna, Salkus, Stus and Gauckler, 2008) and ultrasonic spray pyrolysis (Hamedani et al., 2008; Moe et al., 1998; Chang et al., 2008; Chen and Hwang, 2008). However, none of the studies on ultrasonic spray pyrolysis investigated porosity of the deposited electrode, which can significantly influence the electrode performance (Zhao and Virkar, 2005). It is generally considered that the electrode performance highly depends on its microstructure. Despite a wealth of electrochemical analysis and data of (Ni/CGO) electrode on YSZ electrode, only a few studies experimentally have demonstrated the enhancement of electrochemical performance that can be achieved by manipulating electrode microstructure, such as changing the deposited particle size and electrode porosity (Chen and Hwang, 2008; Muecke et al., 2008). Also, it remains unclear how changing both the particle size and electrode porosity impacts electrode performance.

AC impedance is a more general type of resistance which involves multiple mass transfers, chemical and electrochemical processes (Huang, Hui, Wang and Zhang, 2007). Electrochemical Impedance Spectroscopy (EIS) has been widely used for SOFC component

performance evaluation and degradation diagnostics (Huang et al., 2007; Barbucci, Viviani, Carpanese, Vladikova and Stoynov, 2006; Koide, Someya, Yoshida and Maruyama, 2000). EIS allows direct observation of electrochemical cell properties and the ability to unambiguously separate the role of electrolyte resistance from electrode performance. In this study, ultrasonic spray pyrolysis was used to deposit anode electrodes with varying particle size and porosity. EIS was then employed to measure the electrode resistance of the deposited anodes at various temperatures to quantitatively deduce the role of electrode microstructure on electrochemical activity.

4.2 Experimental Procedures

4.2.1 Ultrasonic Spray Pyrolysis Deposition Experiment

The spray pyrolysis setup used in the electrode deposition is shown in Figure 29. Spray Pyrolysis Experiment Setup. The setup consists of a carrier gas delivery system, a syringe pump, an ultrasonic nebulizer and a hot plate. The detailed description of the setup , experiment material and precursor solution preparation procedure can be found in the earlier work (Liu et al., 2010a).

Two processing parameters were considered in this study: precursor solution concentration (C) and deposition temperature (T). Prior work showed that the precursor solution feed rate (L) had only a minor influence on the resulting film microstructure (Liu et al., 2010a), and therefore, it was fixed at 1.23 ml min^{-1} . The full experiment matrix is provided in Table 8. The deposited samples were all annealed at $800 \text{ }^\circ\text{C}$ for 2 hours to

promote crystallization of the deposited films at heat-up and cool-down rates of $5\text{ }^{\circ}\text{C min}^{-1}$ under N_2 atmosphere. The morphology and composition of the deposited anode film were examined by scanning electron microscope (JEOL JSM-606LV) and energy dispersive X-ray spectrometer (INCA mics/x-stream/SEM TVA3). SEM images were analyzed by software, ImageJ, to calculate the deposition particle size and deposition film porosity. Siemens D-500 X-ray diffraction system was used to obtain the X-ray diffraction (XRD) pattern of the deposited samples.

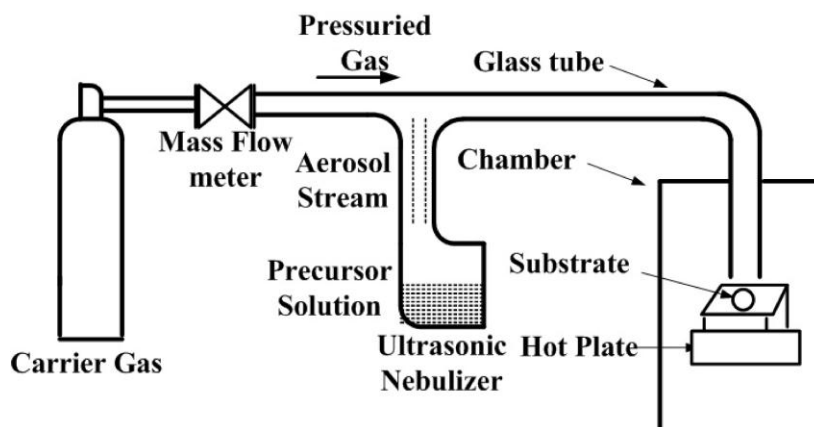


Figure 29. Spray Pyrolysis Experiment Setup

Table 8. Experimental matrix used in the study

#	Precursor solution concentration $C(\text{mol l}^{-1})$	Deposition Temperature $T (^{\circ}\text{C})$	Precursor solution feed rate $L (\text{ml min}^{-1})$
1	0.4	250	1.23
2	0.4	300	1.23
3	0.4	350	1.23
4	0.1	250	1.23
5	0.1	300	1.23
6	0.1	350	1.23
7	0.025	250	1.23
8	0.025	300	1.23
9	0.025	350	1.23

4.2.2 AC Electrochemical Impedance Spectroscopy (EIS) Experiment

Electrochemical impedance spectroscopy was carried out using a Ni/CGO-YSZ-Ni/CGO symmetrical cell (Figure 30). The test samples were prepared using the conditions summarized in Table 9. All samples were reduced under H_2 environment for 90 minutes to fully facilitate the reduction of NiO before impedance testing. All measurements were recorded by an electrochemical workstation (CHI760, CH Instruments, Austin, TX) over the frequency range of 0.1 Hz–100 KHz in a humidified H_2 environment. The temperature was varied between 663 $^{\circ}\text{C}$ and 763 $^{\circ}\text{C}$ to investigate the effect of working electrode temperature on the anode performance for the different electrode microstructures. The measurement voltage amplitude was fixed at 10 mV. Silver wire ($\varnothing 0.5\text{mm}$, 99%, Sigma Aldrich) and silver current collecting mesh (Ag-M40-100, FCM[®]) were pasted on the anode surface to serve as a current collector. The AC EIS experiment test stand is shown in Figure 31.

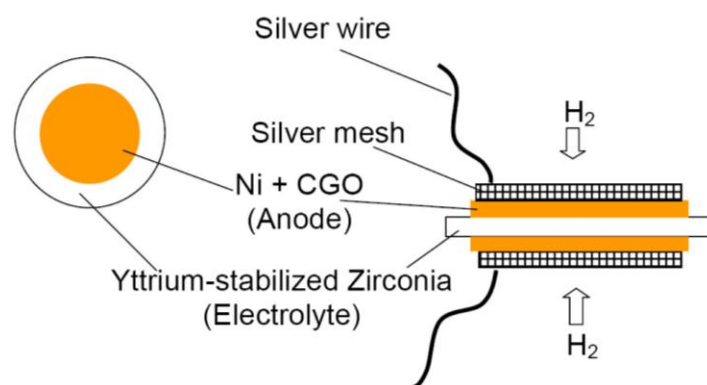


Figure 30. AC Impedance Test Sample Configuration

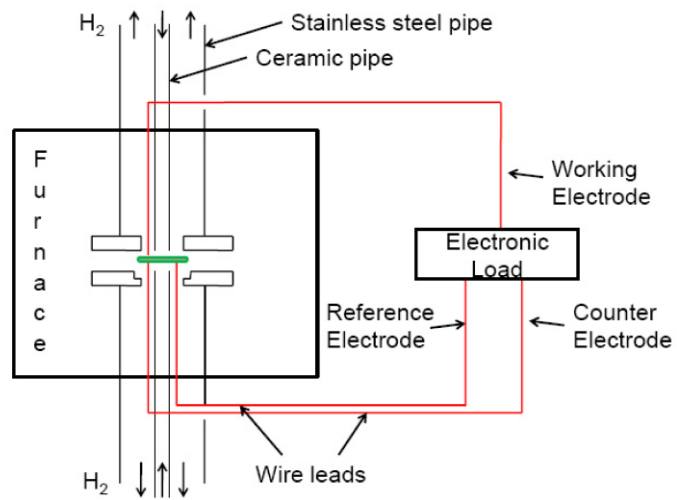


Figure 31. AC Impedance Test Setup

Table 9. Test sample preparation condition and sample microstructure information

#	Precursor solution Concentration C (mol l ⁻¹)	Deposition temperature T (°C)	Precursor solution feed rate L (ml min ⁻¹)	Average Deposition particle size d_p (μm)	Deposited film porosity p (%)
1	0.4	250	1.23	17	36
2	0.025	250	1.23	2.5	22
3	0.025	350	1.23	1.5	34

4.3 Results and Discussion

4.3.1 Ultrasonic Spray Pyrolysis Deposition Mechanism and Results of Anode Deposition Microstructure

The ultrasonic spray pyrolysis method used in this study possesses the characteristics of both conventional spray pyrolysis and chemical vapor deposition (CVD). The deposition mechanism is schematically illustrated in Figure 32. In conventional spray pyrolysis, the deposition occurs solely from high-velocity particles that strike the surface. In this approach, precursor aerosol is transported by a carrier gas, which enables deposition by evaporation-decomposition of precursor solution droplets. Therefore, the anode film is formed and thickened by the accumulation of droplets similar to that of aerosol assisted CVD (Perednis and Gauckler, 2005; Choy and Su, 2001; Hamedani et al., 2008). Compared to conventional spray pyrolysis, the proposed method can deposit a more uniform film with uniformly-sized particles. It also effectively solves the dilemma of spray mist waste in the deposition area that occurs in conventional spray pyrolysis, which then requires spraying over a much larger area than the designed electrode to deposit a uniform film.

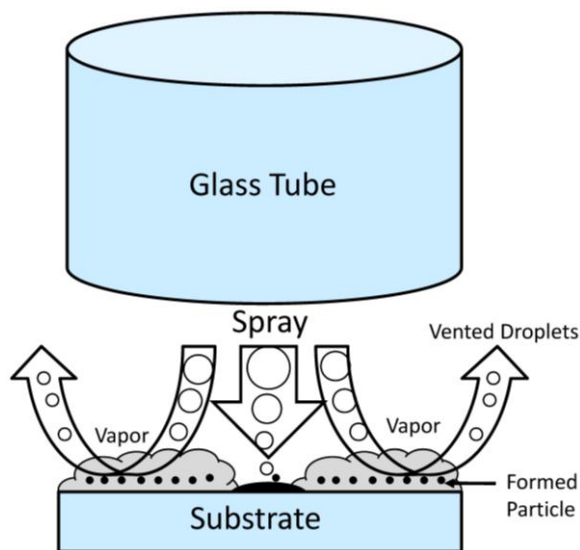


Figure 32. Schematic of Deposition Mechanism of Modified Spray Pyrolysis

A typical microstructure of the deposited anode film is shown in Figure 33. Composition EDS mapping and XRD analyses of the film are similar to those in section 3.4.1. The microstructures of the deposited anode were examined with SEM. Images of the microstructures obtained from the three different syndissertation conditions are shown in to Figure 34. A distinctly different electrode microstructure was observed for each. For Sample #1, perfectly spherical particles are observed, while larger necking between the particles was observed for Sample #2 and #3 due to sintering. Measured particle size and porosity are summarized in Table 9. The trend in particle size and porosity of the three samples is shown in Fig. 8 and Fig. 9, respectively. The particle size decreased from 17 μm in Sample #1 to 1.5–2.5 μm in Samples #2 and #3 by lowering the precursor solution concentration from 0.4 mol l^{-1} to 0.025 mol l^{-1} . Due to the effect of different deposition temperature of Sample #2 and #3, the particle size slightly decreased slightly from 2.5 μm to

1.5 μm (see Fig. 9), and the deposited anode porosity increased from 22% to 34%. Discussion of the changes of porosity and deposition particle size were described in earlier work (Liu et al., 2010a).

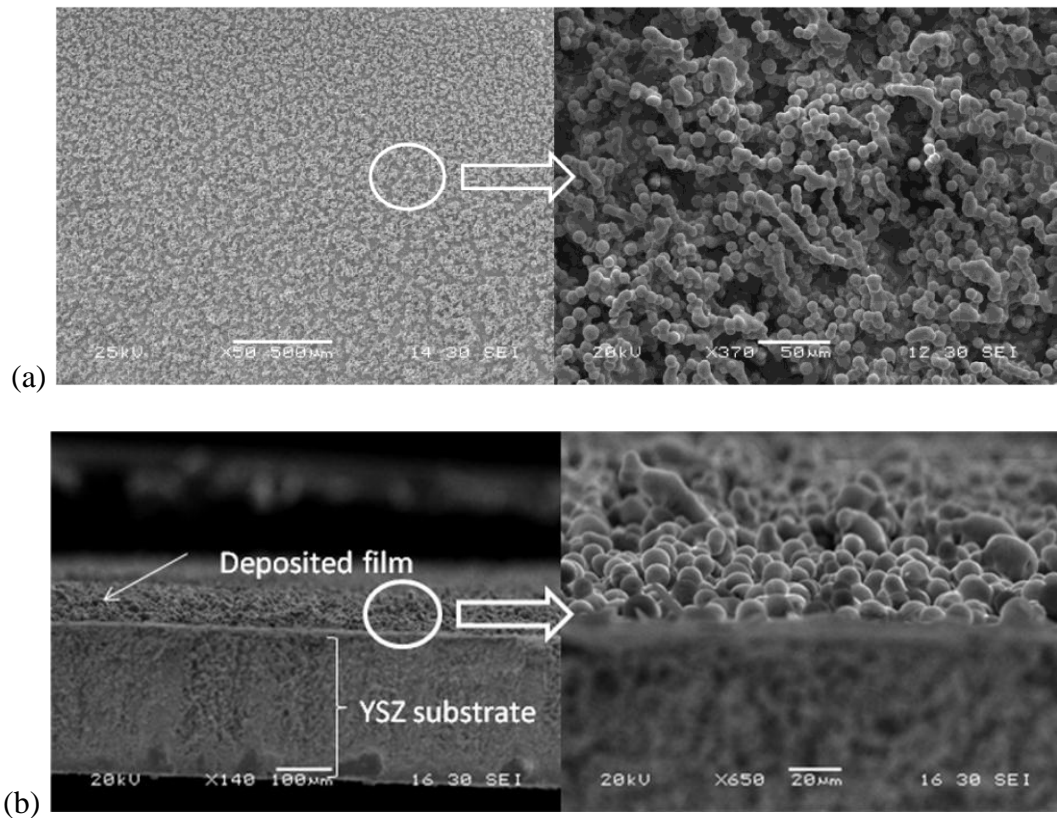


Figure 33. Microstructure of Deposited Anode Film ($L = 1.23 \text{ ml min}^{-1}$, $Q = 1.5 \text{ l min}^{-1}$, $C = 0.1 \text{ mol l}^{-1}$, $T = 300^\circ\text{C}$): (a) Top View and (b) Cross Section.

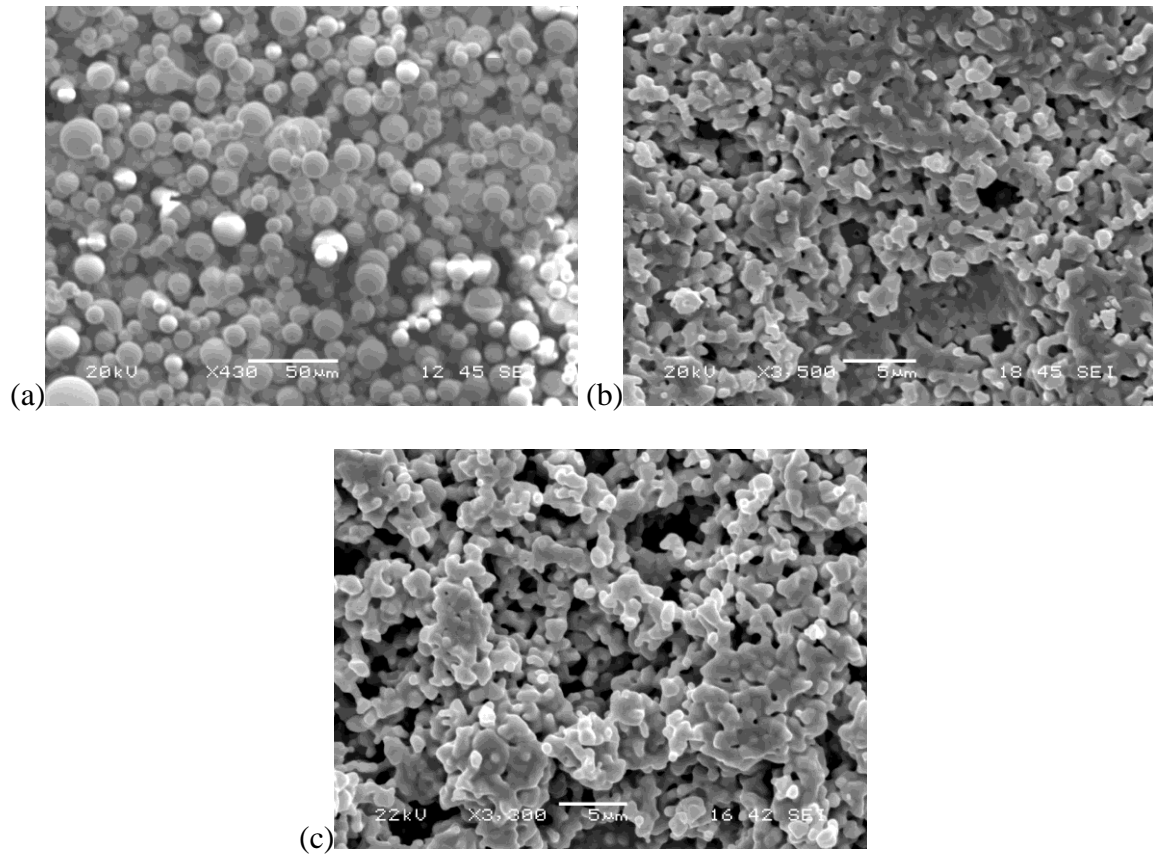


Figure 34. SEM Images of Anode Microstructures: (a) Sample #1 ($d_p = 17 \mu\text{m}$, $p = 36\%$), (b) Sample #2 ($d_p = 2.5 \mu\text{m}$, $p = 22\%$) and (c) Sample #3 ($d_p = 1.5 \mu\text{m}$, $p = 34\%$)

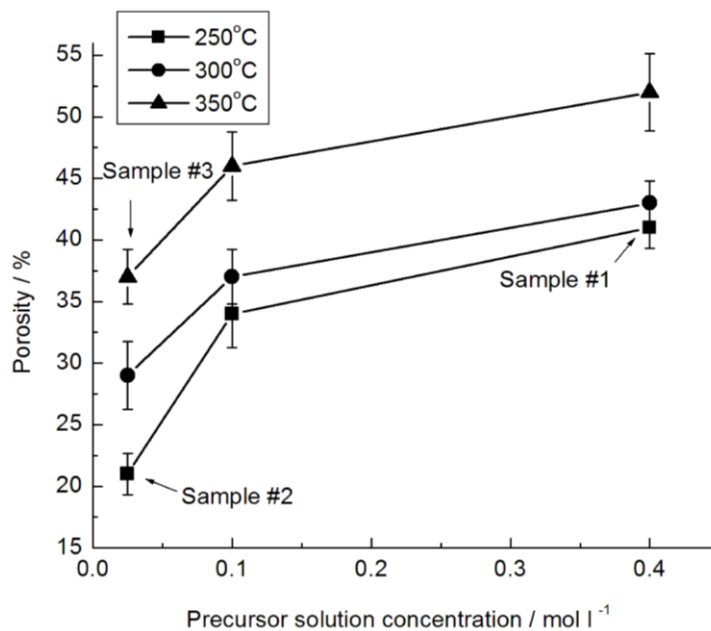


Figure 35. Plot of Film Porosity versus Temperature and Precursor Solution

Concentration ($L = 1.23 \text{ ml min}^{-1}$, $Q = 1.5 \text{ l min}^{-1}$).

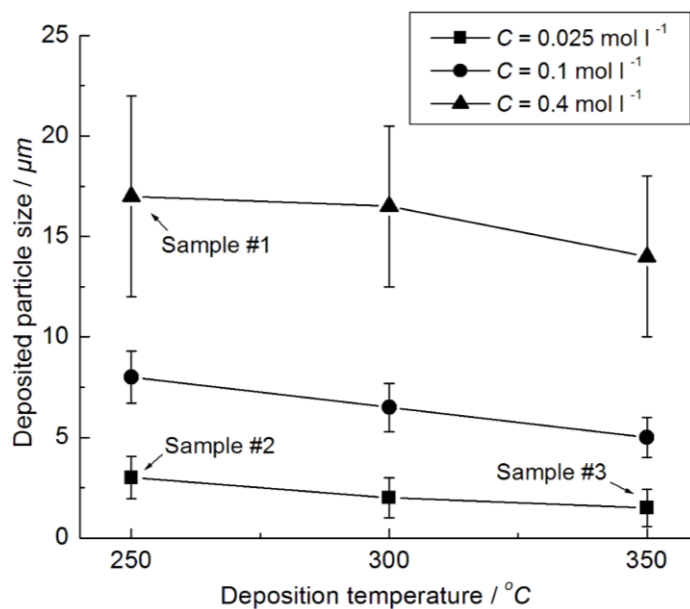


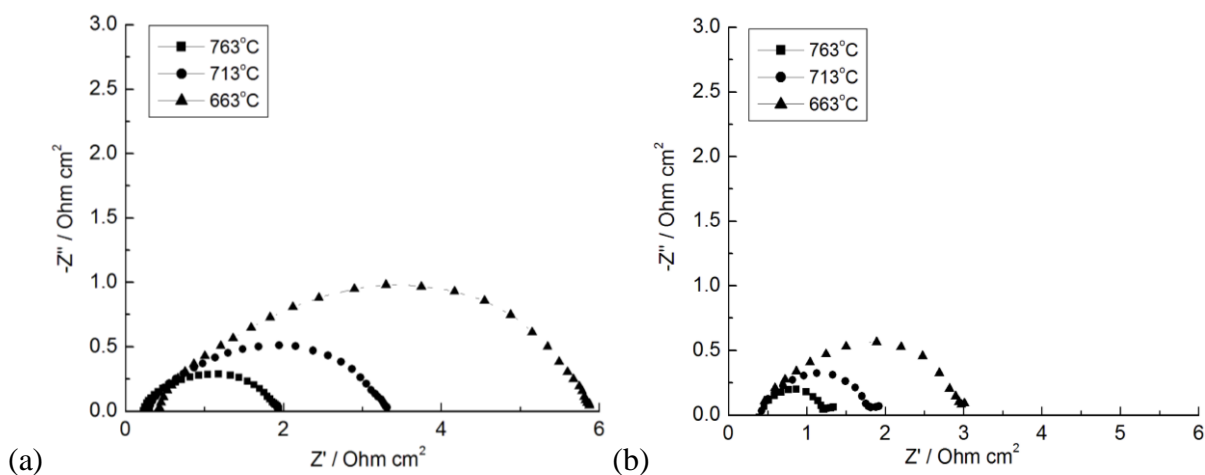
Figure 36. Plot of Particle Size versus Deposition Temperature

4.3.2 AC Electrochemical Impedance Spectroscopy Results of Different Anode Deposition Microstructures

The electrochemical performance of the different anode structures was evaluated using EIS. Nyquist plots for the three samples at three different test temperatures are shown in Figure 37. In each case, the impedance response can be interpreted in terms of a simple equivalent circuit (Figure 38) consisting of an electrolyte resistance ($R_{\text{electrolyte}}$) in series with an electrode element consisting of an electrode resistance ($R_{\text{electrode}}$) and double layer capacitance (C_{dl}) in parallel. In the Nyquist plot, Z' and Z'' represent the real and imaginary values of the cell resistance as a function of the frequency. The interception of the impedance with the real axis Z' in the low frequency regime corresponds to the total resistance, which includes the sum of the electrode and electrolyte resistances ($Z' = R_{\text{electrolyte}} + R_{\text{electrode}}$). The intercept of the impedance with the real axis at the high frequency range reflects just the electrolyte resistance ($R_{\text{electrolyte}}$). Thus, the resistance of the electrode ($R_{\text{electrode}}$), which can be interpreted as being proportional to the electrochemical reaction rate at the anode electrode, can be determined by subtracting the electrolyte resistance from the total cell resistance, which is also equal to the diameter of the impedance arc as measured at the intercept of the real axis.

The impedance results (Figure 37) show a clear decrease in the electrode resistance with increasing temperature, as well as a decrease in electrode resistance between Samples #1, #2 and #3. Microstructural measurements show that Sample #3 has an order of magnitude smaller particle size than Sample #1. Prior research has shown that this decrease

in particle size increases the TPBs and, thereby, improves the performance of deposited electrode (Li, Li and Guo, 2010). This improvement in electrode performance is clearly seen here, where the electrode resistance also decreased by nearly an order of magnitude from 5.45 ohm cm² for Sample #1 to 0.61 ohm cm² for Sample #3 at 663 °C. Notably, these resistance values are within the typical range reported in the literature (Muecke et al., 2008; Primdahl and Liu, 2002; Ishihara, Shibayama, Nishiguchi and Takita, 2000). Several factors may have contributed to the difference in the impedance values of Sample #2 (0.835 ohm cm²) and Sample #3 (0.61 ohm cm²). Slight differences in the particle size may be one factor. In addition, the decrease in the porosity for Sample #2 may have contributed to an increase in the electrode resistance over Sample #3. In the work performed by Chen *et al* (Chen and Hwang, 2008), impedance values were seen to increase with decreasing porosity of deposited electrode. Having a low porosity very likely leads to mass transfer limitation. However, mass transfer limitation is expected to be very small for porosities above 20% (Abbasi, Evans and Abramson, 1983).



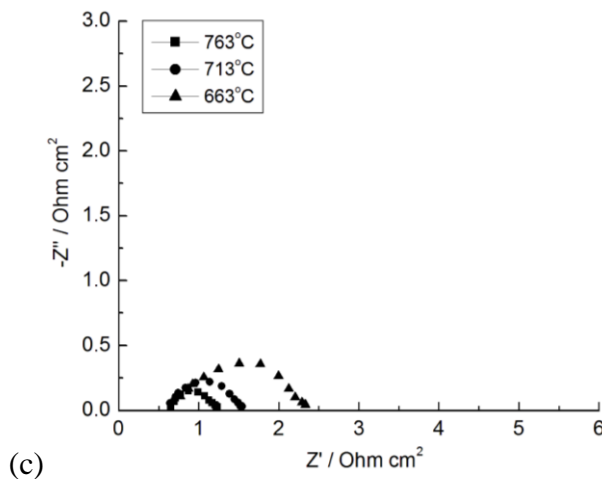


Figure 37. Nyquist Plots Depicting EIS Results for Various Samples at Three Test Temperatures: (a) Sample #1 ($d_p = 17 \mu\text{m}$, $p = 36\%$), (b) Sample #2 ($d_p = 2.5 \mu\text{m}$, $p = 22\%$) and (c) Sample #3 ($d_p = 1.5 \mu\text{m}$, $p = 34\%$)

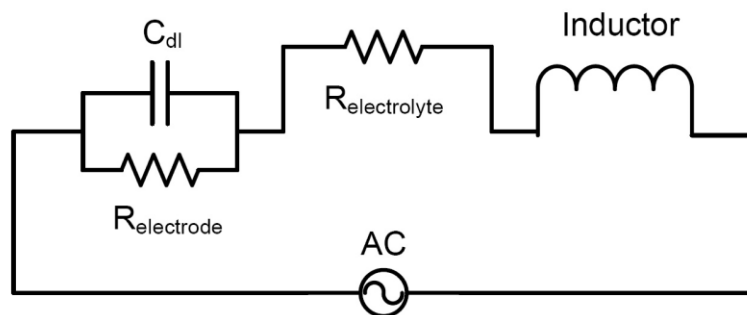


Figure 38. Equivalent Circuit of Electrochemical Test Cell

The temperature dependent electrode resistances that were measured could be used to determine the activation energy (E_a) of the different electrodes. Notably, polarization resistance is closely associated with the amount of TPB, where the reactant gas (H_2) comes into contact with an electronic conductor (Ni) and an ionic conductor (CGO) providing

continuing path for electrons and oxide ions. The activation energies (Ea) as determined from the impedance test are provided in the Arrhenius plot in Fig. 12 for the three different electrode samples. A decrease in the activation energy is observed when comparing Sample #1, #2 and #3.

The relationship between the volume-specific TPB length and the particle size and porosity can be approximated by the following equation (Deng and Petric, 2005):

$$L_{TPB} \propto N_{2pb} (\pi \alpha d_p) A_p = \frac{72\alpha [d_{pore} - (d_{pore} + d_p) p] p}{d_p^2 d_{pore}^2 (1 - \sqrt{1 - \alpha^2})} \quad (35)$$

where, N_{2pb} is the number of two-solid-phase-boundary per unit volume; α is the ratio of two-particle-contact-area diameter and particle diameter; A_p is the surface area of the pore phase per unit volume; d_p is the average diameter of deposition particle; d_{pore} is the average diameter of a pore. The values of α and d_{pore} were approximated from the SEM images. The calculated L_{TPB} for Sample #1 through #3 were $0.33 \mu\text{m} \mu\text{m}^{-3}$ ($\alpha = 0.9$, $d_p = 17 \mu\text{m}$, $d_{pore} = 9.6 \mu\text{m}$, $p = 36\%$), $2.7 \mu\text{m} \mu\text{m}^{-3}$ ($\alpha = 0.6$, $d_p = 2.5 \mu\text{m}$, $d_{pore} = 1.0 \mu\text{m}$, $p = 22\%$), and $3.6 \mu\text{m} \mu\text{m}^{-3}$ ($\alpha = 0.8$, $d_p = 1.5 \mu\text{m}$, $d_{pore} = 2.0 \mu\text{m}$, $p = 34\%$), respectively. Highest L_{TPB} were found in Sample #3, which contained the smallest particle size and largest porosity. As expected, microstructures with higher the L_{TPB} resulted in lower the area specific resistance (ARS). The activation energy was highest (Ea = 1.06 eV) in Sample #1 with largest particle size, and lower for smaller particle size electrodes (Ea = 0.90 and 0.86 eV). The values agree well with those reported in the literatures (Muecke et al., 2008; Primdahl and Liu, 2002). For the porosity ranges produced by spray pyrolysis in this study (above 20%), particle size has a

significant influence on the electrochemical performance of the electrode. However, if the particle size decreases to nanoscale, the effect of porosity may become a critical factor.

It can be observed that microstructures deposited by various processing conditions of spray pyrolysis result in different electrochemical performance. An effectively manipulated electrode microstructure can minimize activation and concentration polarizations (Virkar, Chen, Tanner and Kim, 2000). Optimization of the electrode microstructure in a SOFC may be an important approach to cost reduction and reliability enhancement (Huang et al., 2007).

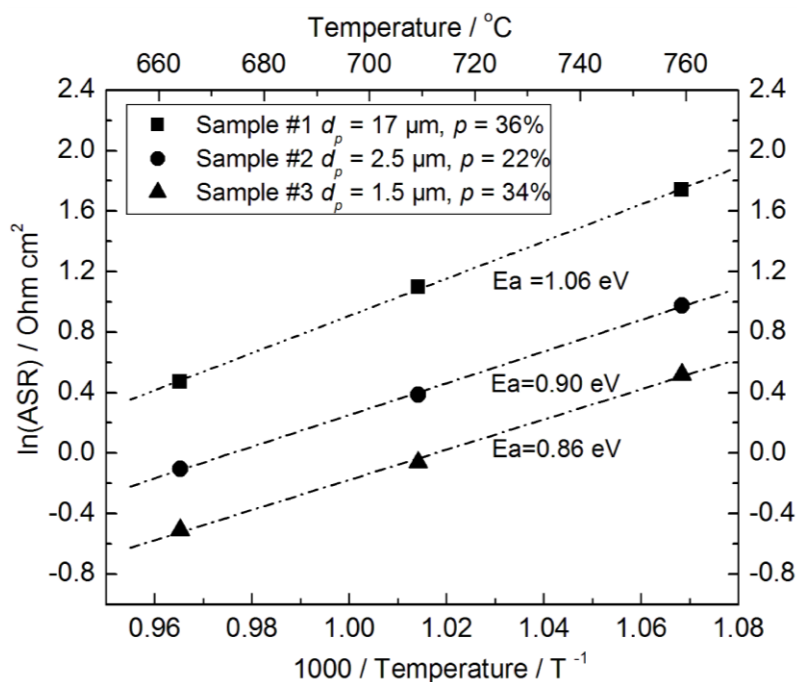


Figure 39. Arrhenius Plot of Electrode Resistances for Three Test Samples

4.4 Conclusions

In this study, a detailed experimental study was performed to demonstrate the potential of tailoring the electrode microstructure of a cell to improve the electrochemical

performance of the SOFC using ultrasonic spray pyrolysis. EDS and XRD analysis showed that all the elements of nickel, cerium and gadolinium, with corresponding diffraction patterns, were homogeneously distributed on the substrate. This demonstrates the capability of ultrasonic spray pyrolysis to create highly dispersed films. The precursor solution concentration (0.025–0.4 mol l⁻¹) and deposition temperature (250 °C–350 °C) significantly influenced the deposited anode microstructure and resulted in changes of electrochemical performance. By manipulating these process parameters, the deposited particle size and porosity could be controlled in the range of 1.5–17 μm and 21%–52%, respectively. The estimated volume-specific TPB length increased by one order of magnitude from 0.33 μm μm⁻³ to 3.57 μm μm⁻³ as a result of the decrease of the particle size and increase in porosity. Consistent with the estimated TPB length, the ASR of the anodes improved from 5.45 ohm cm² to 0.61 ohm cm², and the activation energy decreased from 1.06 eV to 0.86 eV for the temperature range of 663 °C to 763 °C. Ultimately, the influence of porosity on the electrode performance could not be independently isolated since the porosity of these films was above 20%, which is higher than typical mass transfer limited conditions.

**CHAPTER 5. MODELING OF SOLID OXIDE FUEL CELLS PERFORMANCE
WITH HOMOGENOUS AND GRADED ANODE IN PARTICLE SIZE AND
POROSITY**

5.1 Nomenclature

Symbols

Latin letters

A	Triple phase boundaries reaction area, $\text{m}^2 \text{m}^{-3}$
b	Shape factor, unitless
d	diameter, m
D	Diffusion coefficient, $\text{mol m}^{-2} \text{s}^{-1}$
F	Faraday's constant, C mol^{-1}
g	Gibbs free energy, J mol^{-1}
i_n	Charge transfer current density, A m^{-2}
i_o	Exchange current density, A m^{-2}
I	Total current, A m^{-2}
J	Molar flux, $\text{mol m}^{-2} \text{s}^{-1}$
l	Thickness of electrode, m
M	Molecular weight, g mol^{-1}
n_e	Number of electrons in reaction
n^*	Number of particle per volume
n_{el}	Number fraction of electronic particles, unitless
n_{io}	Number fraction of ionic particles, unitless
p	Pressure, Pa

pr	Probability of being in a percolation cluster, unitless
r	Radius of particle, m
R_{ct}	Charge transfer resistance $\Omega \text{ cm}^2$
R_g	Gas constant, $\text{J mol}^{-1} \text{ K}^{-1}$
R_p	Particle size ratio, unitless
T	Temperature, K
V	Voltage, V
Z	Coordination number, unitless

Greek letters

β	Symmetry factor, unitless
γ	Necking factor, unitless
ε	Porosity, unitless
θ	Contact angle, radians
ρ	Resistivity, ohm m
σ	Collision diameter, \AA
τ	Tortuosity, unitless
φ	Volume fraction, unitless
Ω	Collision integral

Super script

i	Inlet
-----	-------

Sub scripts

a	Anode
A	Gas specie A
act	Activation
B	Gas specie B
c	Cathode
$conc$	Concentration

<i>ct</i>	Charge transfer
<i>cr</i>	Critical
<i>eff</i>	Effective
<i>el</i>	Electronic
<i>eq</i>	Equilibrium
<i>f</i>	Free surface
H_2O	Water
H_2	Hydrogen
<i>i</i>	Interface at electrolyte
<i>io</i>	Ionic
<i>K</i>	Knudsen diffusion
<i>loss</i>	Loss
O_2	Oxygen
<i>ohm</i>	Ohmic
<i>p</i>	Particle
<i>pore</i>	Pore
<i>r</i>	Reaction site

5.2 Introduction

Solid Oxide Fuel Cells (SOFCs) have demonstrated the potential to meet the critical energy needs of our modern civilization and are a possible partial solution to maximizing dwindling fossil fuel resources. SOFCs possess the merits of high efficiency (EG&G Technical Services Inc., 2004a; Litzelman, Hertz, Jung and Tuller, 2008; Zhao, Shah and Brandon, 2010), being fuel flexible and tolerant of impurities such as sulfur (Li, 2006; Williams, 2007; Li and Thangadurai, 2009). However, commercialization of SOFC has been hindered by its high voltage loss and high operating temperature. Anode-supported cells

have been developed and investigated to decrease the operating temperature of a SOFC with enhancing their electrochemical performance. Currently, a lot of focus has been put on SOFCs cost, efficiency, and cell life (Surdoval, 2006; Shaffer, 2006; Ni, Leung and Leung, 2007a; Grew, Joshi and Chiu, 2010; Liu, Kim and Chandra, 2010b); little attention has been given to optimizing electrochemical performance by minimizing voltage loss. SOFC electrode electrochemical behavior is mainly determined by three major losses: activation loss, Ohmic loss, and concentration loss. These values are significantly influenced by the microstructure of the electrode (Chan and Xia, 2001). Reaction and concentration losses depend on the quantity and location of triple phase boundaries (TPBs), where a reactant gas molecule, an electronic conductor, and an ionic conductor join to convert fuel's chemical energy to electrical energy occurring in the SOFC anode (O'Hayre, Barnett and Prinz, 2005b) (See Figure 40(a)). Therefore, SOFCs performance can be improved by modifying the electrode microstructure for TPB quantity and location within the anode. One novel way of tailoring electrode microstructures is by functionally grading the electrode, i.e., varying the composition or structure gradually from the electrolyte/electrode interface to the electrode free surface. Through mathematical modeling and experimental efforts, functionally graded structures have been shown to improve power output (Jono, Suda and Hattori, 2007b; Meng, Sun, He and Li, 2008; Xu, Xia, Xiao and Peng, 2005b; Hart, Brandon, Day and Lapena-Rey, 2002; Ni, Leung and Leung, 2007c; Holtappels and Bagger, 2002; Ni, Leung and Leung, 2007b; Holtappels, Sorof, Verbraeken, Rambert and Vogt, 2006).

Previous investigations have explored functionally graded electrodes and have given

explanations as to why it can be beneficial; such as, qualitatively stating that the TPB reaction area is higher in small particle size structures (Ni et al., 2007c). Ni et al (Ni et al., 2007c) presented a model exploring linearly graded electrodes, but did without optimization. Holtappels P. et al (Holtappels et al., 2006) showed porosity graded SOFC anode which optimized the gas transport through the substrate by maintaining a high electrochemical activity for fuel oxidation at the anode/solid electrolyte interface. They did not carry out performance and optimization analysis with porosity graded SOFCs. Thus far, state-of-the-art models have presented linear particle size grading (Ni et al., 2007c), porosity grading (Ni et al., 2007c; Holtappels et al., 2006), porosity-tortuosity ratio grading (Greene et al., 2006), and compositional grading (Deseure, Dessemond, Bultel and Siebert, 2005b; Schneider, Martin, Bultel, Dessemond and Bouvard, 2007). However, there is not any attempt to show electrode behavior based on grading ranges and grading profiles, other than linear. Therefore, the concept of nonlinearly graded structures, which is likely to occur in an actual fabrication process, in a SOFC electrode was explored for the first time in this work. The present study investigates the effect of particle size and porosity grading ranges and their relationship with the grading profiles within those ranges, including linear and nonlinear.

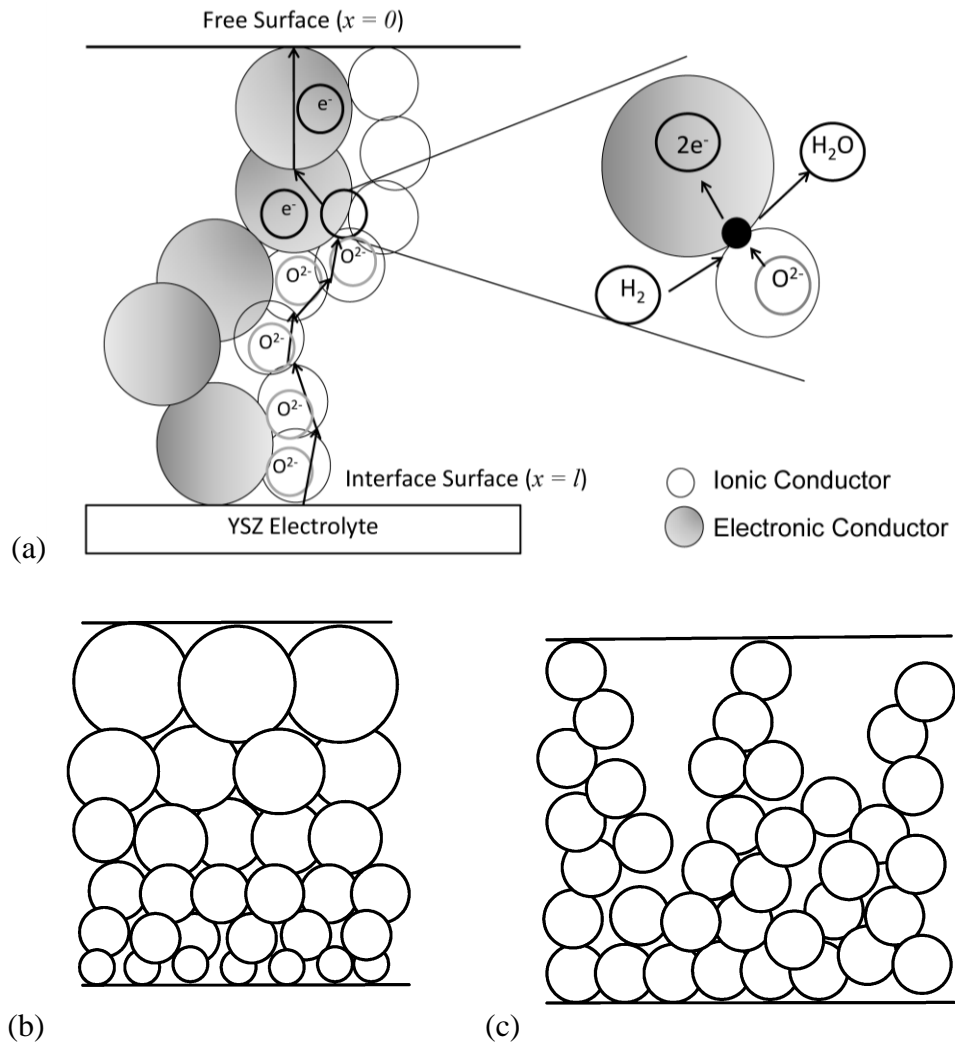


Figure 40. A schematic of TPB and microstructure grading: (a) reaction at TPB, (b) particle size grading, and (c) porosity grading

5.3 Model Development

The previously developed grading models account for the activation losses with the Butler-Volmer rate equation, conduction losses with Ohm's law, and concentration losses with combining a bulk gas diffusion theory with Knudsen diffusion. Greene et al (Greene et

al., 2006) investigated mass transfer losses in porosity graded SOFC electrodes using the mean transport pore model. One shortfall of the model was the parameter ψ , which was the porosity to tortuosity ratio. This does not allow for explicit input control of real porosity and tortuosity values. In addition, the activation losses were assumed to only occur at the electrode-electrolyte interface; however, this is generally not accepted to be true for a composite electrode (Ni et al., 2007c). Deseure et al (Deseure et al., 2005b) and Schneider et al (Schneider et al., 2007) have modeled conduction percolation through compositionally graded structures. Both pieces of work conclude that compositional grading has little benefit for increasing performance. Deseure et al's model (Deseure et al., 2005b), however, did not account for varying reactant gas pressure through the electrode, which ignores the effect of concentration losses. Ni et al's model (Ni et al., 2007c) was complete and varied the electrode microstructure continuously and linearly, but this leaves many more graded structures to be explored. Optimization of grading ranges was not explored at length. Besides those abovementioned, they also treated the anode and cathode with the same particle sizes and grading ranges. This does not account for the different requirements for each particular electrode based on electrode thickness and self-diffusion of the cathode verses counter-diffusion of the anode.

In this work, a system behavior of particle size and porosity graded SOFC electrode is studied by considering electrode behavior based on grading range and grading profile. This work expands upon previously developed theories and models (Chan and Xia, 2001; Costamagna, Costa and Antonucci, 1998). The model consists of a macro and a micro model.

The macro model describes the overall cell behavior through activation, Ohmic, and concentration losses based on chemical and concentration potentials. The micro model outputs effective resistivity of the porous electrode based on microstructural parameters such as pore diameter, particle size, and reaction area. The integration of macro and micro models is achieved by passing the micro model parameters to the macro model during the solution procedure.

In the macro model, the open circuit voltage (OCV), activation loss, Ohmic loss, and concentration (diffusion) losses are calculated. The operating cell voltage relationship can be expressed as:

$$V_{out} = V_{oc} - V_{loss} = V_{oc} - V_{ohm} - V_{act} - V_{conc} \quad (1)$$

where V_{out} is the output voltage; V_{oc} is the open circuit voltage; and V_{loss} is the total voltage loss. V_{loss} includes Ohmic loss voltage (V_{ohm}), activation loss voltage (V_{act}), and concentration loss voltage (V_{conc}).

The basic equations that are used in macro modeling are shared among many research papers (Colpan, Dincer and Hamdullahpur, 2008; Aguiar, Adjiman and Brandon, 2004; Greene et al., 2006). The Nernst potential is used to calculate the open-circuit voltage of SOFCs:

$$V_{oc} = \frac{-\Delta g}{n_e F} + \frac{R_g T}{n_e F} \ln\left(\frac{p_{H_2} \sqrt{p_{O_2}}}{p_{H_2O}}\right) \quad (2)$$

where g is the Gibbs free energy; n_e is the number of electron in reaction; F is the Faraday's constant; R_g is the gas constant; T is the temperature; and p_A is the gas pressure of specie A .

In an electrochemical system, polarization is defined by the following equation (Chan

and Xia, 2001; Costamagna et al., 1998; Ni et al., 2007c):

$$V_{loss} = (V_{el(eq)} - V_{io(eq)}) - (V_{el} - V_{io}) \quad (3)$$

where $V_{el(eq)}$ is the electronic equilibrium voltage; $V_{io(eq)}$ is the ionic equilibrium voltage; V_{el} is electronic voltage; and V_{io} is the ionic voltage.

The charge transport in an SOFC anode can be modeled based on the Ohm's law and the charge balance between the electronic and ionic conductors. The Ohm's law for electronic and ionic conductors are:

$$\frac{dV_{el}}{dx} = \rho_{el(eff)} i_{el} \quad \text{and} \quad \frac{dV_{io}}{dx} = \rho_{io(eff)} i_{io} \quad (4)$$

where $\rho_{el(eff)}$ is effective electronic resistivity; i_{el} is the electronic current density; $\rho_{io(eff)}$ is effective ionic resistivity; and i_{io} is the ionic current density. The charge balance in the electronic and ionic conductors is represented as:

$$\frac{di_{el}}{dx} = -\frac{di_{io}}{dx} = -Ai_n \quad (5)$$

where i_n is the exchange current density; and A is the TPB given in the unit of area per

volume. The Ohmic loss occurs due to the voltage gradient driving the charge transport and results in change of V_{loss} . Therefore, by combining Eqs. (3), (4), (5), the second derivative of Eq. (3) can be written as:

$$\frac{d^2V_{loss}}{dx^2} = \rho_{io(eff)} \frac{di_{io}}{dx} - \rho_{el(eff)} \frac{di_{el}}{dx} = (\rho_{el(eff)} + \rho_{io(eff)}) Ai_n \quad (6)$$

Eq. (7) shows the Butler-Volmer equation which is commonly used to describe the activation polarization that occurs in a cell. The activation loss is caused by the potential needed for charge transfer and is dependent on reactant concentration, material, temperature, and surface properties. Butler-Volmer equation is a rate determining equation, which

depends on the reaction mechanism. However, the exact reaction mechanism is difficult to identify because the formation of water may involve several intermediate steps. Other SOFC modeling work (Yoon, Zink, Gopalan and Pal, 2007; Zhu and Kee, 2003) verified the number of electron (n_e) transferred in the Butler-Volmer equation was one by comparing with experiments. The polarization model indicated that it was a one-electron transfer reaction mechanisms. Therefore, the reaction mechanism was simplified to assume each reaction occurrence is a one-step, single-electron transfer process (Noren and Hoffman, 2005).

$$i_n = i_o \left\{ \exp\left(\frac{\beta n_e F V_{act}}{R_g T}\right) - \exp\left(- (1 - \beta) \frac{n_e F V_{act}}{R_g T}\right) \right\} \quad (7)$$

where i_n is the charge transfer current density; i_o is the exchange current density; and β is the transfer coefficient (typically 0.5). Therefore, activation loss can be expressed as Eq. (8).

$$V_{act} = 2 \frac{R_g T}{n_e F} \sinh^{-1}\left(\frac{i_n}{2i_o}\right) \quad (8)$$

The concentration loss or mass transfer loss can be calculated from the Nernst potential difference between the bulk and TPB site:

$$V_{conc} = -\frac{R_g T}{n_e F} \ln\left(\frac{p_{r,H_2} p_{H_2O}}{p_{H_2} p_{r,H_2O}}\right) \quad (9)$$

where $p_{H_2}^i$ is the inlet hydrogen pressure; p_{r,H_2} is the hydrogen pressure within the electrode;

$p_{H_2O}^i$ is the inlet water vapor pressure; and p_{r,H_2O} is the water vapor pressure within the

electrode. The hydrogen and water pressures inside the electrode can be calculated by:

$$p_{r,H_2} = p_{H_2}^i - \frac{RTl i_n}{n_e F D_{a(eff)}} \quad \text{and} \quad p_{r,H_2O} = p_{H_2O}^i + \frac{RTl i_n}{n_e F D_{a(eff)}} \quad (10)$$

where l is the anode thickness; and $D_{a(eff)}$ is the anode effective diffusion coefficient.

Pressure gradient in the thickness direction can be obtained by combining the Fickian diffusion and current flux flowing in the electrode as the following:

$$\frac{dp_{H_2}}{dx} = -\frac{R_g T i_n}{2FD_{(eff)}} \quad (11)$$

where $D_{(eff)}$ is the effective diffusion coefficient. This equation is valid for all depths throughout the electrode and can account for hydrogen consumption when combined with the Butler-Volmer equation.

$D_{(eff)}$ can be found by considering binary and Knudsen diffusion models. Binary diffusion occurs where molecular-molecular interactions are dominant, and Knudsen diffusion occurs where molecular-surface interactions are dominant. The binary diffusion coefficient can be calculated with the Chapman-Enskog theory, as seen in Eqs. (12) and (13) (Chan, Khor and Xia, 2001). σ_{AB} is the collision diameter and Ω_{DAB} is the collision integral based on the Lennard-Jones potential. The collision integral can be found with Eq. (13).

M_{H_2} and M_{H_2O} are the molecular weight of hydrogen and water. The average energy well depth is calculated with $\epsilon_{H_2-H_2O} = (\epsilon_{H_2} \epsilon_{H_2O})^{0.5}$ in ergs. ϵ_{H_2} and ϵ_{H_2O} are found from the viscosity of the gas (Cussler, 1984). The average collision diameter is calculated

with $\sigma_{H_2-H_2O} = \frac{\sigma_{H_2} + \sigma_{H_2O}}{2}$. σ_{H_2} and σ_{H_2O} are the collision diameters of the specie molecules

in angstroms (Reid, 1987).

$$D_{H_2-H_2O} = 0.0018583 \left(\frac{1}{M_{H_2}} + \frac{1}{M_{H_2O}} \right)^{\frac{1}{2}} \frac{T^{1.5}}{P_a \sigma_{H_2-H_2O}^2 \Omega_{D,H_2-H_2O}} \quad (12)$$

$$\Omega_{D,H_2-H_2O} = \frac{A}{(T^*)^B} + \frac{C}{\exp(DT^*)} + \frac{E}{\exp(FT^*)} + \frac{G}{\exp(HT^*)} \quad (13)$$

where, $T^* = \frac{KT}{\epsilon_{H_2-H_2O}}$, $A = 1.06036$, $B = 0.15610$, $C = 0.19300$, $D = 0.47635$, $E = 1.03587$, $F = 1.52996$, $G = 1.76474$, $H = 3.89411$.

The Knudsen diffusion coefficient can be calculated with Eq. (14) (Chan and Xia, 2001; Anthony L. Hines, 1985) for gas specie A , where d_{pore} is the diameter of the pore.

$$D_{AK} = 48.5d_{pore}\sqrt{\frac{T}{M_A}} \quad (14)$$

The effective diffusion coefficient can be found with Eq. (15), where ϵ and τ represent porosity and tortuosity of the porous structure.

$$D_{A(eff)} = \frac{\epsilon}{\tau} \left(\frac{1}{D_{AB}} + \frac{1}{D_{AK}} \right)^{-1} \quad (15)$$

where, tortuosity τ can be estimated by using the model described in (Lanfrey, Kuzeljevic and Dudukovic, 2010).

The micro model was developed by Costamagna et al (Costamagna et al., 1998) based on the theory of random packed spheres to describe electrode microstructure. The micro model considers parameters, which includes porosity, particle size, particle coordination number, electronic-ionic conductor size ratio, electronic-ionic conductor particle number fraction, and bulk material conductivities. The model then outputs effective resistivity and pore size, which are transferred to the macro model to calculate the Ohmic loss and the concentration loss.

The spheres are a binary mixture of electronic and ionic conducting particles with a contact angle between them to account for sintering. In this model, the parameter R_P was

defined as the ratio of ionic conducting particles as the matrix to the electronic conducting particles, as seen in Eq. (16).

$$R_p = \frac{r_{io}}{r_{el}} \quad (16)$$

The mixture of binary particles has the following coordination number based on the particle type as seen in Eq. (17). The coordination number Z equals 6 in a random packing sphere system, and n_{el} and n_{io} are the number fraction of electronic and ionic conducting particles.

$$Z_{el} = 3 + \frac{Z-3}{n_{el} + (1-n_{el})R_p^2} \quad \text{and} \quad Z_{io} = 3 + \frac{(Z-3)R_p^2}{n_{io} + (1-n_{io})R_p^2} \quad (17)$$

The volume fraction can be found from the R_p ratio and the number fraction of conducting particles of that phase as seen in Eq. (18).

$$\varphi_{el} = \frac{n_{el}}{n_{el} + (1-n_{el})R_p^3} \quad \text{and} \quad \varphi_{io} = \frac{n_{io}}{n_{io} + (1-n_{io})R_p^3} \quad (18)$$

The chance of electrical or ionic percolation occurring is based upon the probability of a continuous cluster of conducting particles from the electrolyte to the electrode free surface existing in the electrode. Costamagna et al used Eq. (19), developed by Bouvard, modifying the coefficients based on the experimental determination of $Z_{m-m}=1.764$ by Kuo et al (Kuo and Gupta, 1995). Subscript m denotes the particle conducting phase.

$$P_m = \left(1 - \left(\frac{4.236 - Z_{m-m}}{2.472}\right)^{2.5}\right)^{0.4} \quad (19)$$

It was shown that Suzuki's model was accurate for $0.154 < R_p < 6.464$. Suzuki's model utilized Eq. (20) (Suzuki and Oshima, 1983).

$$Z_{el-el} = \frac{n_{el}Z}{n_{el} + (1-n_{el})R_p^2} \text{ and } Z_{io-io} = \frac{n_{io}Z}{n_{io} + (1-n_{io})R_p^{-2}} \quad (20)$$

The number of particles per unit volume n_t can be calculated with Eq. (21). Eqs. (21)

and (22) are used when $R_p > 1$.

$$n_t = \frac{1 - \varepsilon}{\frac{4}{3} \pi r_{el}^3 (n_{el} + (1-n_{el})R_p^3)} \quad (21)$$

The area of TPBs A between the spheres per volume can be calculated with Eq. (22).

θ is the contact angle of the smaller particle.

$$A = \frac{\pi (r_{el} \sin(\theta_{el}))^2 n_t n_{el} n_{io} Z_{el} Z_{io} P_{el} P_{io}}{Z} \quad (22)$$

If $R_p < 1$, then Eqs. (23) and (24) should be utilized. Notice that θ is based on the smaller particle. If $R_p = 1$, then either equation set can be used.

$$n_t = \frac{1 - \varepsilon}{\frac{4}{3} \pi r_{io}^3 (n_{io} + (1-n_{io})R_p^{-3})} \quad (23)$$

$$A = \frac{\pi (r_{io} \sin(\theta_{io}))^2 n_t n_{el} n_{io} Z_{el} Z_{io} P_{el} P_{io}}{Z} \quad (24)$$

The effective resistivity can be calculated by using Eq. (25), rewritten from Costamagna (Costamagna et al., 1998). γ is the necking factor between the contacting particles, and $\gamma = 0.5$ is commonly accepted value (Costamagna et al., 1998; Chan and Xia, 2001). The critical number fraction is obtained from percolation theory critical thresholds for a randomly packed bimodal spheres (Liu, Kim, Hillier and Chandra, 2011; Liu et al., 2010a; Anthony L. Hines, 1985).

$$\rho_{el(eff)} = \frac{(1-n_{el,cr})^2}{\gamma \sigma_{el} (n_{el} - n_{el,cr})^2} \text{ and } \rho_{io(eff)} = \frac{(1-n_{io,cr})^2}{\gamma \sigma_{io} (n_{io} - n_{io,cr})^2} \quad (25)$$

Pore diameter can be calculated from Eq. (26) (Nam and Jeon, 2006).

$$d_{pore} = \frac{2}{3} \frac{d_{el} \varepsilon}{(1-\varepsilon)} \frac{n_{el} + (1-n_{el})R_p^3}{n_{el} + (1-n_{el})R_p^2} \quad (26)$$

The second-order derivative of total voltage loss can be expressed as Eq. (27) using Butler-Volmer equation coupled with mass transport equation (Costamagna et al., 1998; Chan and Xia, 2001; Ni et al., 2007c). By combining Eqs. (5), (6), (7), (10) and (11), the system of coupled differential equations that is used for the anode can be represented as Eqs (27), (28) and (29). p_a is the total pressure on anode, and $p_a = p_{r,H_2} + p_{r,H_2O}$. Eqs. (27), (28), and (29) can be easily modified and used for the cathode as well.

$$\frac{d^2 V_{loss}}{dx^2} = (\rho_{el(eff)} + \rho_{io(ef)f}) Ai_o \left[\frac{p_{r,H_2}}{p_{H_2}^i} \exp\left(\frac{\beta n F V_{loss}}{RT}\right) - \frac{p_a - p_{r,H_2}}{p_a - p_{H_2}^i} \exp\left(- (1-\beta) \frac{n F V_{loss}}{RT}\right) \right] \quad (27)$$

$$\frac{dp_{r,H_2}}{dx} = - \frac{RT}{2F} \frac{i_{el}}{\left(1 - \frac{p_{r,H_2}}{p_a}\right) D_{H_2(eff)} + \left(\frac{p_{r,H_2}}{p_a}\right) D_{H_2O(eff)}} \quad (28)$$

$$\frac{di_{el}}{dx} = - Ai_o \left[\frac{p_{r,H_2}}{p_{H_2}^i} \exp\left(\frac{\beta n F V_{loss}}{RT}\right) - \frac{p_a - p_{r,H_2}}{p_a - p_{H_2}^i} \exp\left(- (1-\beta) \frac{n F V_{loss}}{RT}\right) \right] \quad (29)$$

The boundary conditions for this coupled, boundary value equation system are summarized in Table 10.

Table 10. Boundary conditions for the electrode.

$x=0$ (free surface)	$\frac{dV_{loss}}{dx} = \rho_{el(eff)} i_{el}$ and $i_{el} = I_t$ $p_{H_2} = p_{H_2}^i$
$x=l$ (Interface between electrode and electrolyte)	$\frac{dV_{loss}}{dx} = \rho_{io(ef)} i_{io}$

After the distribution of total voltage loss is calculated, the overall electrode charge transfer resistance can be determined.

$$R_{ct} = \frac{V_{loss}}{I_t} \quad (30)$$

where I_t is the total current density in the electrode.

5.4 Model validation

The developed model was validated against experimental work by Jiang et al (Jiang et al., 2005). The model parameters used for the validation are shown in Table 11. Figure 41(a) and (b) show Jiang et al's (Jiang et al., 2005) experimental data with the fitted model curves. It can be seen that a reasonable fit was obtained for both YSZ doping levels and both operating temperatures. The exchange current density was the only fitting parameter used and was between 1000 A m^{-2} and 6500 A m^{-2} . These values are reasonable when compared with those found in literatures (Virkar et al., 2000; Chan and Xia, 2001; Zhao and Virkar, 2005). In the validated model, actual electronic and ionic particle sizes reported in Jiang et al's work were used. Images of their electrochemical impedance spectroscopy measurement suggested that the cell may have suffered significant concentration loss. Therefore, the tortuosity used for fitting the experimental data was larger than those commonly accepted values for structures with porosity around 30%. The contribution of each voltage loss terms are separately plotted in Figure 41(b). The diffusion loss accounts for about 30% of total losses, which may likely occur in an anode-supported SOFC with thick catalyst doping.

Table 11. Values of model parameters used in validation.

Model Parameter	Value
Anode thickness (μm)	150
YSZ/Ni volume fractions (unitless) (Jiang et al., 2005)	0.17/0.21
Electronic particle diameter (μm) (Jiang et al., 2005)	1.28
Ionic particle diameter (μm) (Jiang et al., 2005)	0.1
Porosity (unitless)	0.3
Tortuosity (unitless) (Costamagna et al., 1998; Ni et al., 2007c)	4.5
Necking factor (unitless) (Costamagna et al., 1998)	0.5
Hydrogen supply pressure (Pa) (Chan and Xia, 2001)	98261
Anode electronic conductivity, Nickel (S m^{-1}) (Chan and Xia, 2001)	2×10^6
Anode ionic conductivity, YSZ (S m^{-1}) (Leah, Brandon and Aguiar, 2005)	$2.706 \times 10^6 \exp(-0.64/(8.6173 \times 10^{-5}T))/T$

The developed model was also validated against our previous experiment works (Liu et al., 2011; Liu et al., 2010a). Three types of anodes with different microstructures were fabricated by ultrasonic spray pyrolysis. Three different test sample preparation conditions, sample microstructure details and morphology are listed and shown in Table 12 and Figure 42. Table 13 shows the validation results and the values of model parameters used in validation. The modeling results agree well with experimental data and the discrepancy is smaller than 10%.

Table 12. Test sample preparation condition and sample microstructure information

#	Precursor solution concentration C (mol l ⁻¹)	Deposition temperature T (K)	Average deposition particle size d_p (μm)	Deposited film porosity ε (%)	Deposited film thickness l (μm)
1	0.4	523	17	36	37
2	0.025	523	2.5	22	23
3	0.025	623	1.5	34	18

*Precursor solution feed rate fixed as 1.23 ml min⁻¹

Table 13. Test sample preparation condition and sample microstructure information**(a) Model validation with experimental results**

Test sample #	Test temperature (K)	Electrode charge transfer resistance (Ω cm ²) Experiment	Electrode charge transfer resistance (Ω cm ²) Model	Discrepancy (%)
1	1036	1.731	1.780	2.83
1	986	3.011	3.114	3.42
1	936	5.460	5.958	9.12
2	1036	0.808	0.803	0.62
2	986	1.469	1.540	4.83
2	936	2.587	2.813	8.74
3	1036	0.591	0.597	1.02
3	986	0.944	1.010	7.00
3	936	1.678	1.826	8.82

Table 13. (Continued) (b) Values of model parameters used in validation

Model Parameter		Value
Temperature (K)	T	1036//986//936
Total pressure on anode (Pa)	p_a	101300
Pressure of hydrogen (Pa) (Chan and Xia, 2001)	$p_{H_2}^i$	86105
Pressure of oxygen (Pa)	$p_{H_2O}^i$	21273
Electronic number fraction (unitless)	n_{el}	(#1) 0.384 // (#2) 0.468 // (#3) 0.396
Ionic number fraction (unitless)	n_{io}	(#1) 0.256 // (#2) 0.312 // (#3) 0.264
Exchange current of anode ($A\ m^{-2}$)	$i_{o(a)}$	(#1) 2375 // (#2) 4500 // (#3) 4735
Thickness of anode (μm)	l	(#1) 37 // (#2) 23 // (#3) 18
Electronic conductor in anode ($S\ m^{-1}$) $\times 10^6$ (Gil, Moure and Tartaj, 2007)	σ_{el}	5.31@1036K // 5.16@986 // 5.08@936
Ionic conductor in anode ($S\ m^{-1}$) (Leah et al., 2005)	σ_{io}	$2.706 \times 10^6 \exp(-0.64/(8.6173 \times 10^{-5} T))/T$
Porosity (unitless)	ε	(#1) 0.36 // (#2) 0.22 // (#3) 0.34
Tortuosity (unitless) (Lanfrey et al., 2010)	τ	(#1) 1.9 // (#2) 4 // (#3) 2.0
Number of electrons in reaction (unitless) (Yoon et al., 2007; Zhu and Kee, 2003; Noren and Hoffman, 2005)	n	1
Necking factor (unitless) (Costamagna et al., 1998)	γ	0.5
Symmetry factor (unitless) (Chan and Xia, 2001; Lee and Bae, 2008; Ni et al., 2007c; Kim, Virkar, Fung, Mehta and Singhal, 1999)	β	0.5
Faraday's constant ($C\ mol^{-1}$)	F	96485
Gas constant ($J\ (mol \cdot K)^{-1}$)	R	8.314

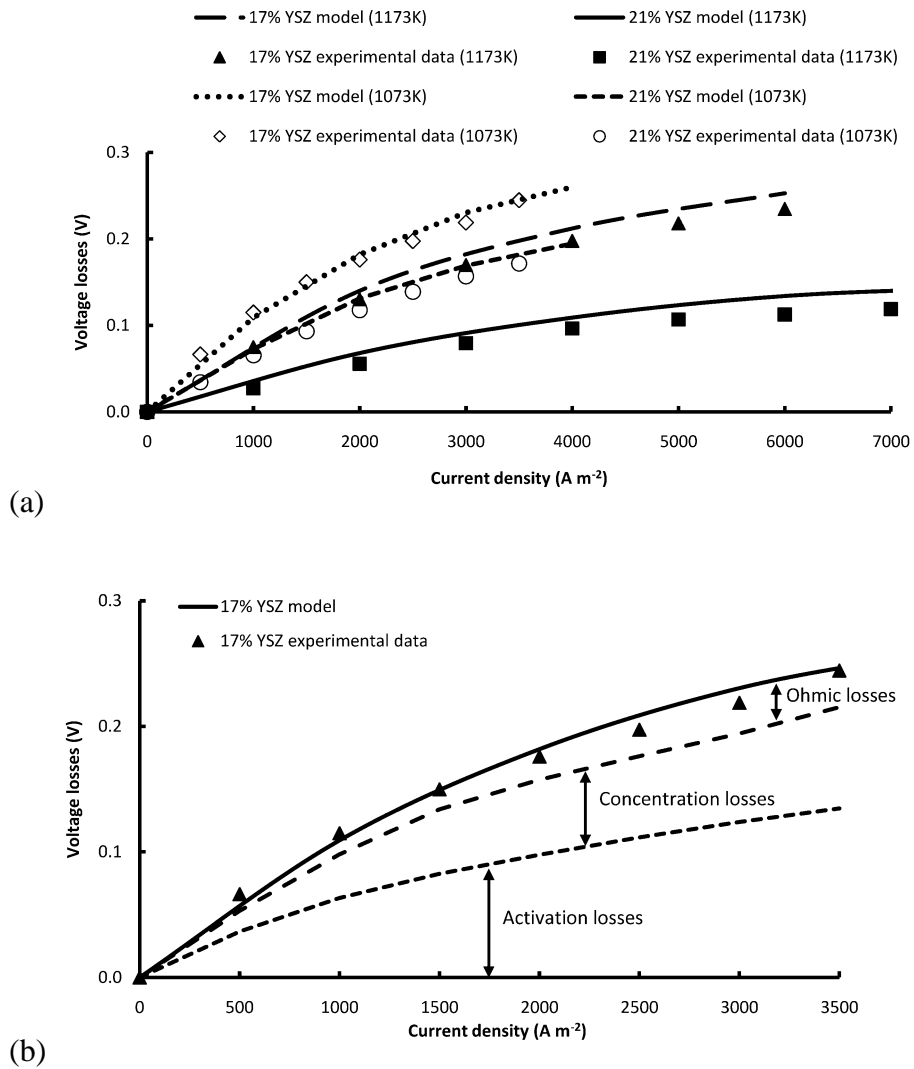


Figure 41. Comparison between model simulation and experimental data of Jiang et al: (a) voltage losses at 1073 K and 1173K and (b) individual voltage losses at 1073 K.

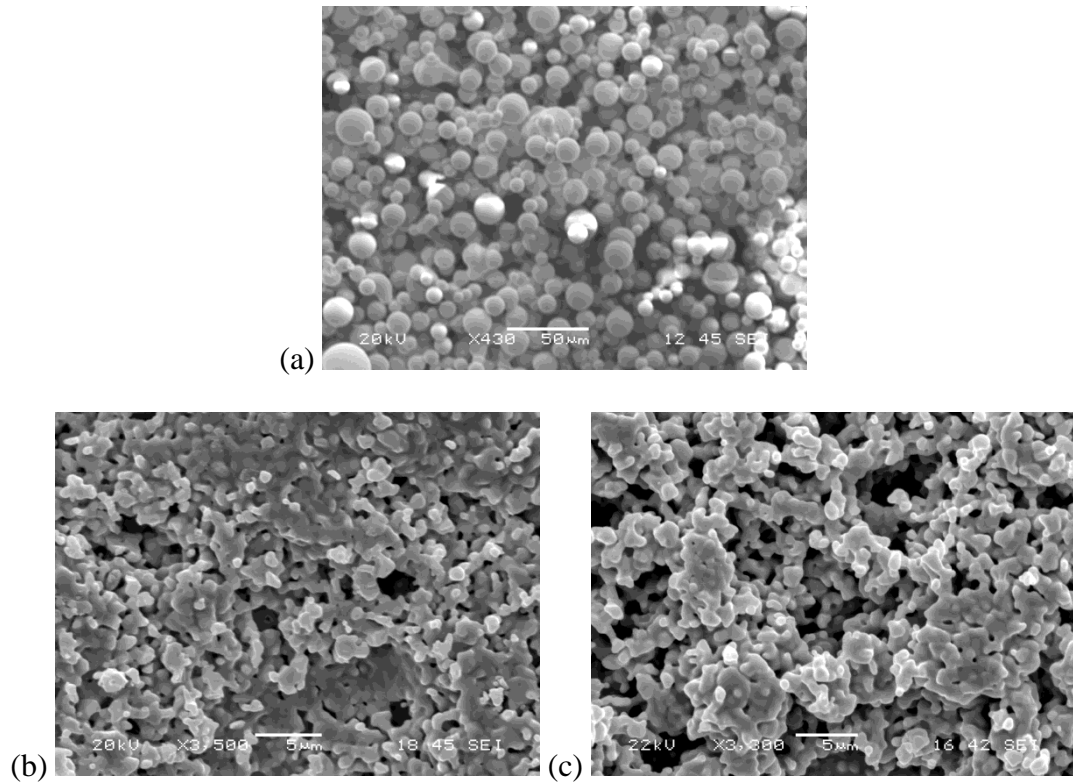


Figure 42. SEM images of anode microstructures: (a) Sample #1 ($d_p = 17 \mu\text{m}$, $\varepsilon = 36\%$), (b) Sample #2 ($d_p = 2.5 \mu\text{m}$, $\varepsilon = 22\%$) and (c) Sample #3 ($d_p = 1.5 \mu\text{m}$, $\varepsilon = 34\%$).

5.5 Results and discussion

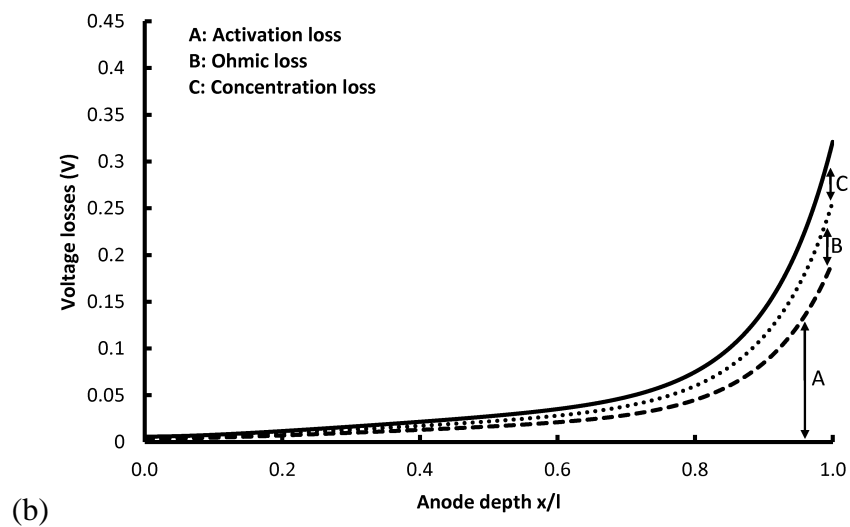
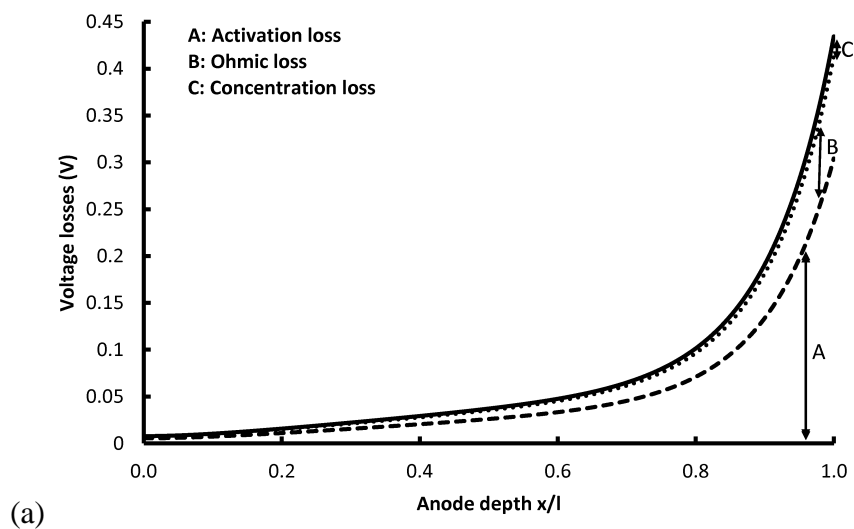
In the following sections, the developed model is used to study the electrochemical performance of homogenous and graded anodes in a SOFC. Particle size and porosity grading range effects on grading profile and voltage losses are investigated.

5.5.1. Analysis of homogenous anodes

Typical SOFC electrodes have a homogenous microstructure. Three test samples with different homogenous microstructures are analyzed to evaluate their electrochemical

performance using the developed model. Figure 43 shows the voltage loss distributions of three different test samples. Activation loss, ohmic loss and concentration loss were separated from the total voltage loss. The activation loss is the most dominant loss, which relates to TPBs area and activation energy closely. With decreasing the electrode particle size, the TPBs area dramatically increases based on the model prediction (Eqn. 22), as shown in Figure 44. The electrochemical performance of the different anode structures was evaluated using electrochemical impedance spectroscopy. The impedance results (Table 13) show a clear decrease in the charge transfer resistance with increasing temperature, as well as a decrease in charge transfer resistance among Samples #1, #2 and #3. Prior research has shown that this decrease in particle size increases the TPBs and, thereby, improves the performance of deposited electrode (Li et al., 2010). This improvement in electrode performance is clearly seen here, where the charge transfer resistance also decreased from $5.460 \Omega \text{ cm}^2$ for Sample #1 to $0.591 \Omega \text{ cm}^2$ for Sample #3 at 936 K. Notably, these resistance values are within the typical range reported in the literature (Muecke et al., 2008; Primdahl and Liu, 2002; Ishihara et al., 2000). The temperature dependent electrode charge transfer resistances that were measured could be used to determine the activation energy (E_a) of the different electrodes. The activation energies as determined from the impedance tests are provided in the Arrhenius plot in Figure 45. A decrease in the activation energy is observed when comparing Sample #1, #2 and #3. The decreasing trend of percentage of activation loss in the total voltage loss matches experimental results, as shown in Figure 43. Higher gas diffusion also helps to improve SOFC performance by lowering the concentration

loss. It can be seen from Figure 46, diffusion coefficients, vary dramatically with different electrode particle sizes. The diffusion coefficient can be increased by adopting larger electrode particle size. With similar electrode particle size, higher porous structure also helps to obtain higher gas diffusion.



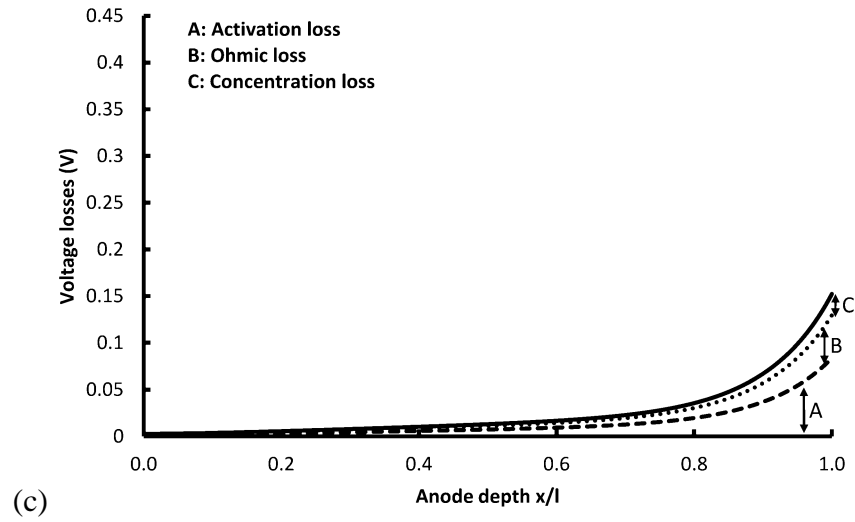


Figure 43. Voltage loss distribution: (a) Sample #1, (b) Sample #2 and (c) Sample #3

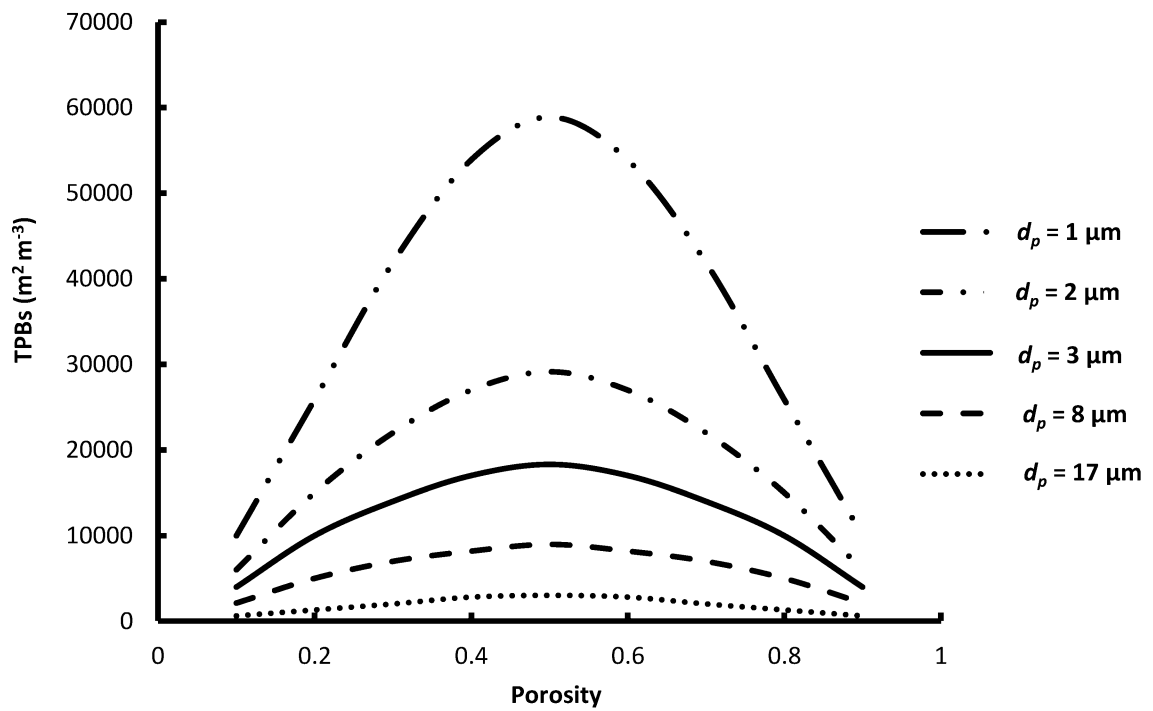


Figure 44. TPBs reaction area versus electrode particle size

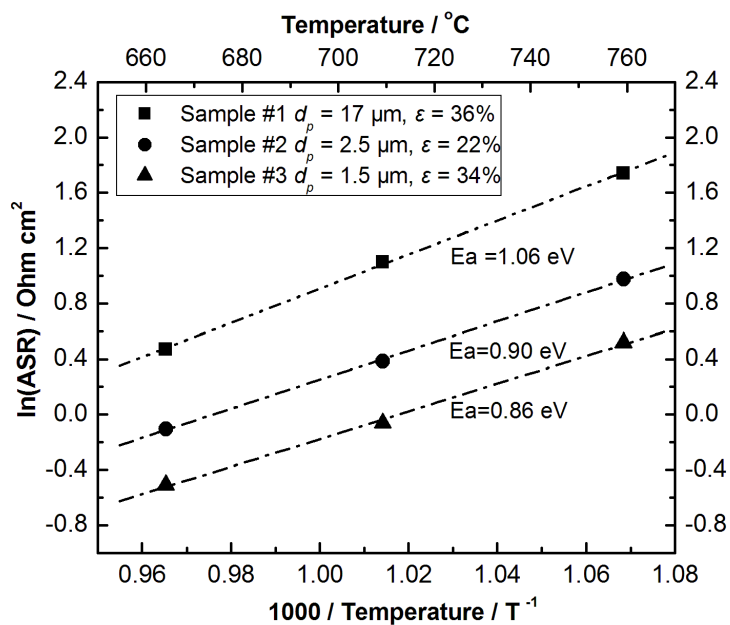


Figure 45. Nyquist plots depicting EIS results for various samples at three test temperatures: Sample #1 ($d_p = 17 \mu\text{m}$, $\varepsilon = 36\%$), Sample #2 ($d_p = 2.5 \mu\text{m}$, $\varepsilon = 22\%$) and Sample #3 ($d_p = 1.5 \mu\text{m}$, $\varepsilon = 34\%$).

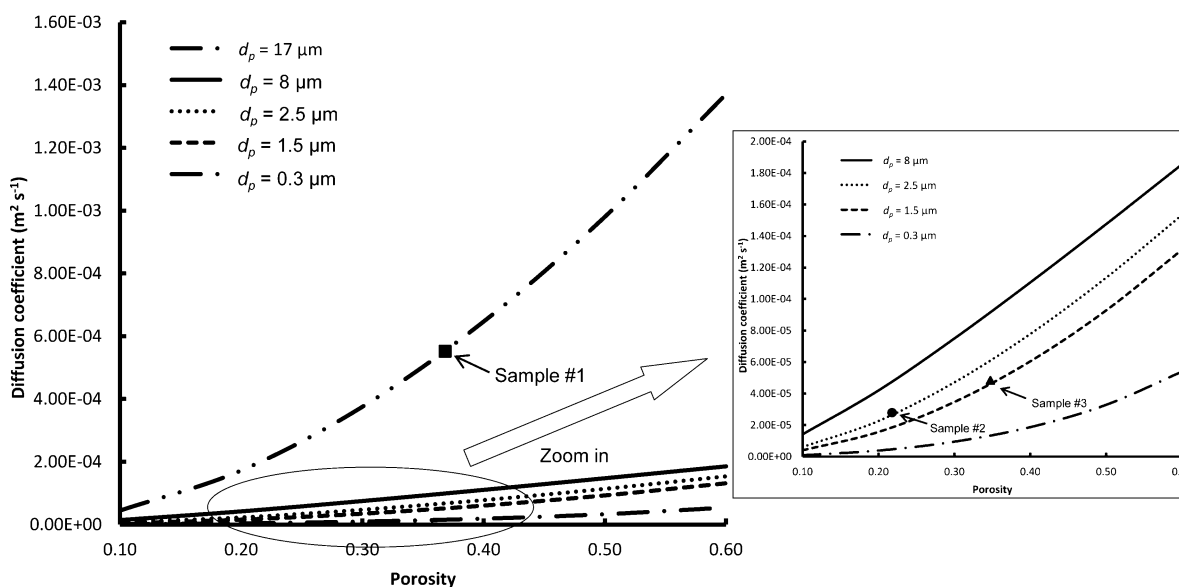


Figure 46. Diffusion coefficients for three test samples: Sample #1 ($d_p = 17 \mu\text{m}$, $\varepsilon = 36\%$), Sample #2 ($d_p = 2.5 \mu\text{m}$, $\varepsilon = 22\%$) and Sample #3 ($d_p = 1.5 \mu\text{m}$, $\varepsilon = 34\%$).

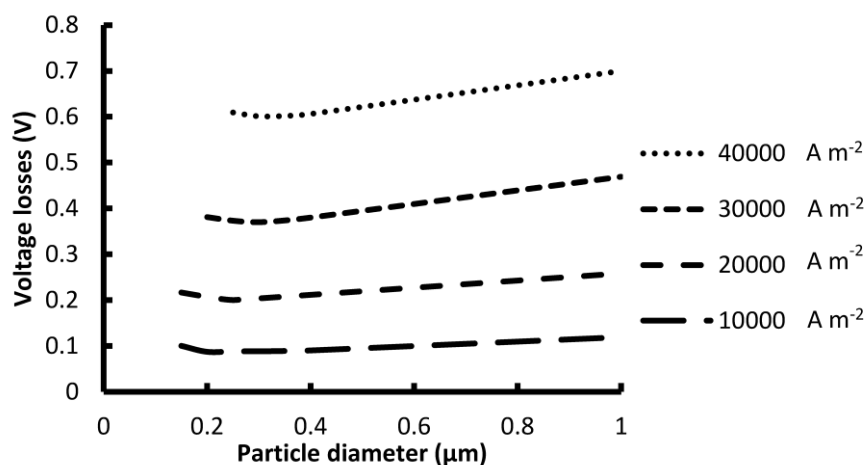
5.5.2. Effect of particle size grading

The experimental and modeling work in the previous section confirm the idea that an electrode microstructure with large TPBs reaction area and high diffusion ability can improve the performance of a SOFC. Particle size graded electrode can significantly increase the area of TPBs. A typical particle size grading scheme of a SOFC anode microstructure is illustrated in Figure 40(b). Smaller particle structures have larger TPBs area but have smaller diffusion coefficients as shown in Figure 46. On the other hand, at bigger particle sizes, the TPBs area is small and diffusion coefficients are large. Therefore, a particle size graded anode can take advantage of the large TPBs reaction area near the anode-electrolyte interface where the reactions primarily occur, and without suffering from high diffusion losses by using larger particles near the free surface.

Table 14 shows the input model parameters used in this study. The effects of particle size on the voltage loss at different current densities were investigated, as shown in Figure 8. It shows the existence of optimal particle size for a given current density in a homogeneous electrode system. If the particle size is increased from the optimal one, overall losses increase from growing activation losses. If the particle size is reduced from the optimal size, overall losses increase from growing diffusion losses. The optimal particle size decreases with increasing current density until 30000 A m^{-2} and increases for larger current densities as observed in Figure 47.

Table 14. Values of model parameters used in the study

Model Parameter		Value
Temperature (K)	T	1036
Total pressure on anode (Pa)	p_a	101300
Pressure of hydrogen (Pa) (Chan and Xia, 2001)	$p_{H_2}^i$	86105
Pressure of oxygen (Pa)	$p_{H_2O}^i$	21273
Electronic number fraction (unitless)	n_{el}	0.36
Ionic number fraction (unitless)	n_{io}	0.26
Exchange current of anode ($A\ m^{-2}$)	$i_{o(a)}$	4000
Thickness of anode (μm)	l	150
Electronic conductor in anode ($S\ m^{-1}$) $\times 10^6$ (Gil et al., 2007)	σ_{el}	5.31@1036K
Ionic conductor in anode ($S\ m^{-1}$) (Leah et al., 2005)	σ_{io}	$2.706 \times 10^6 \exp(-0.64/(8.6173 \times 10^{-5}T))/T$
Porosity (unitless)	ε	0.30
Tortuosity (unitless) (Lanfrey et al., 2010)	τ	2.0
Number of electrons in reaction (unitless) (Yoon et al., 2007; Zhu and Kee, 2003; Noren and Hoffman, 2005)	n	1
Necking factor (unitless) (Costamagna et al., 1998)	γ	0.5
Symmetry factor (unitless) (Chan and Xia, 2001; Lee and Bae, 2008; Ni et al., 2007c; Kim et al., 1999)	β	0.5
Faraday's constant ($C\ mol^{-1}$)	F	96485
Gas constant ($J\ (mol \cdot K)^{-1}$)	R	8.314

**Figure 47. Voltage loss versus particle diameter at different current densities.**

The following symmetrical equations were developed and implemented to study the linear and nonlinear particle size and porosity grading. Eqn. (31) and Eqn. (32) can be used to obtain particle size grading profiles with concave up shape and concave down shape respectively, shown in Figure 48:

$$d_p = \frac{(d_f - d_i)}{d_f} \left(\frac{(b^2 + lb)d_f}{l(x+b)} + d_f - \left(\frac{d_f(b^2 + lb)}{lb} \right) \right) + d_i \quad (31)$$

$$d_p = \frac{(d_f - d_i)}{d_f} \left(\frac{(b^2 + lb)d_f}{l(x-l-b)} - d_f + \left(\frac{d_f(b^2 + lb)}{lb} \right) \right) + d_f \quad (32)$$

where, b is the shape factor that controls the nonlinearity of the particle size grading profile; d_f is the particle diameter at free surface; and d_i is the particle diameter at the interface between the anode and electrolyte. When $b = 1$, the particle size grading profile is linear. If $b < 1$, the particle size grading profile is nonlinear. The electrode free surface is at $x = 0$, and anode-electrolyte interface surface is at the end of the x axis, shown in Figure 48.

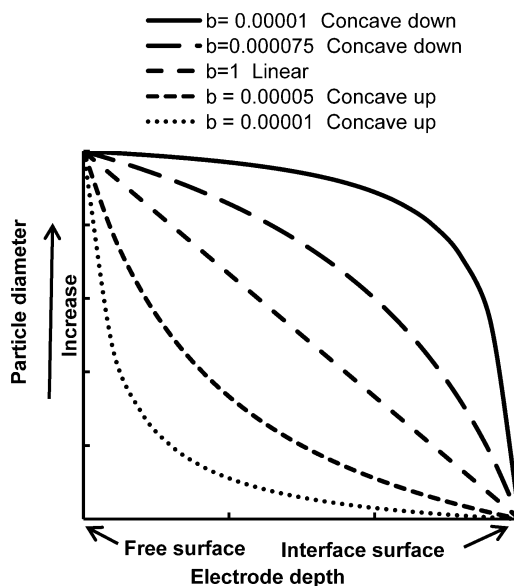


Figure 48. Particle size grading profiles used in this study

The performance of linearly graded anode was studied where the minimum particle size at the anode-electrolyte interface was fixed at 0.3 μm . The particle size grading range was varied until the best performing particle size was found. The particle size at anode free surface of 3 μm gave the best performance with lowest polarization. A 10.5% decrease in voltage loss at 20000 A m^{-2} over the limited homogeneous case was observed. In the meanwhile, nonlinear grading anode performance was investigated with two different grading ranges of particle size, one with smaller range (0.3–0.6 μm) and the other with larger range (0.3–8.0 μm). For both grading ranges, the grading profile was varied until the best performing profile was found (i.e. a grading profile with least voltage loss). Table 15 summarizes the results of both linear and nonlinear graded anode performance. As the particle size grading range becomes larger, the voltage losses can be decreased with the appropriate grading profile. And the performance of the nonlinearly graded anode performances prevails against the performances of homogeneous and linear optimized structure.

Table 15. Summary of particle size grading

Grading Profile	Anode Particle Diam. (μm)	Voltage Loss at 20000 A m^{-2} (V)
Homogeneous	0.3	0.219
Concave Down	0.3→0.6	0.216
Linear	0.3→3	0.196
Concave Up	0.3→8	0.192

5.5.3. Effect of porosity grading

Varying porosity can also improve a SOFC electrochemical performance based on the experimental and modeling analysis in section 4.1. Figure 40(c) shows a schematic of a typical porosity grading microstructure of SOFC anode. Table 16 shows the percent reduction in voltage losses between the optimized homogeneous and linearly graded structures, along with the reduction in losses between homogeneous and nonlinearly graded anodes. All particle sizes investigated showed a noticeable benefit when linear grading was introduced to the system, although there was more benefit seen when nonlinear grading was used. When a concave down grading profile and increased grading range were used, the nonlinear grading profile showed improvement in the 0.3 μm case. This reduced the diffusion losses by increasing the mean pore size in the anode structure. The widened grading range, for the 0.3 μm nonlinear case, increased the activation reaction area near the anode-electrolyte interface where diffusion is not as much of a concern. In the 3 μm case, linear grading minimized the balance of the activation and concentration losses. Nonlinear grading was detrimental to the anode's performance when introduced. Of all the cases studied, the nonlinear 0.3 μm structure had the lowest losses, while the homogeneous 3 μm structure had the highest. Losses are not reduced as effectively with porosity grading as particle size grading. This is due to reaction area changing squarely with changing particle size and parabolically with changing porosity. Also, particle size grading can range over two orders of magnitude is advantageous when porosity grading cannot.

Table 16. Percent voltage loss reduction from a homogeneous anode microstructure

Particle diameter	Linear	Nonlinear
0.3 μm	6.3% (porosity 30-60%)	10.3% (porosity 10-60%)
0.8 μm	6.8% (porosity 20-60%)	3.1% (porosity 10-60%)
3 μm	4.1% (porosity 10-60%)	-0.3% (porosity 10-60%)

5.6 Conclusion

The aim of this work was to understand the effects of electrode microstructure grading on a SOFC performance. In this study, a fundamental theory-based numerical model has been proposed and developed to evaluate the effects of electrode microstructure variation on a SOFC performance. The modeling approach integrated two models: a macro model and a micro model. The macro model describes the overall cell behavior through activation, Ohmic, and concentration losses based on chemical and concentration potentials. With the consideration of electrode microstructure parameters, the micro model outputs electrode effective conductivity, TPBs area and pore size. The micro model output data are then integrated into the macro model. A full SOFC electrode polarization model is developed from this compilation.

The model can effectively provide insight into the evaluation of electrochemical performance with designed SOFC electrodes. All three major loss distributions can be obtained and separated from the overall voltage loss. Three deposited SOFC anode samples have been analyzed by the model. The results demonstrated the potential of graded microstructure can improve the electrochemical performance of a SOFC. The concept of nonlinearly graded microstructures in a SOFC electrode was explored for the first time in this

work. This study investigated the particle size and porosity grading range effects on grading profile, including linear and nonlinear profiles, and voltage losses. It has been shown that a larger particle size grading range (0.3–8 μm) is more effective at reducing voltage losses than smaller ranges. Linear grading showed reduced voltage losses over homogeneous anodes. Nonlinear grading demonstrated particular benefit over linear and homogenous microstructures. Particle size grading was more effective at reducing losses in a SOFC anode than porosity grading because the reaction area increased squarely with decreasing particle size, but parabolically with decreasing porosity. Also, the fact that particle size grading can range over two orders of magnitude is advantageous when porosity grading cannot.

This study experimentally and numerically demonstrated the potential of controlling the electrode microstructure of a SOFC to improve the cell's electrochemical performance. The work contributed to the understanding of cell performance in relation to graded microstructures. Based on the model simulation, a design guideline can be provided, which can aid selection and development of fabrication process that can further improve SOFC performance.

CHAPTER 6. SUMMARY AND SCIENTIFIC CONTRIBUTIONS

6.1 Summary

The dissertation provided insight into the analysis of the reliability of SOFC, and a deeper understanding of SOFC electrode electrochemical performance in different controlled microstructures through experimental and modeling approaches. A thermo-mechanical model has been developed to predict the cell lifetime based on thermal cycling fatigue. The interfacial and peeling stresses calculated from the mismatch of material mechanical properties were used to estimate the crack nucleation to predict the number of cycles to cell failure. The model can effectively provide insight into the development and distribution of the thermal stresses from the thermal cycling and predict the lifetime of a cell with different geometries and microstructures. Experimental works have also been carried out to fabricate cells with different controlled microstructures. A spray deposition technique has been adopted to establish an economically practical prototype fabrication setup to deposit and tailor the anode cell microstructure, and understand its impact on electrochemical performance of the cell. A detailed experimental work on ultrasonic spray pyrolysis was performed to control and predict the deposited anode electrode microstructure of SOFC. The cell performance was measured by AC electrochemical impedance spectroscopy. In order to fully understand SOFCs electrochemical performance with controlled microstructure, a fundamental theory-based numerical model has been proposed and developed to evaluate the

effects of electrode microstructure variation on a SOFC performance. The possibility of integration of thermo-mechanical model to electrochemical performance model has also been investigated and discussed in this chapter.

6.1.1 Modeling of Thermal Stresses and Lifetime Prediction of Planar Solid Oxide Fuel Cell under Thermal Cycling Conditions

A thermo-mechanical model has been developed to predict the distribution of two types of thermal stresses, interfacial shear stress and peeling stress, in the multilayer structure of SOFC. Thermal stresses are generated from the mismatch of material mechanical properties. They were used to estimate the crack nucleation for the prediction of the number of cycles needed for cell failure. Numerical results were validated against available experimental results, which showed a good agreement. The major findings are summarized as the following:

(1) It was found that the interfacial shear and peeling stresses were more concentrated near the free edge, which theoretically explains the damage near the edges frequently observed in experiments under thermal cycling conditions. For the case of Ni-YSZ-LSM cell, the anode-electrolyte interface was found to be more prone to delamination under thermal cycling.

(2) The simulation results showed that the lifetime of a cell highly depends on its geometric and microstructural parameters. As the porosity and the thickness of anode increased, the lifetime of the cell decreased for the electrolyte supported cell. A similar trend

was found for the anode supported structure where electrolyte porosity and thickness were varied.

(3) The model can efficiently provide insight into the development and distribution of the thermal stresses during thermal cycling and predict the lifetime of a cell. It can be used as an effective tool for designing of the cell structure. The work also provides a foundation for future SOFC reliability and durability research.

6.1.2 Fabrication of Solid Oxide Fuel Cell Anode Electrode by Spray Pyrolysis

This experimental work verified the potential of using ultrasonic spray pyrolysis to control and predict the deposited anode electrode microstructure of a SOFC. The effects of processing parameters, including deposition time, precursor solution concentration, deposition temperature and precursor solution feed rate, on the deposited anode film microstructure and morphology were analyzed. Based on the experimental study, the following conclusions can be drawn:

(1) The EDS and XRD analysis showed that all the elements, nickel, cerium, and gadolinium with corresponding diffraction patterns, were homogeneously distributed on the substrate. Thus, it demonstrated the capability of the developed prototype fabrication setup in dispersing the constitutive elements.

(2) The utilized ultrasonic atomization model can predict the size of deposition particle. The analytical values agreed well with the experimental results. The model can be used as a tool to aid designing SOFC electrode microstructures.

(3) The precursor solution concentration and deposition temperature were the most critical parameters that influenced the microstructure. On the other hand, the precursor solution feed rate only had minimal influence on the deposited anode film microstructure and morphology.

(4) The deposited particle size decreased as the deposition temperature increased and precursor solution concentration decreased. Too low ($< 250^{\circ}\text{C}$) or too high ($> 450^{\circ}\text{C}$) deposition temperature resulted in severe cracks and low deposition rate. The porosity was also significantly affected by deposition temperature and precursor solution concentration. By manipulating these process parameters, the deposited anode electrode particle size and porosity could be controlled in the range of $1.5\text{--}17\ \mu\text{m}$ and $22\%\text{--}54\%$, respectively.

6.1.3 Microstructural and Electrochemical Impedance Study of Ni-CGO Anodes for Solid Oxide Fuel Cells Fabricated by Ultrasonic Spray Pyrolysis

The study demonstrated the potential of using ultrasonic spray pyrolysis to enhance electrochemical performance by tailoring the microstructure of a SOFC anode electrode. A detailed experimental work on the enhancement of electrode electrochemical performance was investigated using AC electrochemical impedance spectroscopy. The findings from the experimental work can be concluded as the following:

(1) The precursor solution concentration ($0.025\text{--}0.4\ \text{mol l}^{-1}$) and deposition temperature ($250\ ^{\circ}\text{C}\text{--}350\ ^{\circ}\text{C}$) significantly influenced the deposited anode microstructure and resulted in change of electrochemical performance.

(2) Decreasing the deposition particle size and increasing the porosity of electrode reduce the polarization resistance and activation energy of the deposited cells. The estimated volume-specific TPB length increased one order of magnitude from $0.33 \mu\text{m} \mu\text{m}^{-3}$ to $3.57 \mu\text{m} \mu\text{m}^{-3}$ as a result of decrease in the particle size and increase in the porosity.

(3) Consistent with the estimated TPB length, the ASR of the deposited anode improved from 5.45 ohm cm^2 to 0.61 ohm cm^2 , and the activation energy decreased from 1.06 eV to 0.86 eV for the temperature range of $663 \text{ }^\circ\text{C}$ to $763 \text{ }^\circ\text{C}$.

(4) Low polarization and activation energy makes the proposed fabrication process a promising candidate for fabricating high performance SOFC electrode with manipulated microstructure.

6.1.4 Modeling of Solid Oxide Fuel Cells Performance with Homogenous and Graded Anode in Particle Size and Porosity

In this study, a fundamental theory-based numerical model has been proposed and developed to evaluate the effects of electrode microstructure variation on a SOFC performance. The modeling approach integrated two models: a macro model and a micro model. Following conclusions have been drawn from this study.

(1) The model can effectively provide insight into the evaluation of electrochemical performance with designed SOFC electrodes. All three major loss distributions can be obtained and separated from the overall voltage loss.

(2) Three deposited SOFC anode samples have been analyzed by the model. The results demonstrated the potential of graded microstructure can improve the electrochemical

performance of a SOFC.

(3) The concept of nonlinearly graded microstructures in a SOFC electrode was explored for the first time in this work. This study investigated the particle size and porosity grading range effects on grading profile, including linear and nonlinear profiles, and voltage losses.

(4) It has been shown that a larger particle size grading range (0.3–8 μm) is more effective at reducing voltage losses than smaller ranges. Linear grading showed reduced voltage losses over homogeneous anodes. Nonlinear grading demonstrated particular benefit over linear and homogenous microstructures.

(5) Particle size grading was more effective at reducing losses in a SOFC anode than porosity grading because the reaction area increased squarely with decreasing particle size, but parabolically with decreasing porosity. In addition, the fact that particle size grading can range over two orders of magnitude is advantageous when porosity grading cannot.

6.2 Scientific Contributions

The major scientific contributions of the dissertation may be summarized as the following:

1. The thermo-mechanical model is one of the first attempts to understand the cyclic failure behavior of multilayer SOFC through theoretical approach. The model is capable of providing thermal stress distribution and crack nucleation in a cell under thermal cycling conditions. The model is able to provide theoretical explanations for the mechanical failures

frequently observed in experiments. This model can contribute towards SOFC reliability and durability research and aid in the analysis and designing of cell structure for reduced thermal stress and longer cell life.

2. The electrode of SOFC with tailored microstructure can be successfully deposited using the economically practical prototype fabrication setup established in this study. The detailed experimental study demonstrated the potential of ultrasonic spray pyrolysis for tailoring the microstructure of SOFC electrode. An ultrasonic atomization model was used and validated to predict the deposition particle size, which was firstly introduced and applied to aid designing SOFC electrode microstructures.

3. The work provided insight on identifying the critical process parameters of ultrasonic spray pyrolysis on the microstructure of tailoring deposition electrode. The precursor solution concentration and deposition temperature were experimentally demonstrated as the most critical parameters that influenced the morphology and porosity of the deposited microstructure. An experimental parameters study revealed those process effects on the deposition a designed electrode microstructure using ultrasonic spray pyrolysis.

4. The experimental results provided a deeper understanding of the relationship between SOFC electrode microstructure and electrochemical performance of the cell. Decreasing the deposition particle size and increasing porosity of the electrode decreased polarization

resistance and activation energy, which was confirmed by AC electrochemical impedance spectroscopy technique. Low polarization and activation energy makes the established prototype fabrication setup a promising candidate for the fabrication of high performance SOFC electrode with tailored microstructure.

5. A fundamental theory-based numerical model has been proposed and developed to evaluate the effects of electrode microstructure variation on a SOFC performance experimentally and numerically. The concept of nonlinearly graded structures, which is likely to occur in an actual fabrication process, in a SOFC electrode was explored for the first time in this work.

6.3 Recommendations for the future work

The dissertation investigated solid oxide fuel cell reliability and performance modeling and fabrication by spray pyrolysis. The developed thermo-mechanical model, electrochemical performance model, and the designed fabrication setup have the potential to be integrated into a whole design, evaluation and fabrication system to aid development of SOFCs with more robustness and improved electrochemical performance. The thermo-mechanical model proposed and developed in this research can aid analysis and design of cell structure to reduce thermal stress and enhance cell life, which will contribute in SOFC reliability and durability research. On the other hand, the electrochemical performance model can effectively provide insight into the evaluation of electrochemical performance with designed SOFC electrodes. All three major loss distributions can be obtained and separated

from the overall voltage loss. A potential pathway to integration of the thermo-mechanical model and electrochemical model is recommended in Fig. 49. The thermal, mechanical and chemical degradation change the mechanical, microstructural, and compositional properties of the SOFC components. By integrating the inputs which influence cell degradation, the developed thermo-mechanical and electrochemical performance models can be coupled to provide both electrochemical performance and cell lifetime. Overall, the integrated model can be used as an effective tool for designing and optimizing the cell structure. The designed fabrication and electrochemical performance setups can be used as experimental tools to validate the integrated model.

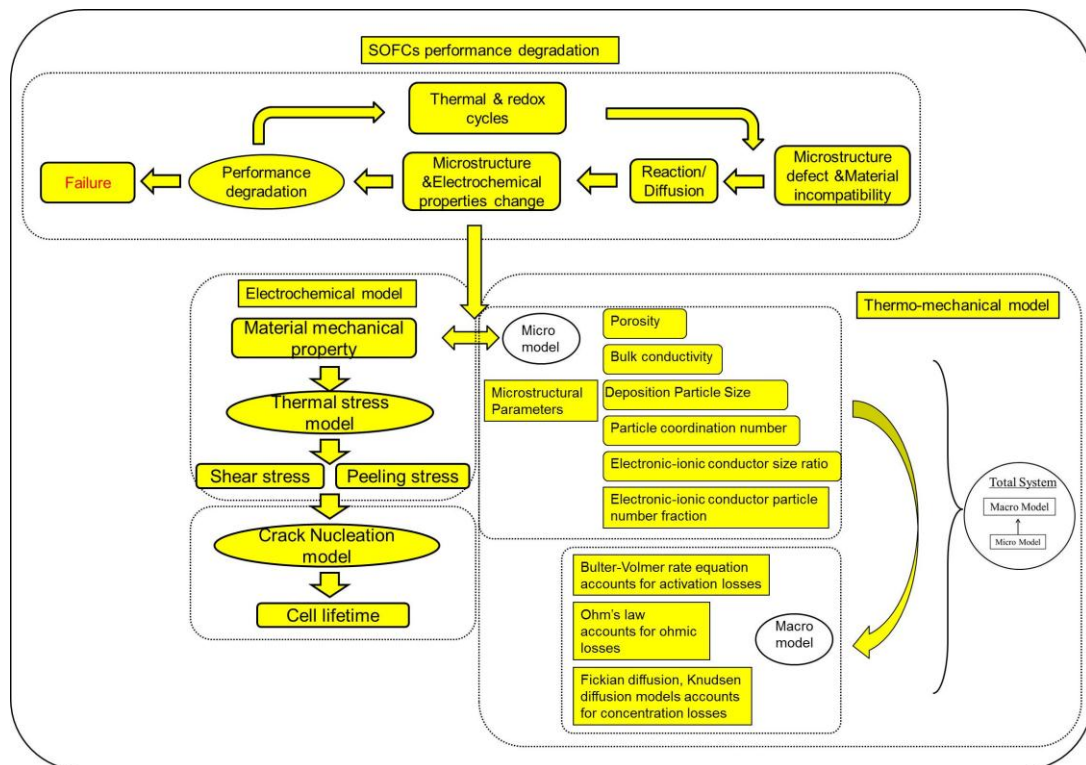


Figure 49. SOFCs thermo-mechanical reliability and electrochemical performance model integration

BIBLIOGRAPHY

Abbasi, M. H., Evans, J. W. and Abramson, I. S. (1983) Diffusion of gases in porous solids: Monte Carlo simulations in the Knudsen and ordinary diffusion regimes, *AIChE Journal*, **29**, 4, pp. 617-624.

Aguiar, P., Adjiman, C. S. and Brandon, N. P. (2004) Anode-supported intermediate temperature direct internal reforming solid oxide fuel cell. I: model-based steady-state performance, *Journal of Power Sources*, **138**, 1-2, pp. 120-136.

Ali, A., Wen, X., Nandakumar, K., Luo, J. and Chuang, K. T. (2008) Geometrical modeling of microstructure of solid oxide fuel cell composite electrodes, *Journal of Power Sources*, **185**, 2, pp. 961-966.

Anderson, T. L. (2005) *Fracture Mechanics Fundamental and Applications*, Taylor & Francis Group, New York.

Anthony L. Hines, R. N. M. (1985) *Mass Transfer: Fundamentals and Applications*, Englewood Cliffs, N.J. : Prentice-Hall Englewood Cliffs, New Jersey.

Aruna, S. T., Muthuraman, M. and Patil, K. C. (1998) Synthesis and properties of Ni-YSZ cermet: anode material for solid oxide fuel cells, *Solid State Ionics*, **111**, 1-2, pp. 45-51.

Atkinson, A. and Selcuk, A. (2000) Mechanical behaviour of ceramic oxygen ion-conducting membranes, *Solid State Ionics*, **134**, 1-2, pp. 59-66.

Barbucci, A., Viviani, M., Carpanese, P., Vladikova, D. and Stoyanov, Z. (2006) Impedance analysis of oxygen reduction in SOFC composite electrodes, *Electrochimica Acta*, **51**, 8-9, pp. 1641-1650.

Beckel, D., Dubach, A., Studart, A. and Gauckler, L. (2006) Spray pyrolysis of La_{0.6}Sr_{0.4}Co_{0.2}Fe_{0.8}O_{3-δ} thin film cathodes, *Journal of Electroceramics*, **16**, 3, pp. 221-228.

Bohac, P. and Gauckler, L. (1999) Chemical spray deposition of YSZ and GCO solid electrolyte films, *Solid State Ionics*, **119**, 1-4, pp. 317-321.

Brahim, C., Ringued, A., Gourba, E., Cassir, M., Billard, A. and Briois, P. (2006) Electrical properties of thin bilayered YSZ/GDC SOFC electrolyte elaborated by sputtering, *Journal of Power Sources*, **156**, 1, pp. 45-49.

Bujalski, W., Dikwal, Chinnan M., Kendall, Kevin (2007) Cycling of three solid oxide fuel cell types, *Journal of Power Sources*, **171**, 1, pp. 96-100.

- Busso, E. P., Tkach, Y. and Travis, R. P. (2001) Thermally induced failure of multilayer ceramic structures, *Philosophical Magazine a-Physics of Condensed Matter Structure Defects and Mechanical Properties*, **81**, 8, pp. 1979-1995.
- Cai, P. Z., Green, D. J. and Messing, G. L. (1997) Constrained densification of alumina/zirconia hybrid laminates .1. Experimental observations of processing defects, *Journal of the American Ceramic Society*, **80**, 8, pp. 1929-1939.
- Chan, S. H., Khor, K. A. and Xia, Z. T. (2001) A complete polarization model of a solid oxide fuel cell and its sensitivity to the change of cell component thickness, *Journal of Power Sources*, **93**, 1-2, pp. 130-140.
- Chan, S. H. and Xia, Z. T. (2001) Anode micro model of solid oxide fuel cell, *Journal of the Electrochemical Society*, **148**, 4, pp. A388-A394.
- Chandra, A., Huang, Y., Jiang, Z. Q., Hu, K. X. and Fu, G. (2000) A model of crack nucleation in layered electronic assemblies under thermal cycling, *Journal of Electronic Packaging*, **122**, 3, pp. 220-226.
- Chang, C.-L., Hsu, C.-S. and Hwang, B.-H. (2008) Unique porous thick $\text{Sm}_{0.5}\text{Sr}_{0.5}\text{CoO}_3$ solid oxide fuel cell cathode films prepared by spray pyrolysis, *Journal of Power Sources*, **179**, 2, pp. 734-738.
- Chen, C. Y., Tseng, T. K., Tsay, C. Y. and Lin, C. K. (2008) Formation of irregular nanocrystalline CeO_2 particles from acetate-based precursor via spray pyrolysis, *Journal of Materials Engineering and Performance*, **17**, 1, pp. 20-24.
- Chen, J. C. and Hwang, B. H. (2008) Microstructure and properties of the Ni-CGO composite anodes prepared by the electrostatic-assisted ultrasonic spray pyrolysis method, *Journal of the American Ceramic Society*, **91**, 1, pp. 97-102.
- Chen, K., Zhe, L., Ai, N., Chen, X., Hu, J., Huang, X. and Su, W. (2007) Effect of SDC-impregnated LSM cathodes on the performance of anode-supported YSZ films for SOFCs, *Journal of Power Sources*, **167**, 1, pp. 84-89.
- Chourashiya, M. G., Pawar, S. H. and Jadhav, L. D. (2008) Syndissertation and characterization of $\text{Gd}_{0.1}\text{Ce}_{0.9}\text{O}_{1.95}$ thin films by spray pyrolysis technique, *Applied Surface Science*, **254**, 11, pp. 3431-3435.
- Choy, K. L. and Su, B. (2001) Growth behavior and microstructure of CdS thin films deposited by an electrostatic spray assisted vapor deposition (ESAVD) process, *Thin Solid Films*, **388**, 1-2, pp. 9-14.

- Colpan, C. O., Dincer, I. and Hamdullahpur, F. (2008) A review on macro-level modeling of planar solid oxide fuel cells, *International Journal of Energy Research*, **32**, 4, pp. 336-355.
- Costamagna, P., Costa, P. and Antonucci, V. (1998) Micro-modelling of solid oxide fuel cell electrodes, *Electrochimica Acta*, **43**, 3-4, pp. 375-394.
- Cussler, E. L. (1984) *Diffusion, Mass Transfer in Fluid Systems*, Cambridge University Press, New York.
- Deng, X. H. and Petric, A. (2005) Geometrical modeling of the triple-phase-boundary in solid oxide fuel cells, *Journal of Power Sources*, **140**, 2, pp. 297-303.
- Deseure, J., Bultel, Y., Dessemond, L. and Siebert, E. (2005a) Theoretical optimisation of a SOFC composite cathode, *Electrochimica Acta*, **50**, 10, pp. 2037-2046.
- Deseure, J., Dessemond, L., Bultel, Y. and Siebert, E. (2005b) Modelling of a SOFC graded cathode, *Journal of the European Ceramic Society*, **25**, 12, pp. 2673-2676.
- E. Tang, D. P., M. Pastula and B. Borglum In: S.C. Singhal and J. Mizusaki, Editors (2005) SOFC IX, *The Electrochemical Society Proceedings Series*, Pennington, NJ p. 89.
- EG&G Technical Services Inc. (2004a) *Fuel Cell Handbook*, 7th Edn, Morgantown, WV.
- EG&G Technical Services Inc. (2004b) *Fuel Cell Handbook*, 7th Edn, Morgantown, WV.
- Faes, A., Nakajo, A., Hessler-Wyser, A., Dubois, D., Brisse, A., Modena, S. and Van herle, J. (2009) RedOx study of anode-supported solid oxide fuel cell, *Journal of Power Sources*, **193**, 1, pp. 55-64.
- Flesner, R. R. (2009) Modeling of Solid Oxide Fuel Cell functionally graded electrodes and a feasibility study of fabrication techniques for functionally graded electrodes, MASTER OF SCIENCE, Mechanical Engineering, Iowa State University.
- FuelCell Energy (March 21, 2007) *Company Update*,
- Fukui, T., Ohara, S., Naito, M. and Nogi, K. (2002) Performance and stability of SOFC anode fabricated from NiO/YSZ composite particles, *International Workshop on Interfaces: Ceramic and metal Interfaces: Control at the Atomic Level*, Jun 23-27, Oviedo, Spain, pp. 2963-2967.
- G. Schiller, T. F., M. Lang, P. Metzger and AO Störmer (2005) Recent Results of the SOFC APU Development at DLR, *9th International Symposium on Solid Oxide Fuel Cells (SOFC-IX)*, , Quebec City, pp. 66-75.

Gil, V., Moure, C. and Tartaj, J. (2007) Sinterability, microstructures and electrical properties of Ni/Gd-doped ceria cermets used as anode materials for SOFCs, *Journal of the European Ceramic Society*, **27**, 13-15, pp. 4205-4209.

Giraud, S. and Canel, J. (2008) Young's modulus of some SOFCs materials as a function of temperature, *Journal of the European Ceramic Society*, **28**, 1, pp. 77-83.

Greene, E. S., Chiu, W. K. S. and Medeiros, M. G. (2006) Mass transfer in graded microstructure solid oxide fuel cell electrodes, *Journal of Power Sources*, **161**, 1, pp. 225-231.

Grew, K. N., Joshi, A. S. and Chiu, W. K. S. (2010) Direct Internal Reformation and Mass Transport in the Solid Oxide Fuel Cell Anode: A Pore-scale Lattice Boltzmann Study with Detailed Reaction Kinetics, *Fuel Cells*, **10**, 6, pp. 1143-1156.

H Tada, P. P., GR Irwin (1985) *The Stress Analysis of Cracks Handbook*, Del. Research, St. Louis.

Haanappel, V. A. C., Mertens, J. and Malzbender, J. (2007) Characterisation of Ni-cermets SOFCs with varying anode densities, *Journal of Power Sources*, **171**, 2, pp. 789-792.

Hagen, A., Barfod, R., Hendriksen, P. V., Liu, Y. L. and Ramousse, S. (2006) Degradation of anode supported SOFCs as a function of temperature and current load, *Journal of the Electrochemical Society*, **153**, 6, pp. A1165-A1171.

Hamedani, H. A., Dahmen, K.-H., Li, D., Peydaye-Saheli, H., Garmestani, H. and Khaleel, M. (2008) Fabrication of gradient porous LSM cathode by optimizing deposition parameters in ultrasonic spray pyrolysis, *Materials Science and Engineering: B*, **153**, 1-3, pp. 1-9.

Han, M., Tang, X., Yin, H. and Peng, S. (2007) Fabrication, microstructure and properties of a YSZ electrolyte for SOFCs, *Journal of Power Sources*, **165**, 2, pp. 757-763.

Hart, N. T. (2004) Scale-up of the IP-SOFC to multi kilowatt levels, *DTI/F/01/00197/REP*, **URN 04/556**,

Hart, N. T., Brandon, N. P., Day, M. J. and Lapena-Rey, N. (2002) Functionally graded composite cathodes for solid oxide fuel cells, *Journal of Power Sources*, **106**, 1-2, pp. 42-50.

Herbstritt, D., Krugel, A., Weber, A. and Ivers-Tiffée, E. (2001) Thermocyclic load: Delamination defects and electrical performance of single cells, *7th International Symposium on Solid Oxide Fuel Cells*, Jun 03-08, Tsukuba, Japan, pp. 942-951.

- Higashinakagawa, K., Sameshima, S. and Hirata, Y. (2004) Preparation, microstructures and electrical properties of a Ni/Sm-doped ceria cermet as an anode material of a solid oxide fuel cell, *Journal of Ceramic Processing Research*, **5**, 1, pp. 84-88.
- Holtappels, P. and Bagger, C. (2002) Fabrication and performance of advanced multi-layer SOFC cathodes, *Journal of the European Ceramic Society*, **22**, 1, pp. 41-48.
- Holtappels, P., Sorof, C., Verbraeken, M. C., Rambert, S. and Vogt, U. (2006) Preparation of porosity-graded SOFC anode substrates, *Fuel Cells*, **6**, 2, pp. 113-116.
- Hsiao, Y. C., Selman, J. Robert (1997) The degradation of SOFC electrodes, *Solid State Ionics*, **98**, 1-2, pp. 33-38.
- Huang, Q.-A., Hui, R., Wang, B. and Zhang, J. (2007) A review of AC impedance modeling and validation in SOFC diagnosis, *Electrochimica Acta*, **52**, 28, pp. 8144-8164.
- Huang, Y., Gong, X. Y., Suo, Z. and Jiang, Z. Q. (1997) A model of evolving damage bands in materials, *International Journal of Solids and Structures*, **34**, 30, pp. 3941-3951.
- Hui, R., Wang, Z. W., Kesler, O., Rose, L., Jankovic, J., Yick, S., Maric, R. and Ghosh, D. (2007) Thermal plasma spraying for SOFCs: Applications, potential advantages, and challenges, *Journal of Power Sources*, **170**, 2, pp. 308-323.
- Ishihara, T., Shibayama, T., Nishiguchi, H. and Takita, Y. (2000) Nickel-Gd-doped CeO₂ cermet anode for intermediate temperature operating solid oxide fuel cells using LaGaO₃-based perovskite electrolyte, *Solid State Ionics*, **132**, 3-4, pp. 209-216.
- Jiang, S. P., Wang, W. and Zhen, Y. D. (2005) Performance and electrode behaviour of nano-YSZ impregnated nickel anodes used in solid oxide fuel cells, *Journal of Power Sources*, **147**, 1-2, pp. 1-7.
- Jiang, Z. Q., Huang, Y. and Chandra, A. (1997) Thermal stresses in layered electronic assemblies, *Journal of Electronic Packaging*, **119**, 2, pp. 127-132.
- Jokanović, V. (1996) Syndissertation and formation mechanism of ultrafine spherical Al₂O₃ powders by ultrasonic spray pyrolysis, *Materials transactions, JIM*, **37**, 4, p. 627.
- Jokanovic, V., Janackovic, D. and Uskokovic, D. (1999) Influence of aerosol formation mechanism by an ultrasonic field on particle size distribution of ceramic powders, *Ultrasonics Sonochemistry*, **6**, 3, pp. 157-169.
- Jokanović, V., Spasić, A. M. and Uskoković, D. (2004) Designing of nanostructured hollow TiO₂ spheres obtained by ultrasonic spray pyrolysis, *Journal of Colloid and Interface Science*, **278**, 2, pp. 342-352.

Jono, K., Suda, S. and Hattori, M. (2007a) Effect of Graded Porous Structure on Ni-YSZ Anode Performance, *ECS Transactions*, **7**, 1, pp. 1541-1546.

Jono, K., Suda, S. and Hattori, M. (2007b) Effect of graded porous structure on Ni-YSZ anode performance, 1 PART 2 Edn, Electrochemical Society Inc., Pennington, NJ 08534-2896, United States, pp. 1541-1546.

Kharton, V. V., Figueiredo, F. M., Navarro, L., Naumovich, E. N., Kovalevsky, A. V., Yaremchenko, A. A., Viskup, A. P., Carneiro, A., Marques, F. M. B. and Frade, J. R. (2001) Ceria-based materials for solid oxide fuel cells, *Journal of Materials Science*, **36**, 5, pp. 1105-1117.

Kim, J. W., Virkar, A. V., Fung, K. Z., Mehta, K. and Singhal, S. C. (1999) Polarization effects in intermediate temperature, anode-supported solid oxide fuel cells, *Journal of the Electrochemical Society*, **146**, 1, pp. 69-78.

Koch, S., Hendriksen, P. V., Mogensen, M., Liu, Y., Dekker, N., Rietveld, B., de Haart, B. and Tietz, F. (2006) Solid oxide fuel cell performance under severe operating conditions, *6th European Solid Oxide Fuel Cell Forum (SOFC)*, 2004, Luzerne, SWITZERLAND, pp. 130-136.

Koide, H., Someya, Y., Yoshida, T. and Maruyama, T. (2000) Properties of Ni/YSZ cermet as anode for SOFC, *Solid State Ionics*, **132**, 3-4, pp. 253-260.

Komatsu, T., Watanabe, K., Arakawa, M. and Arai, H. (2009) A long-term degradation study of power generation characteristics of anode-supported solid oxide fuel cells using LaNi(Fe)O₃ electrode, *Journal of Power Sources*, **193**, 2, pp. 585-588.

Kumar, A. N. and Sorensen, B. F. (2002) Fracture energy and crack growth in surface treated Ytria stabilized Zirconia for SOFC applications, *Materials Science and Engineering a-Structural Materials Properties Microstructure and Processing*, **333**, 1-2, pp. 380-389.

Kuo, C. H. and Gupta, P. K. (1995) Rigidity and conductivity percolation thresholds in particulate composites, *Acta Metallurgica Et Materialia*, **43**, 1, pp. 397-403.

Lanfrey, P. Y., Kuzeljevic, Z. V. and Dudukovic, M. P. (2010) Tortuosity model for fixed beds randomly packed with identical particles, *Chemical Engineering Science*, **65**, 5, pp. 1891-1896.

Laurencin, J., Delette, G., Lefebvre-Joud, F. and Dupeux, A. (2008) A numerical tool to estimate SOFC mechanical degradation: Case of the planar cell configuration, *Journal of the European Ceramic Society*, **28**, 9, pp. 1857-1869.

- Laurencin, J., Delette, G., Morel, B., Lefebvre-Joud, F. and Dupeux, M. (2009) Solid Oxide Fuel Cells damage mechanisms due to Ni-YSZ re-oxidation: Case of the Anode Supported Cell, *Journal of Power Sources*, **192**, 2, pp. 344-352.
- Leah, R. T., Brandon, N. P. and Aguiar, P. (2005) Modelling of cells, stacks and systems based around metal-supported planar IT-SOFC cells with CGO electrolytes operating at 500–600 °C, *Journal of Power Sources*, **145**, 2, pp. 336-352.
- Lee, C. B. and Bae, J. M. (2008) Fabrication and characterization of metal-supported solid oxide fuel cells, *Journal of Power Sources*, **176**, 1, pp. 62-69.
- Lee, J. H., Heo, J. W., Lee, D. S., Kim, J., Kim, G. H., Lee, H. W., Song, H. S. and Moon, J. H. (2003) The impact of anode microstructure on the power generating characteristics of SOFC, *Solid State Ionics*, **158**, 3-4, pp. 225-232.
- Leone, P., Santarelli, M., Asinari, P., Cal, M. and Borchiellini, R. (2008) Experimental investigations of the microscopic features and polarization limiting factors of planar SOFCs with LSM and LSCF cathodes, *Journal of Power Sources*, **177**, 1, pp. 111-122.
- Li, C.-X., Li, C.-J. and Guo, L.-J. (2010) Effect of composition of NiO/YSZ anode on the polarization characteristics of SOFC fabricated by atmospheric plasma spraying, *International Journal of Hydrogen Energy*, **35**, 7, pp. 2964-2969.
- Li, Q. and Thangadurai, V. (2009) Syndissertation, Structure and Electrical Properties of Mo-doped CeO₂-Materials for SOFCs, *Fuel Cells*, **9**, 5, pp. 684-698.
- Li, X. (2006) *Principles of Fuel Cells*, Taylor & Francis Group, New York.
- Litzelman, S. J., Hertz, J. L., Jung, W. and Tuller, H. L. (2008) Opportunities and Challenges in Materials Development for Thin Film Solid Oxide Fuel Cells, *Fuel Cells*, **8**, 5, pp. 294-302.
- Liu, L., Kim, G.-Y. and Chandra, A. (2010a) Fabrication of solid oxide fuel cell anode electrode by spray pyrolysis, *Journal of Power Sources*, **195**, 20, pp. 7046-7053.
- Liu, L., Kim, G.-Y. and Chandra, A. (2010b) Modeling of thermal stresses and lifetime prediction of planar solid oxide fuel cell under thermal cycling conditions, *Journal of Power Sources*, **195**, 8, pp. 2310-2318.
- Liu, L., Kim, G.-Y., Hillier, A. C. and Chandra, A. (2011) Microstructural and electrochemical impedance study of nickel–Ce_{0.9}Gd_{0.1}O_{1.95} anodes for solid oxide fuel cells fabricated by ultrasonic spray pyrolysis, *Journal of Power Sources*, **196**, 6, pp. 3026-3032.

Liu, Y. L. and Jiao, C. G. (2005) Microstructure degradation of an anode/electrolyte interface in SOFC studied by transmission electron microscopy, *Solid State Ionics*, **176**, 5-6, pp. 435-442.

Lowrie, F. L. and Rawlings, R. D. (2000) Room and high temperature failure mechanisms in solid oxide fuel cell electrolytes, *Journal of the European Ceramic Society*, **20**, 6, pp. 751-760.

Maffei, N. and de Silveira, G. (2003) Interfacial layers in tape cast anode-supported doped lanthanum gallate SOFC elements, *Solid State Ionics*, **159**, 3-4, pp. 209-216.

Meng, B., Sun, Y., He, X. D. and Li, M. W. (2008) Graded Ni-YSZ anode coatings for solid oxide fuel cell prepared by EB-PVD, *Materials Science and Technology*, **24**, 8, pp. 997-1001.

Miladin, R. and Edgar, L. C. (2004a) Elastic Properties of Nickel-Based Anodes for Solid Oxide Fuel Cells as a Function of the Fraction of Reduced NiO, *Journal of the American Ceramic Society*, **87**, 12, pp. 2242-2246.

Miladin, R. and Edgar, L. C. (2004b) Mechanical properties of tape cast nickel-based anode materials for solid oxide fuel cells before and after reduction in hydrogen, *Acta Materialia*, **52**, 20, pp. 5747-5756.

Minh, N. Q. (2004) Solid oxide fuel cell technology--features and applications, *Solid State Ionics*, **174**, 1-4, pp. 271-277.

Moe, K. K., Tagawa, T, Goto and S (1998) *Preparation of electrode catalyst for SOFC reactor by ultrasonic mist pyrolysis : Effect of spray time*, Nippon seramikusu kyokai, Tokyo, JAPON.

Mori, M., Yamamoto, T., Itoh, H., Inaba, H. and Tagawa, H. (1998) Thermal expansion of nickel-zirconia anodes in solid oxide fuel cells during fabrication and operation, *Journal of the Electrochemical Society*, **145**, 4, pp. 1374-1381.

Muecke, U. P., Akiba, K., Infortuna, A., Salkus, T., Stus, N. V. and Gauckler, L. J. (2008) Electrochemical performance of nanocrystalline nickel/gadolinia-doped ceria thin film anodes for solid oxide fuel cells, *Solid State Ionics*, **178**, 33-34, pp. 1762-1768.

Muecke, U. P., Messing, G. L. and Gauckler, L. J. (2009) The Leidenfrost effect during spray pyrolysis of nickel oxide-gadolinia doped ceria composite thin films, *Thin Solid Films*, **517**, 5, pp. 1515-1521.

N.H.J. Stelzer, C. H. C., L.N. van Rij, J. Schoonman (1997) Spray Deposition of Doped YSZ Electrode Materials for a Monolithic Solid Oxide Fuel Cell Design, *Materials and Processes 10th I.E.A. SOFC Workshop*, Switzerland, p. 236.

Nakajo, A., Stiller, C., Härkegård, G. and Bolland, O. (2006) Modeling of thermal stresses and probability of survival of tubular SOFC, *Journal of Power Sources*, **158**, 1, pp. 287-294.

Nam, J. H. and Jeon, D. H. (2006) A comprehensive micro-scale model for transport and reaction in intermediate temperature solid oxide fuel cells, *Electrochimica Acta*, **51**, 17, pp. 3446-3460.

Nguyen, T. and Djurado, E. (2001) Deposition and characterization of nanocrystalline tetragonal zirconia films using electrostatic spray deposition, *Solid State Ionics*, **138**, 3-4, pp. 191-197.

Ni, M., Leung, M. K. H. and Leung, D. Y. C. (2007a) Mathematical modelling of proton-conducting solid oxide fuel cells and comparison with oxygen-ion-conducting counterpart, *Fuel Cells*, **7**, 4, pp. 269-278.

Ni, M., Leung, M. K. H. and Leung, D. Y. C. (2007b) Micro-scale modeling of a functionally graded Ni-YSZ anode, *Chemical Engineering and Technology*, **30**, 5, pp. 587-592.

Ni, M., Leung, M. K. H. and Leung, D. Y. C. (2007c) Micro-scale modelling of solid oxide fuel cells with micro-structurally graded electrodes, *Journal of Power Sources*, **168**, 2, pp. 369-378.

Noren, D. A. and Hoffman, M. A. (2005) Clarifying the Butler-Volmer equation and related approximations for calculating activation losses in solid oxide fuel cell models, *Journal of Power Sources*, **152**, pp. 175-181.

O'Hayre, R., Barnett, D. M. and Prinz, F. B. (2005a) The triple phase boundary - A mathematical model and experimental investigations for fuel cells, *Journal of the Electrochemical Society*, **152**, 2, pp. A439-A444.

O'Hayre, R., Barnett, D. M. and Prinz, F. B. (2005b) The triple phase boundary a mathematical model and experimental investigations for fuel cells, *Journal of the Electrochemical Society*, **152**, 2, pp. 439-444.

Ohno, N. and Hutchinson, J. W. (1984) Plastic-flow Localization due to Non-uniform Void Distribution, *Journal of the Mechanics and Physics of Solids*, **32**, 1, pp. 63-85.

Ormerod, R. M. (2003) Solid oxide fuel cells, *Chemical Society Reviews*, **32**, 1, pp. 17-28.

Perednis, D. and Gauckler, L. J. (2005) Thin Film Deposition Using Spray Pyrolysis, *Journal of Electroceramics*, **14**, 2, pp. 103-111.

Pihlatie, M., Kaiser, A. and Mogensen, M. (2008) Mechanical properties of NiO/Ni-YSZ composites depending on temperature, porosity and redox cycling, *Journal of the European Ceramic Society*, **In Press, Corrected Proof**,

Pitakthapanaphong, S. and Busso, E. P. (2005) Finite element analysis of the fracture behaviour of multi-layered systems used in solid oxide fuel cell applications, *Modelling and Simulation in Materials Science and Engineering*, **13**, 4, pp. 531-540.

Prabhakaran, K., Beigh, M. O., Lakra, J., Gokhale, N. M. and Sharma, S. C. (2007) Characteristics of 8mol% yttria stabilized zirconia powder prepared by spray drying process, *Journal of Materials Processing Technology*, **189**, 1-3, pp. 178-181.

Primdahl, S. and Liu, Y. L. (2002) Ni Catalyst for Hydrogen Conversion in Gadolinia-Doped Ceria Anodes for Solid Oxide Fuel Cells, *Journal of The Electrochemical Society*, **149**, 11, pp. A1466-A1472.

Princivalle, A., Perednis, D., Neagu, R. and Djurado, E. (2004) Microstructural Investigations of Nanostructured La(Sr)MnO₃-未 Films Deposited by Electrostatic Spray Deposition, *Chemistry of Materials*, **16**, 19, pp. 3733-3739.

Reid, R. P., John; Poling, Bruce (1987) *The Properties of Gases & Liquids*, 4th Edn, McGraw-Hill Book Company, New York.

Rotureau, D., Viricelle, J. P., Pijolat, C., Caillol, N. and Pijolat, M. (2005) Development of a planar SOFC device using screen-printing technology, *Journal of the European Ceramic Society*, **25**, 12, pp. 2633-2636.

Sameshima, S., Ichikawa, T., Kawaminami, M. and Hirata, Y. (1999) Thermal and mechanical properties of rare earth-doped ceria ceramics, *Materials Chemistry and Physics*, **61**, 1, pp. 31-35.

Sarantaridis, D., Rudkin, R. A. and Atkinson, A. (2008) Oxidation failure modes of anode-supported solid oxide fuel cells, *Journal of Power Sources*, **180**, 2, pp. 704-710.

Schneider, L. C. R., Martin, C. L., Bultel, Y., Dessemond, L. and Bouvard, D. (2007) Percolation effects in functionally graded SOFC electrodes, *Electrochimica Acta*, **52**, 9, pp. 3190-3198.

Selcuk, A., Merere, G. and Atkinson, A. (2001) The influence of electrodes on the strength of planar zirconia solid oxide fuel cells, *Journal of Materials Science*, **36**, 5, pp. 1173-1182.

Shaffer, S. (2006) *Development Update on Delphi's Solid Oxide Fuel Cell Power System*, Philadelphia, PA.

Shi, M., Liu, N., Xu, Y. D., Wang, C., Yuan, Y. P., Majewski, P. and Aldinger, F. (2005) Preparation of electrolyte foils $\text{La}_{0.85}\text{Sr}_{0.15}\text{Ga}_{0.85}\text{Mg}_{0.15}\text{O}_{2.85}$ (LSGM) by means of tape casting, *Journal of Materials Processing Technology*, **169**, 2, pp. 179-183.

Simwonis, D., Thülen, H., Dias, F. J., Naoumidis, A. and Stöver, D. (1999) Properties of Ni/YSZ porous cermets for SOFC anode substrates prepared by tape casting and coat-mix[®] process, *Journal of Materials Processing Technology*, **92-93**, pp. 107-111.

Song, J. H., Park, S. I., Lee, J. H. and Kim, H. S. (2008) Fabrication characteristics of an anode-supported thin-film electrolyte fabricated by the tape casting method for IT-SOFC, *Journal of Materials Processing Technology*, **198**, 1-3, pp. 414-418.

Sorensen, B. F. and Primdahl, S. (1998) Relationship between strength and failure mode of ceramic multilayers, *Journal of Materials Science*, **33**, 22, pp. 5291-5300.

Steele, B. C. H. (2000) Appraisal of $\text{Ce}_{1-y}\text{Gd}_y\text{O}_{2-y/2}$ electrolytes for IT-SOFC operation at 500 degrees C, *Solid State Ionics*, **129**, 1-4, pp. 95-110.

Stoermer, A. O., Rupp, J. L. M. and Gauckler, L. J. (2006) Spray pyrolysis of electrolyte interlayers for vacuum plasma-sprayed SOFC, *Solid State Ionics*, **177**, 19-25, pp. 2075-2079.

Suda, S., Itagaki, M., Node, E., Takahashi, S., Kawano, M., Yoshida, H. and Inagaki, T. (2006) Preparation of SOFC anode composites by spray pyrolysis, *Journal of the European Ceramic Society*, **26**, 4-5, pp. 593-597.

Sun, X., Liu, W. N., Stephens, E. and Khaleel, M. A. (2008) Determination of interfacial adhesion strength between oxide scale and substrate for metallic SOFC interconnects, *Journal of Power Sources*, **176**, 1, pp. 167-174.

Surdoval, W. A. (2006) *7th SECA Public Workshop & Peer Review*, Philadelphia.

Suzuki, M. and Oshima, T. (1983) Estimation of the Co-ordination number in a Multi-Component Mixture of Spheres, *Powder Technology*, **35**, 2, pp. 159-166.

Taniguchi, S., Kadowaki, M., Yasuo, T., Akiyama, Y., Miyake, Y. and Nishio, K. (2000) Improvement of thermal cycle characteristics of a planar-type solid oxide fuel cell by using ceramic fiber as sealing material, *Journal of Power Sources*, **90**, 2, pp. 163-169.

Tanner, C. W., Fung, K. Z. and Virkar, A. V. (1997) The effect of porous composite electrode structure on solid oxide fuel cell performance .1. Theoretical analysis, *Journal of the Electrochemical Society*, **144**, 1, pp. 21-30.

- Tietz, F. (1999) Thermal expansion of SOFC materials, *Ionics*, **5**, 1, pp. 129-139.
- Tsoga, A., Gupta, A., Naoumidis, A. and Nikolopoulos, P. (2000) Gadolinia-doped ceria and yttria stabilized zirconia interfaces: regarding their application for SOFC technology, *Acta Materialia*, **48**, 18-19, pp. 4709-4714.
- Uchida, H., Arisaka, S. and Watanabe, M. (2000) High performance electrodes for medium-temperature solid oxide fuel cells: Activation of La(Sr)CoO₃ cathode with highly dispersed Pt metal electrocatalysts, *Solid State Ionics*, **135**, 1-4, pp. 347-351.
- Van herle, J., Ihringer, R., Vasquez Cavieres, R., Constantin, L. and Bucheli, O. (2001) Anode supported solid oxide fuel cells with screen-printed cathodes, *Journal of the European Ceramic Society*, **21**, 10-11, pp. 1855-1859.
- Virkar, A. V., Chen, J., Tanner, C. W. and Kim, J. W. (2000) The role of electrode microstructure on activation and concentration polarizations in solid oxide fuel cells, *Solid State Ionics*, **131**, 1-2, pp. 189-198.
- Waldbillig, D., Wood, A. and Ivey, D. G. (2005) Electrochemical and microstructural characterization of the redox tolerance of solid oxide fuel cell anodes, *Journal of Power Sources*, **145**, 2, pp. 206-215.
- Wang, J. C. (1984) Young's modulus of porous materials. part 1. Theoretical derivation of modulus-porosity correlation, *Journal of Materials Science*, **19**, 3, pp. 801-808.
- Wang, J. L. and Zeng, S. X. (2008) Thermal stresses analysis in adhesive/solder bonded bimaterial assemblies, *Journal of Applied Physics*, **104**, 11, pp. 113501-113508.
- Wang, K. P., Huang, Y. Y., Chandra, A. and Hu, K. X. (2000) Interfacial shear stress, peeling stress, and die cracking stress in trilayer electronic assemblies, *IEEE Transactions on Components and Packaging Technologies*, **23**, 2, pp. 309-316.
- Wilhelm, O., Pratsinis, S. E., Perednis, D. and Gauckler, L. J. (2005) Electrospray and pressurized spray deposition of yttria-stabilized zirconia films, *Thin Solid Films*, **479**, 1-2, pp. 121-129.
- Will, J., Mitterdorfer, A., Kleinlogel, C., Perednis, D. and Gauckler, L. J. (2000) Fabrication of thin electrolytes for second-generation solid oxide fuel cells, *Solid State Ionics*, **131**, 1-2, pp. 79-96.
- Williams, M. C. (2007) Solid oxide fuel cells: Fundamentals to systems, *Fuel Cells*, **7**, 1, pp. 78-85.

- Xie, Y., Neagu, R., Hsu, C.-S., Zhang, X. and Deces-Petit, C. (2007) Spray Pyrolysis Deposition of Electrolyte and Anode for Metal Supported Solid Oxide Fuel Cell, *ECS Transactions*, **7**, 1, pp. 787-794.
- Xu, X., Xia, C., Huang, S. and Peng, D. (2005a) YSZ thin films deposited by spin-coating for IT-SOFCs, *Ceramics International*, **31**, 8, pp. 1061-1064.
- Xu, X., Xia, C., Xiao, G. and Peng, D. (2005b) Fabrication and performance of functionally graded cathodes for IT-SOFCs based on doped ceria electrolytes, *Solid State Ionics*, **176**, 17-18, pp. 1513-1520.
- Yakabe, H., Baba, Y., Sakurai, T. and Yoshitaka, Y. (2004) Evaluation of the residual stress for anode-supported SOFCs, *Journal of Power Sources*, **135**, 1-2, pp. 9-16.
- Yang, C., Li, W., Zhang, S., Bi, L., Peng, R., Chen, C. and Liu, W. (2009) Fabrication and characterization of an anode-supported hollow fiber SOFC, *Journal of Power Sources*, **187**, 1, pp. 90-92.
- Yokokawa, H., Tu, H., Iwanschitz, B. and Mai, A. (2008) Fundamental mechanisms limiting solid oxide fuel cell durability, *Journal of Power Sources*, **182**, 2, pp. 400-412.
- Yoon, K. J., Zink, P., Gopalan, S. and Pal, U. B. (2007) Polarization measurements on single-step co-fired solid oxide fuel cells (SOFCs), *Journal of Power Sources*, **172**, 1, pp. 39-49.
- Yoon, S. P., Nam, S. W., Han, J., Lim, T. H., Hong, S. A. and Hyun, S. H. (2004) Effect of electrode microstructure on gas-phase diffusion in solid oxide fuel cells, *Solid State Ionics*, **166**, 1-2, pp. 1-11.
- Yu, J. H., Park, G. W., Lee, S. and Woo, S. K. (2007) Microstructural effects on the electrical and mechanical properties of Ni-YSZ cermet for SOFC anode, *Journal of Power Sources*, **163**, 2, pp. 926-932.
- Zhang, T., Zhu, Q., Huang, W. L., Xie, Z. and Xin, X. (2008) Stress field and failure probability analysis for the single cell of planar solid oxide fuel cells, *Journal of Power Sources*, **182**, 2, pp. 540-545.
- Zhang, X., Ohara, S., Maric, R., Okawa, H., Fukui, T., Yoshida, H., Inagaki, T. and Miura, K. (2000) Interface reactions in the NiO-SDC-LSGM system, *Solid State Ionics*, **133**, 3-4, pp. 153-160.
- Zhao, F. and Virkar, A. V. (2005) Dependence of polarization in anode-supported solid oxide fuel cells on various cell parameters, *Journal of Power Sources*, **141**, 1, pp. 79-95.

Zhao, H., Li, X., Ju, F. and Pal, U. (2008) Effects of particle size of 8mol% Y_2O_3 stabilized ZrO_2 (YSZ) and additive Ta_2O_5 on the phase composition and the microstructure of sintered YSZ electrolyte, *Journal of Materials Processing Technology*, **200**, 1-3, pp. 199-204.

Zhao, Y., Shah, N. and Brandon, N. (2010) The Development and Application of a Novel Optimisation Strategy for Solid Oxide Fuel Cell-Gas Turbine Hybrid Cycles, *Fuel Cells*, **10**, 1, pp. 181-193.

Zhonghe, B., Baolian, Y., Zhenwei, W., Yonglai, D., Hejin, W., Yunchuan, S. and Mojie, C. (2004) A High-Performance Anode-Supported SOFC with LDC-LSGM Bilayer Electrolytes, *Electrochemical and Solid-State Letters*, **7**, 5, pp. A105-A107.

Zhu, H. and Kee, R. J. (2003) A general mathematical model for analyzing the performance of fuel-cell membrane-electrode assemblies, *Journal of Power Sources*, **117**, 1-2, pp. 61-74.